School of Physical and Chemical Sciences
University of Canterbury, Private Bag 4800
Christchurch, New Zealand

# Photometry and Spectroscopy of RV Tauri stars

*A thesis presented for the degree of*

Master of Science in Astronomy

*by*

**Kunal Bhardwaj**

*Supervisor:* Assoc. Prof. Karen R. Pollard


**July 2020**

*I feel the ocean swaying me*
*Washing away all my pain*
*See where I used to be wounded*
*Remember the scar?*
*Now you can't see a thing*
*And I don't feel no pain, no, no*

*Singing about the Valleys of Sunrise*
*Green and blue canyons, too*
*Singing about Atlantis love songs*
*The Valleys of Neptune is rising, rising, rising*

*- Jimi Hendrix*

## Abstract

RV Tauri stars are recognized as radially pulsating, post-Asymptotic Giant Branch stars, in the high-luminosity end of type-II Cepheids. They show characteristic light modulations and spectral line variations which are generally linked with intrinsic radial pulsations and resulting shock waves. This thesis investigates stellar pulsations in a sample of RV Tauri stars using a mix of analytical methods. In particular, it examines the short-term and long-term variability by searching for periodicities in the photometric and spectroscopic data for a number of selected southern hemisphere RV Tauri stars. These data are used to explore how the variability and other observed stellar properties, fit within the current theories which explain RV Tauri behaviour as being due to stellar pulsation, binarity, and interaction with its local environment, including circumbinary dust.

We use extensive visual photometric data from the AAVSO International Database for analysing the long-term and short-term variations and recent $BV$ data for analysing the short-term pulsations. AAVSO's `VPhot` was used to perform differential photometry for the $BV$ data and `Period04` was used for Fourier analysis and least-squares fitting in a pre-whitening manner to find periodicites in both visual and $BV$ data.

Both short-term pulsational and most of the long-term periods of all the stars studied were found to be in reasonable agreement with the published values. The amplitude of the long-term periods was substantial in variation. Complex peak structures are seen in periodograms possibly owing to period changes over time and/or "flips" seen in the deep-shallow light curve alternation with time. These variations in both short and long-term periods (and also amplitude) over time is confirmed in wavelet analysis of U Mon and IW Car.

Nearly 100 spectra of U Mon were acquired over 5 months to cover $\sim$1.5 cycles of its 92-day pulsation period. Effects of two pulsation-related shock-waves per pulsation cycle were seen on specific spectral line profiles, consistent with previous studies. The new pulsational radial velocity curves measured by Gaussian profile fitting to the Fe I line at 6200.313 Å show well-defined consistency with the published pulsational radial velocity curve. The results in this thesis add depth and scope to the leading RV Tauri model which explains the light and spectral variations in RVb stars through a combination of binarity, intrinsic stellar pulsations, interaction and obscuration mechanisms involving binaries and circumstellar/circumbinary disk depending on the observer's perspective.

# Acknowledgements

Thank you Family, for making it possible.
Thank you Karen, for being so kind.
Thank you Bum, for all the good and the bad.
Thank you Friends for being as cool as you can.
Thanks to myself for making it through.
And the Reader, thanks to you.

# Contents

# List of Figures

# List of Tables

# Chapter 1

# Introduction

## 1.1 Stellar pulsations

Stellar pulsations are a result of periodic physical changes in stars. Intrinsic changes in brightness, size, colour and temperature in pulsating stars causes observable variations in their light, colour and radial velocity curves. The class of star analysed in this thesis, the RV Tauri stars, are evolved, luminous population II giants and supergiants that display radial pulsations (Preston et al. 1963; Aerts et al. 2010).

### 1.1.1 Modelling oscillations in stars

Pulsating stars can be modelled as spheres oscillating at specific frequencies due to internal standing sound waves which are self-excited within the star. The sound waves causes star to expand and contract (get cooler and hotter). We detect these pulsations in both photometry and spectroscopy as the star's surface oscillates, and the star becoming brighter and dimmer and hotter and cooler as it pulsates. To understand 3-D radial oscillations in stars, we can build up the concept by understanding 1-D and 2-D oscillations of a string and a drum head respectively (Kurtz, 2006).

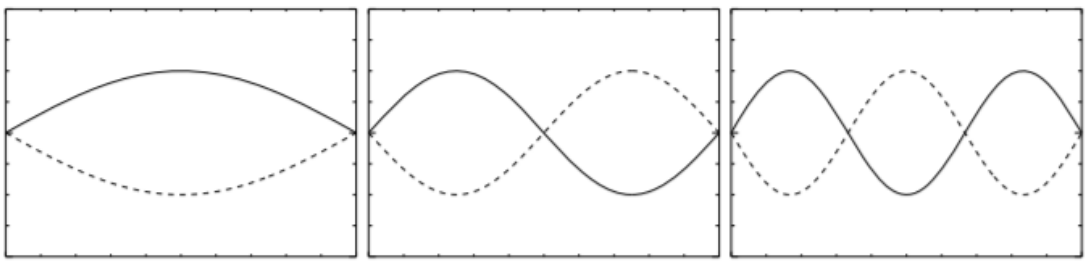

**Figure 1.1:** First three oscillation modes for a standing wave on a string fixed at both ends.

Figure 1.1 shows different oscillation patterns of a string such as in a guitar. Each pattern is a specific mode of oscillation. The length of the string determines the frequency of oscillations. The fundamental mode has no nodes except for the fixed ends, while the first overtone has a node in the middle of the string and vibrates with twice the frequency of the fundamental mode. The second overtone has two nodes equally spaced and vibrates with three times the frequency of the fundamental mode and so on. These overtones are called harmonics, where the first overtone and fundamental mode has a ratio of 2:1, the second overtone and first overtone has a ratio of 3:2 and so on. A similar view can be acquired by air oscillations in an open-closed organ pipe with an antinode at the open end. Such an organ pipe is a simple comparison to a radially pulsating star, except that stars do not have a constant temperature, density, pressure and chemistry from its interior to its surface as an organ pipe does.

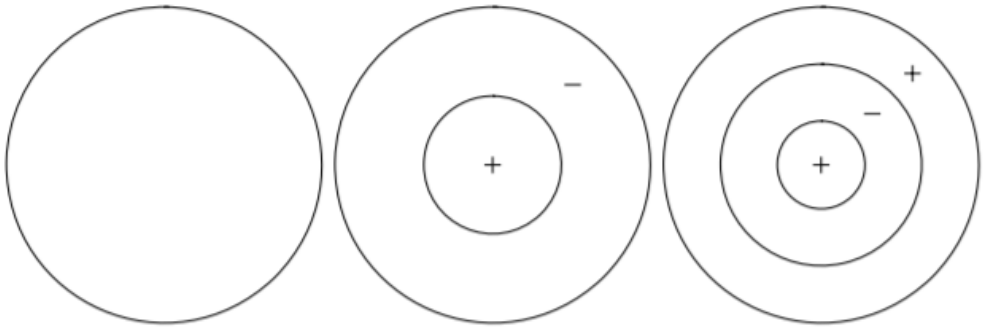


**Figure 1.2:** First three radial oscillation modes for a drum head. The outward and inward antiphase movement of the drum head is shown by plus and minus signs respectively.

For a 2-D representation of radial pulsations in a star, we can use vibrations of a drum head as a simple analogy. Figure 1.2 shows the first three radial oscillations on a circular drum head. The fixed nodal line is a circle at the rim of the drum head. On the left, the fundamental mode is when the drum head moves up and down with an antinode at the centre of the circular head. The middle shows the first radial overtone where the inner and outer circular region move up and down in antiphase, with a circular node. The right one shows the second radial overtone with two nodes at the two concentric circles, and so on.

### 1.1.2 Formalism of 3-D oscillations in stars

For a 3-D description of stellar oscillations, stars can be treated as spherically-symmetric, self-gravitating fluid. Hence we can use spherical harmonics as we need to view nodes as concentric shells rather than circles (as in the case of drum head).

To do this, a few assumptions are needed to be made; conservation of thermal energy being one. The flux is then defined by the energy transported through various stellar layers via radiation and convection. The convection-related parameters are considered the most complicated aspect of pulsation theory and in practice are generally simplified or neglected (de Boer & Seggewiss, 2008).

The reviews by Brown & Gilliland (1994) and Gautschy & Saio (1995) note that a simplified description of oscillations is possible by treating them as small perturbations about the equilibrium state of a star. The pulsation eigenmodes can be written as a product of a function of radius $\xi(r)$ and a spatial spherical harmonic $Y_l^m$. The spatial and temporal perturbations to a star's mean state are then as given in (Brown & Gilliland, 1994) as

$$\xi_{nlm}(r, \theta, \phi, t) = \xi_{nl}(r) Y_l^m(\theta, \phi) e^{-i\omega_{nlm}t} \tag{1.1}$$

where $\xi$ is any scalar perturbation associated with the mode (*e.g.* radial displacement), and r, $\theta$, $\phi$, and t are radial coordinate, the co-latitude[1], the longitude, and the time, respectively. The variable $\omega$ is the angular frequency of the oscillation. The spherical harmonics $Y_l^m(\theta, \phi)$ are given by

$$Y_l^m(\theta, \phi) = (-1)^m c_{lm} P_l^m(cos\theta) e^{im\theta} \tag{1.2}$$

where $P_l^m$ is a Legendre function, and the $c_{lm}$ is the normalisation constant given by

$$c_{lm}^2 = \frac{(2l+1)(l-m)!}{4\pi(l+m)!} \tag{1.3}$$

The parameters used for the description of the behaviour of the star are $n$, $l$ and $m$, where $n$ is the radial order (the number of nodes present between the centre and surface of a star), $l$ is the spherical degree of the mode (the number of nodal circles, where $l = 0$ signifies spherically symmetric radial oscillations), and $m$ is the azimuthal order that projects $l$ onto the star's equator and shows the number of nodal lines passing through the rotation axis. Thus $m = 2l+1$, where $l$ can be any integer from -$l$ to +$l$. Some radial and non-radial pulsation patterns are shown in Figure 1.3.

### 1.1.3 Spherically symmetric radial pulsations

The simplest way a star can pulsate is radially (where $l$=0 in equations $1.1 - 1.3$). In this case, the stellar photosphere expands and contracts preserving its spherical symmetry, unlike non-radial modes where different parts of the star move inward or outward. The oscillations of air in an organ pipe, as mentioned in Section 1.1.1, are analogous in 3D to the radial oscillations in a star, as shown in Figure 1.4.

[1]Latitude is measured from the equator, whereas co-latitude is measured from the pulsation axis which is assumed to coincide with the rotation axis for most pulsating stars

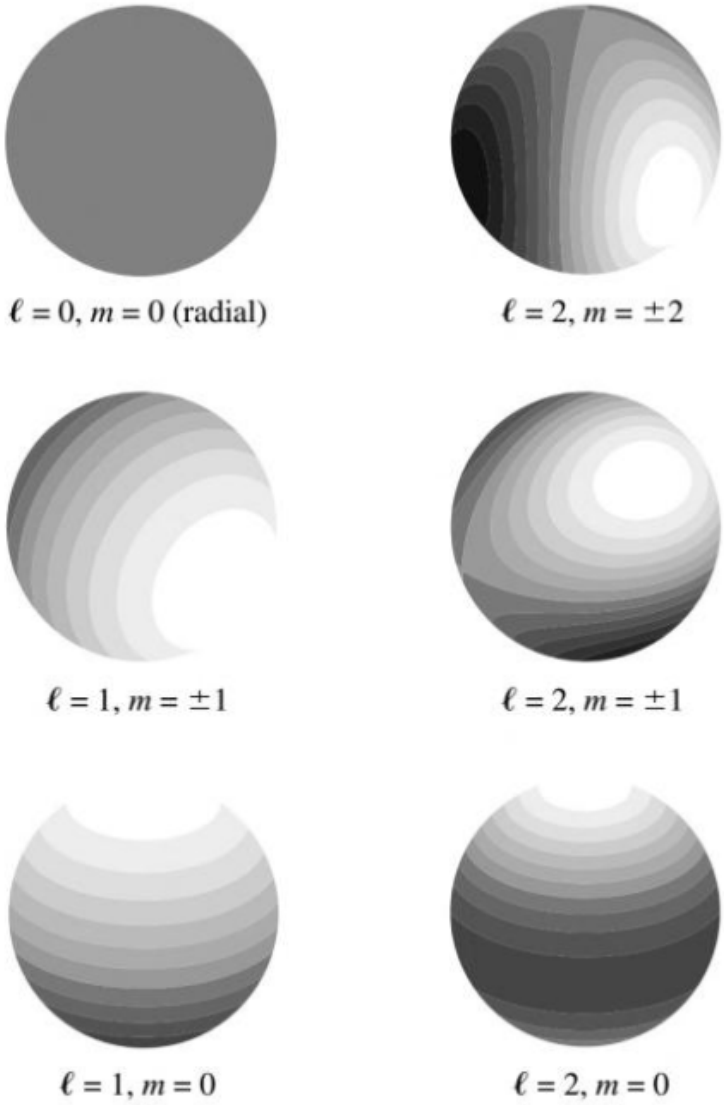


**Figure 1.3:** Radial and non-radial pulsation patterns where modes of pulsation are given by the real component of $Y_l^m$. Figure from Carroll & Ostlie (2017).

For the fundamental mode (Figure 1.4(a)), the node is at the center of the star and an antinode at the star's surface. Matter moves in the same direction at every point in the star. The first overtone is when a radial node (which is a concentric shell inside the star) is in between the star's center and surface, and the material is moving in antiphase on either side of this node (Figure 1.4(b)). The second overtone (Fig. 1.4(c)) has two radial nodes with matter moving in antiphase on either side of each node at the same time.

The majority of the types of stars in the instability strip, including RV Tauri stars, are known to pulsate in fundamental and first overtone radial modes (Catelan & Smith, 2015). The ratios of first overtone period to the fundamental period in these stars would be similar to that in an open-ended organ pipe were the stars

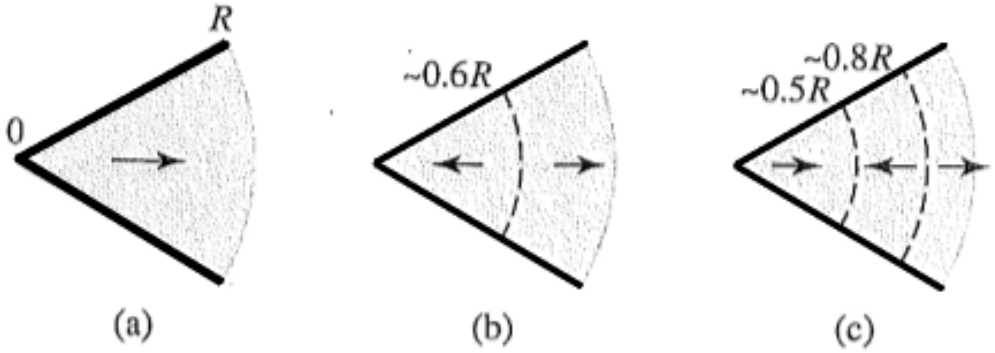


**Figure 1.4:** Radial standing sound waves for different modes in a spherically symmetric star. The fundamental mode is shown in (a), the first overtone in (b) and the second overtone in (c). The surface of the star is at radius $R$, the dashed lines represent the nodal surfaces, and the arrows indicate the direction of movement of the material in that region.

uniform in chemical composition and temperature. However, in real stars, the ratios of these periods depend on the sound speed gradient in the stars, which depends on temperature and chemical composition gradients (Aerts et al., 2010). Hence, the ratios of first overtone period to the fundamental period differs, for example, for late-stage centrally-condensed giant stars compared to hydrogen core-burning stars.

### 1.1.4 Driving mechanisms of pulsations

Opacity changes in stellar interiors are known to be a major driver of the pulsations in stars (de Boer & Seggewiss, 2008). This is known as the $\kappa$-mechanism. Kramer's opacity law states that the opacity, $\kappa$, of a layer of a star depends on the density $\rho$ and the temperature $T$ of the stellar material as

$$\kappa \propto \frac{\rho}{T^{3.5}}. \tag{1.4}$$

Both density and temperature rise due to compression of a stellar layer. As the equation above indicates, the opacity of the material is more sensitive to temperature than density, so opacity generally decreases upon compression. However, in pulsating stars like Population II Cepheids (see Section 1.3) with hydrogen and helium partial ionization zones, some heat generated from compression is used to ionize those zones further, hence the temperature is not substantially raised. Still, density does increase which leads to a corresponding increase in opacity of the layer. This results in containment of the radiation beneath the layer, in turn building the radiation pressure until the star begins to expand. Ions and electrons recombine in the hydrogen and helium partial ionization zones, and release energy, hence the

temperature does not decrease substantially during expansion. Meanwhile, opacity is again determined by density, which decreases during expansion. Radiation passes through the layer and, as the layer cools, the star contracts again. Hence, the cycle is repeated and the star pulsates.

The other pulsation driving mechanisms that may be actively affecting the overall oscillations along with the $\kappa$-mechanism are the perturbations in nuclear-burning energy output (the $\epsilon$-mechanism), and a mechanism driven by convection (Freytag et al., 2017).

## 1.2 The AGB to planetary nebula phase

A brief evolutionary description of a typical low-to-intermediate mass star (initial mass around $0.5 - 8\ M_{\odot}$) is given here, followed by more detailed descriptions of Population II Cepheids, RV Tauri stars and the specific target stars analysed in this thesis. For more detail, the reader is referred to the books by Kippenhahn et al. (2012) and Aerts et al. (2010) and the references therein.

As central helium depletes after core-helium burning, Population II stars with masses above $0.5\ M_{\odot}$ move from the horizontal branch to the early-Asymptotic Giant Branch (AGB) in the Hertzsprung-Russell diagram. In the early AGB phase, the star comprises of a degenerate carbon-oxygen core surrounded by hydrogen and helium fusing shells. The luminosity is primarily due to the faster-burning hydrogen-burning shell and, as a product of this, helium gets accumulated as a thin intershell between the carbon-oxygen core and the hydrogen shell. This thin helium intershell ignites as it becomes sufficiently massive and hydrogen shell-burning extinguishes as the outer layers expand. The star contracts and a huge amount of energy is released, produced largely by the triple-alpha process. The star begins to expand again due to the resulting helium convective zone (Eid, 2016). The convection is believed to mix the material produced in the core and the helium-hydrogen shells (Herwig, 2005). As a result of this extinction and re-ignition of the helium shell, the star starts to produce helium flashes, in turn causing major changes in its photospheric chemistry. This is known as the thermally-pulsing AGB phase (Herwig, 2005) and causes the star to cross the classical instability strip.

The helium intershell eventually loses mass, extinguishes and contracts. The hydrogen shell reignites, convection from which drives fresh material from nucleosynthesis upwards to the stellar surface. At the end of AGB phase, a complex mechanism involving the expansion of the outer layers, pulsations and radiation pressure on dust particles causes rapid mass-loss of the star (Höfner & Olofsson, 2018). This mass-loss ends eventually when the hydrogen shell burning ends, and the star begins its post-AGB phase.

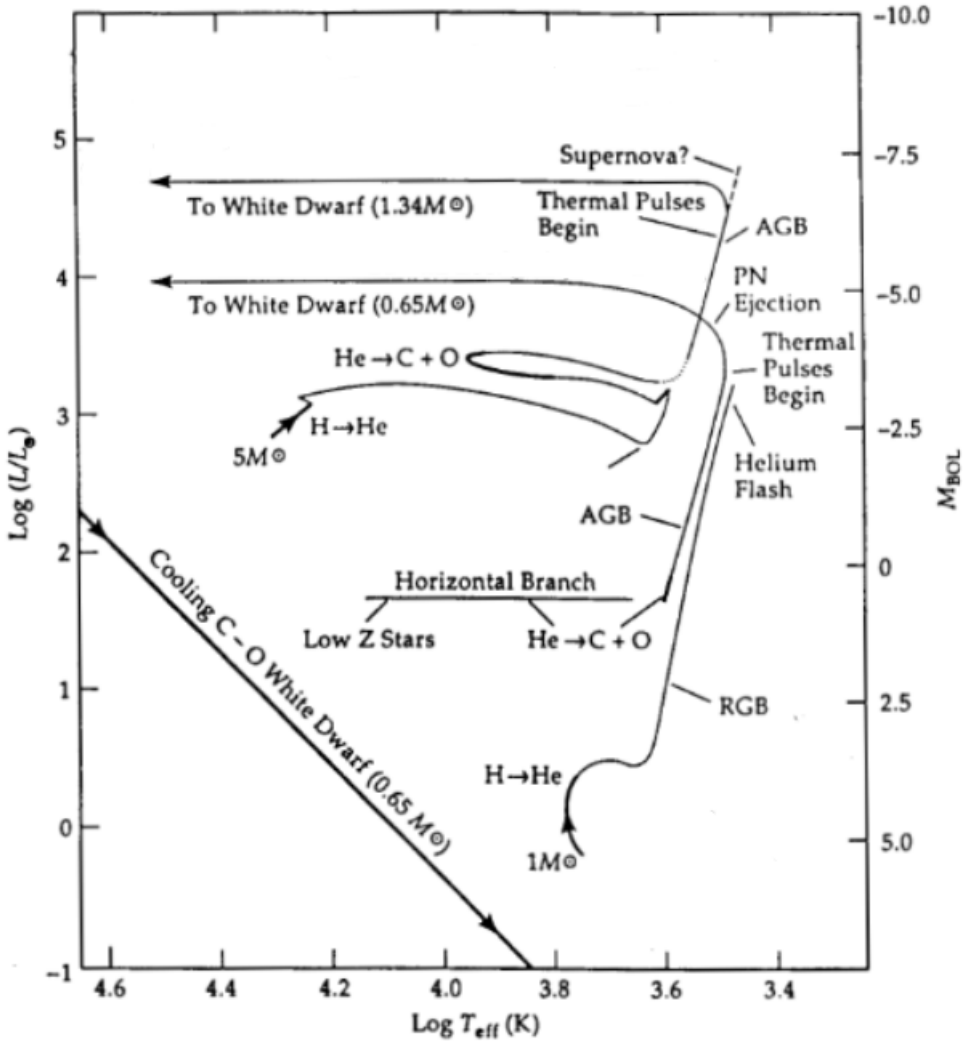


**Figure 1.5:** Hertzsprung-Russell diagram showing the evolution of a 1 $M_\odot$ star and a 5 $M_\odot$ star. Figure from Gary (2001).

Believed to be more or less spherically symmetric at this stage, post-AGB stars lose most of their material as the outer layers expand. A disk or a torus is likely to form if a companion star is present. Recent infrared studies of post-AGB stars such as by Sloan et al. (2014) and Matsuura et al. (2014) using the Spitzer Space Telescope show chemistry variations which could be linked to density variations in the circumstellar envelope, indicating the possibility of a disk or torus (Lagadec, 2017). Ultimately, the ejected material cools as it drifts further away as the star evolves and loses its outer atmosphere completely, exposing the extremely hot degenerate core. At this stage, high energy radiation from the core can ionize the previously-ejected material, which then is seen as emission nebula known as a planetary nebula. Planetary nebula can take a variety of shapes depending on the post-AGB stellar evolution, binarity and magnetic fields.

## 1.3 Population II Cepheids

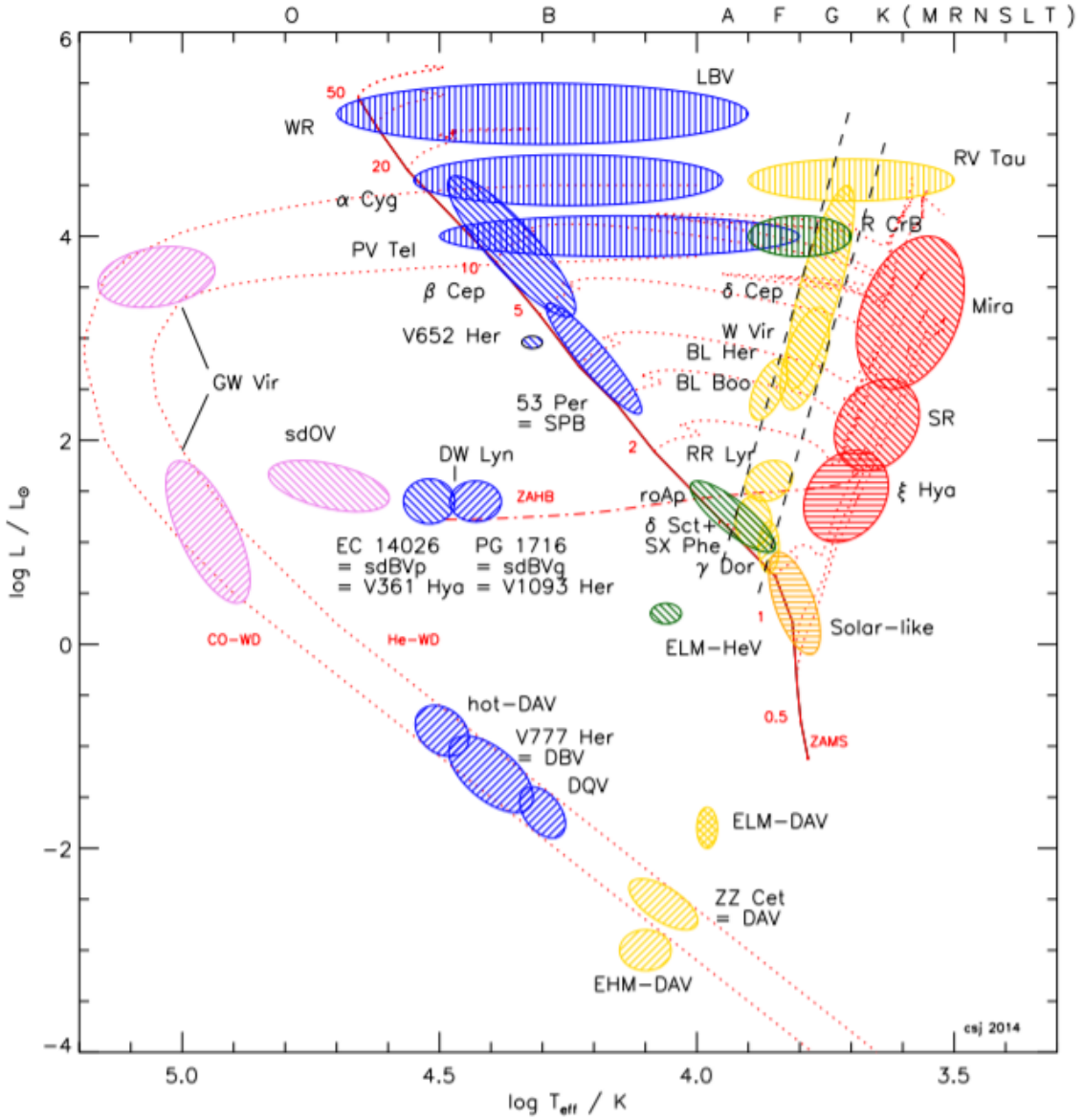


**Figure 1.6:** A Hertzsprung-Russell Diagram (Jeffery & Saio, 2016) showing the approximate locations of major classes of pulsating variables, coloured roughly by spectral type. Also indicated is the zero-age main sequence (red line) and horizontal branch, the Cepheid instability strip (black dashed lines), and evolutionary tracks for stars of various masses (red dotted lines), where mass in solar masses is indicated by small numbers in red. Shadings represent opacity driven p-modes (\\\\), g-modes (////) and strange modes (||||) and acoustically-driven modes (≡). Approximate spectral types are indicated on the top axis.

Among the stars found in the instability strip (see Figure 1.6) are Cepheids of Population I and II, also called Type I and II Cepheids. Population I Cepheids (or

Classical Cepheids) are relatively more massive ($\sim 4 - 20 M_{\odot}$) and younger stars ($10^7 - 10^8$ years) and mostly found in regions of recent star formation (Catelan & Smith, 2015). They are primarily used as standard candles for extragalactic distance determinations due to their well established period-luminosity relation. Population I Cepheids have been found to pulsate with up to three radial modes, with a combination of the fundamental, first and second overtone radial modes (see Soszynski et al. 2008a for a review).

Population II Cepheids are older and are evolved, low-mass ($\sim 0.5 - 0.8 M_{\odot}$) equivalent of Population I Cepheids. Their luminosities lie below those of Classical Cepheids and above those of RR Lyrae stars (Wallerstein, 2002), as shown in Figure 1.6. They have been detected in the Milky Way halo, bulge, spiral arms and globular clusters as well in other galaxies such as the LMC and SMC, Fornax dwarf galaxy, Andromeda and M32 (Catelan & Smith, 2015). The oscillations of these stars are caused by the $\kappa-$mechanism and these stars are believed to pulsate in either the radial fundamental or first overtone modes (Aerts et al., 2010). Their pulsations tend to be more unstable and complex in contrast to the stable and regular pulsations seen in Population I Cepheids. The mass of a Population II Cepheid is more concentrated in the core which is surrounded by a large envelope of nearly zero density gradient. The pulsations in such an envelope are non-linear and non-adiabatic, with many different pulsation modes over a wide range of effective temperature and luminosity (Pollard et al., 2000).

Population II Cepheids are roughly classified into three groups with differing evolutionary history, light curve characteristics and periods (see Wallerstein (2002) and Soszyński et al. (2008b)). These are the: BL Herculis type (BL Her, periods between $1 - 5$ days), W Virginis type (W Vir, periods $10 - 20$ days) and RV Tauri type (RV Tau, periods greater than 20 days), although these period boundaries are roughly estimated and usually overlap with each other (Soszyński et al., 2008b).

### 1.3.1 RV Tauri stars

RV Tauri type star are named after the prototype RV Tauri, the light variation of which was discovered by Ceraski in 1905 (Ceraski, 1905). The discovery popularized the star and led to all similarly pulsating stars to be named as RV Tauri type variables. A large infrared excess due to circumstellar dust is exhibited by a significant faction of RV Tauri stars, and on the basis of their infrared excess, luminosities and mass-loss history, they have been classified as post-AGB stars (Jura, 1986). They are radially-pulsating supergiants, having spectral types F to K, believed to be in transition from the AGB phase to the white dwarf phase, and in some cases, may be in a pre-planetary nebula phase (Willson & Templeton, 2009). It is also possible that their blueward evolution is slow enough so they do not photoionize their

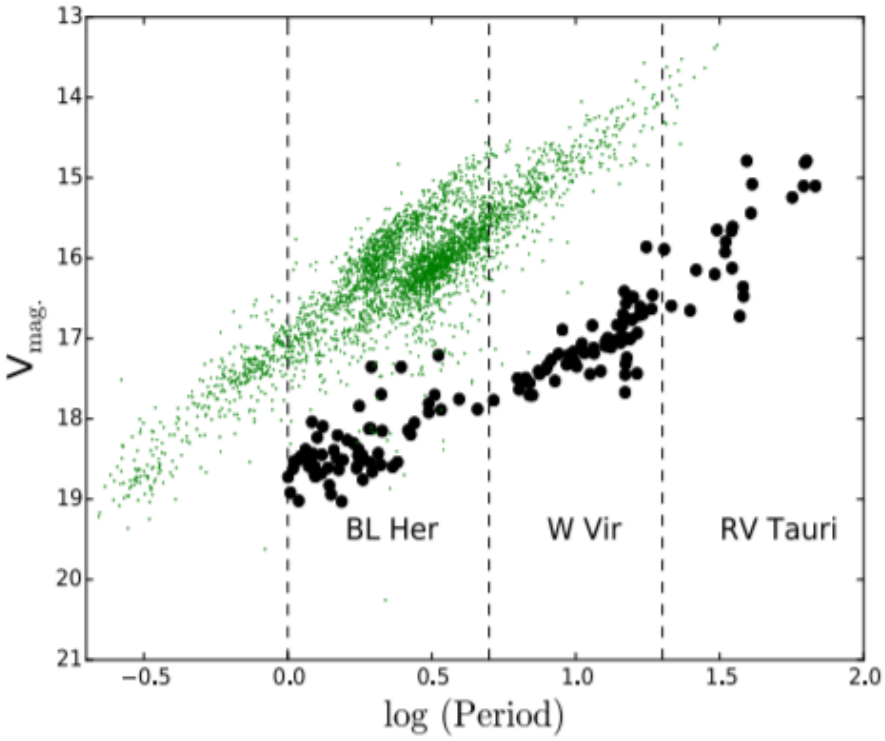


**Figure 1.7:** Period-luminosity relation of Population I Cepheids (green dots) and Population II Cepheids (black dots) in the LMC. Regions occupied by each type of population II Cepheid based on their pulsation periods are separated by dashed lines. Figure by Manick (2018) based on data from the OGLE-III LMC survey by Soszyński et al. (2008b).

envelope before it dissipates, and so never appear as planetary nebulae (Jura, 1986).

RV Tauri stars are known to be low-mass metal-deficient Population II Cepheids with semi-periods greater than 20 days (Wallerstein, 2002). They lie above the rest of the cooler Cepheids and extend on either side of the classical instability strip, as seen in the pulsational HR diagram (Fig. 1.6). RV Tauri stars are the brightest of the three types of Population II Cepheids, and have the longest periods, as evident from the period-luminosity relation diagram shown in Figure 1.7.

RV Tauri stars are further classified according to their photometric subtype (RVa and RVb) and spectroscopic characteristics (RVA, RVB and RVC) as described below. The median mass of RVa stars (0.45-0.52$M_{\odot}$) is found to be lower than that of RVb stars (0.7-1.8$M_{\odot}$), although this was from a sample with a relatively low number of RVb stars (Bódi & Kiss, 2019).

## Photometric characteristics and subtypes

RV Tauri stars are classified by their characteristic light curve that has an alternating 'deep-shallow' nature; a shallow minimum followed by a deep minimum as shown

in Figure 1.8. The shorter period between successive minima has been coined as the fundamental period $P_0$, while the period between successive deep minima as the double or 'formal' period $P_1$ (Pollard et al., 1996). However, some stars that have been classified as RV Tauri type have irregular light curves which do not always show this consistent alternating deep-shallow behaviour (*e.g.* U Mon, AR Pup, IW Car and R Sct). Thus, there can be some uncertainty as to whether to use the shorter period between successive minima of any type, or the longer period (Catelan & Smith, 2015). These inconsistencies in the alternating nature of the period can probably be explained by considering all the dynamical atmospheric effects that regulate the shape of the light curves (Wallerstein, 2002).

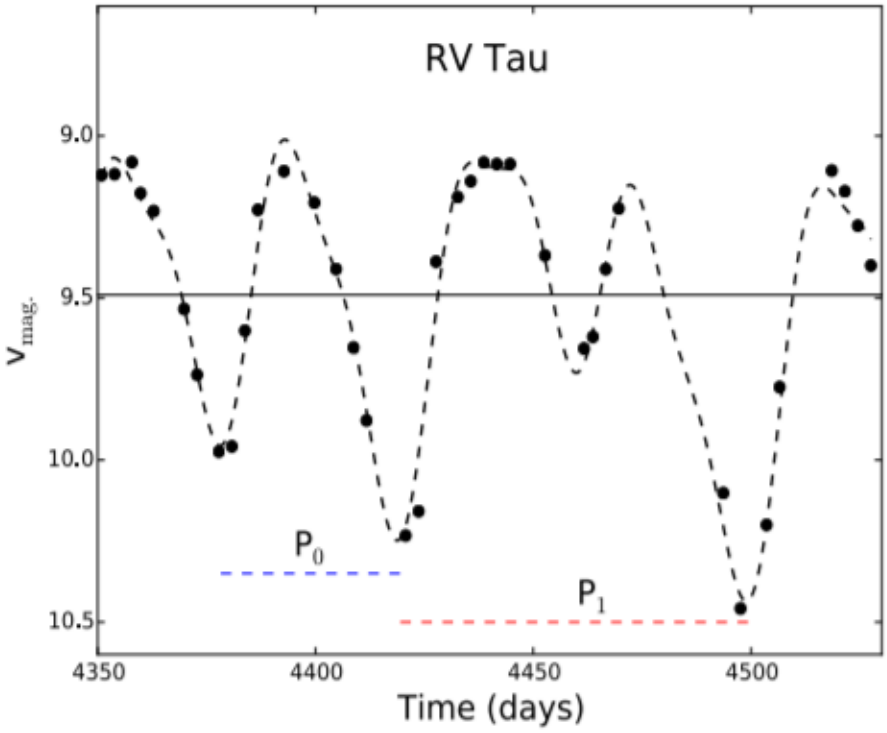


**Figure 1.8:** The prototype RV Tau light curve showing the characteristic, alternating deep and shallow minima. Figure by Manick (2018) based on data from the All Sky Automated Survey (ASAS) catalogue (Pojmanski et al. (2005)).

The positioning of the deep-shallow minima can also reverse or "flip" occasionally. Three RV Tauri stars, U Mon, UZ Oph and TT Oph, were analysed for their interchanges of the alternating amplitude in their light curves by Plachy et al. (2013). While all three stars showed this interchange on both long and short time scales, no periodicities in the changes were detected. These random cycle to cycle changes in the light curves of many RV Tauri stars make the detection of a true evolutionary change in their period more difficult (Percy et al., 1997).

Differences in photometric properties between globular cluster and field RV Tauri

stars have been noted by Zsoldos (1998). Similarities between RV Tauri and W Vir type stars have often led to them being classified as one or the other (Percy, 2007). Hence, discussions in literature on defining the basis of their classification are plentiful (Pollard et al., 1996).

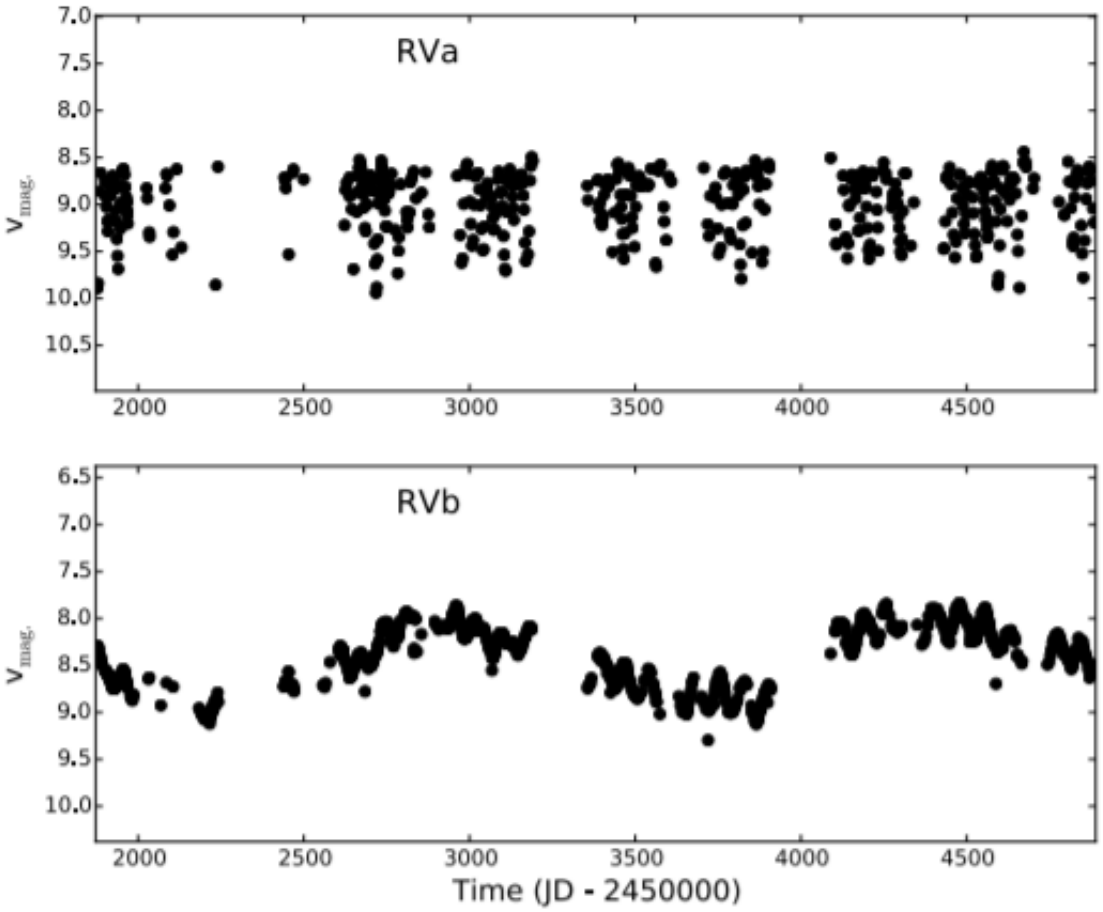


**Figure 1.9:** (Top) Light curve of RU Cen (RVa type), and (Bottom) IW Car (RVb type). Figure by Manick (2018) based on data from the All Sky Automated Survey (ASAS) catalogue (Pojmanski et al., 2005).

RV Tauri stars which show only short-term pulsational variations with a constant mean magnitude are classed as photometric RVa-type, while those with an additional long-term variation in their mean magnitude superimposed on the short-term pulsational variations, are classed as photometric RVb-type (see Preston et al. 1963; Lloyd Evans 1985; Zsoldos 1996; Pollard et al. 1996). The long-term variations as seen in the light curves usually have periods of the order of $\sim 600 - 2600$ days. Example light curves of both an RVa type and RVb type star are shown in Figure 1.9.

Pollard et al. (1996) suggest from their analysis of their $(B - V)$ and $(V - R)$ colour curves of RV Tauri stars R Sct (RVa) and U Mon (RVb), that the mechanism

for producing very deep minima in RVa stars might be different to that in RVb stars.

## Modelling the photometric variability

Over the years, many models have been proposed to explain the physical origin of the above mentioned photometric behavior of RV Tauri stars. Takeuti & Petersen (1983), Tuchman et al. (1993) and Fokin (1994) all suggest that the alternating "deep-shallow" nature of the light curve is the result of a 2:1 frequency resonance between simultaneously excited fundamental and first overtone radial pulsation modes. While it succeeds in explaining the regular alternating deep and shallow minima in the light curve, the model fails to reproduce the light curves of other known more irregularly pulsating RV Tauri stars. Pollard et al. (1996) employ a 'harmonic' ($f + 2f$) least-squares fit of fundamental frequency ($f$) and its first harmonic ($2f$) to reproduce the alternating deep-shallow (RV Tauri-type) light curve. They suggest that fixing the second period would preserve the characteristic light curve even outside the range of data, would result in a fit that may indicate the real physical phenomenon and provide some predictability.

Using numerical hydrodynamical models, Buchlar et al. (1987) and Plachy et al. (2018) claim the irregularities in the light curves are a consequence of low-dimensional chaos. Shenton et al. (1992) suggest a model in which simultaneous excitation of a radial and non-radial mode, where the period of non-radial mode is exactly twice that of radial mode, based on their study of the RV Tauri star AC Her.

The current leading model to explain the long-term RVb phenomenon is the binary dust-eclipse model, initially developed by Percy (1993) and Fokin (1994). Pollard et al. (1996) adapt a model of a binary periodically eclipsing by a circumbinary dust-torus (Waelkens & Waters, 1993), and propose that light and colour variations seen in RVb stars such as U Mon and AI Sco are a result of interaction between the binary components, as well as interaction with the previously ejected material as the system moves in its orbit. A more recent study which supports the dust obscuration model to explain RVb phenomenon is by Kiss & Bódi (2017). They suggest that by using fluxes instead of magnitudes, amplitude attenuation can be explained from periodic eclipsing of starlight by circumbinary disk surrounding the whole system.

A recent study of the RVb star AR Pup by Ertel et al. (2019) reveal a resolved circumbinary disk, leading the authors to suggest that long term variations in AR Pup are a consequence of variable scattering of starlight and variable disk illumination over the binary orbit. In the case of the RVa star RU Cen, the light curves show very regular variations and Pollard et al. (1996) notes that this regularity resulted in it being misclassified as an eclipsing binary in the past. A long term variability in radial velocity was detected and interpreted as being due to binary orbital motion by Maas et al. (2002). The presence of binarity and extremely processed circumbinary

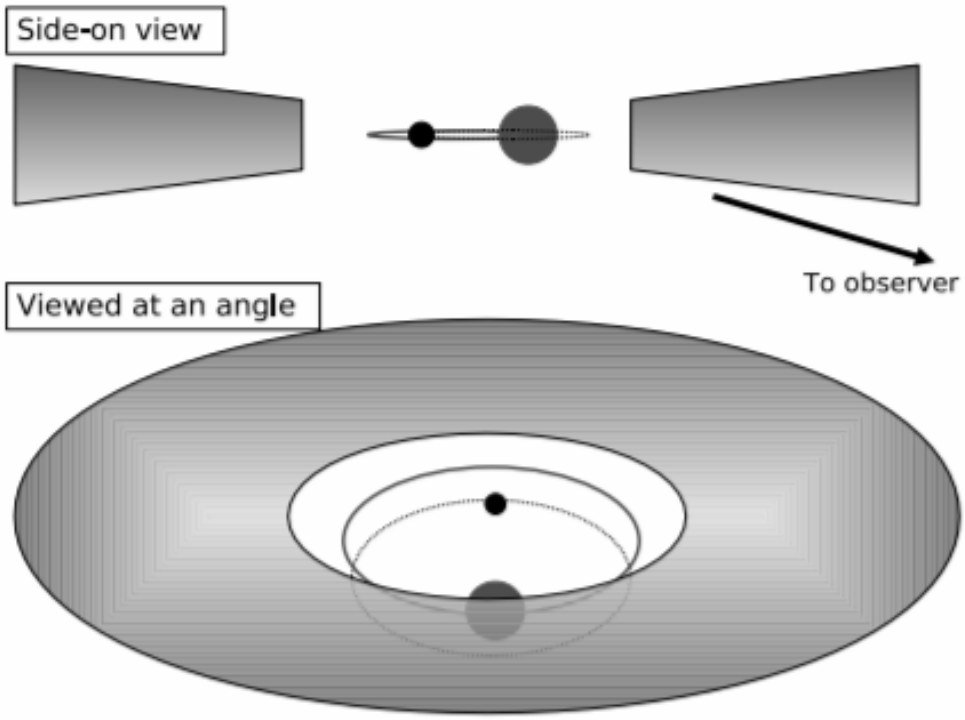


**Figure 1.10:** Dust obscuration model (Pollard et al., 2006). Depending on the line of sight of the observer, the RV Tauri star may be periodically eclipsed by the circumbinary dust-torus.

dust is strongly suggested by Gielen et al. (2007). The authors note an intimate relation between depleted photospheric chemistry and the presence of circumbinary disk, and also a likely relation between formation of circumstellar dust and binary interaction.

## Spectroscopic characteristics and classification

Spectroscopic studies over the years have further revealed the inhomogeneity of the RV Tauri class. The spectroscopic subclassification of RV Tauri stars that is generally adopted is RVA, RVB and RVB as catalogued by Preston et al. (1963). RVA stars are generally G-K spectroscopic type variables and show strong absorption lines but normal CN bands (Maas et al., 2002), with TiO molecular bands occasionally appearing at minimum phase of pulsation (Pollard et al., 1997). RVB stars are somewhat hotter Fp(R) variables whose spectral features include evidence of carbon and nitrogen abundance by the presence and strength of CN and CH bands at some phases where the photosphere is not too hot for the presence of these molecules (Gielen et al., 2007). RVC stars are Fp variables which have weak line spectra with occasional CN and CH molecular bands but not as enhanced as seen in RVB type

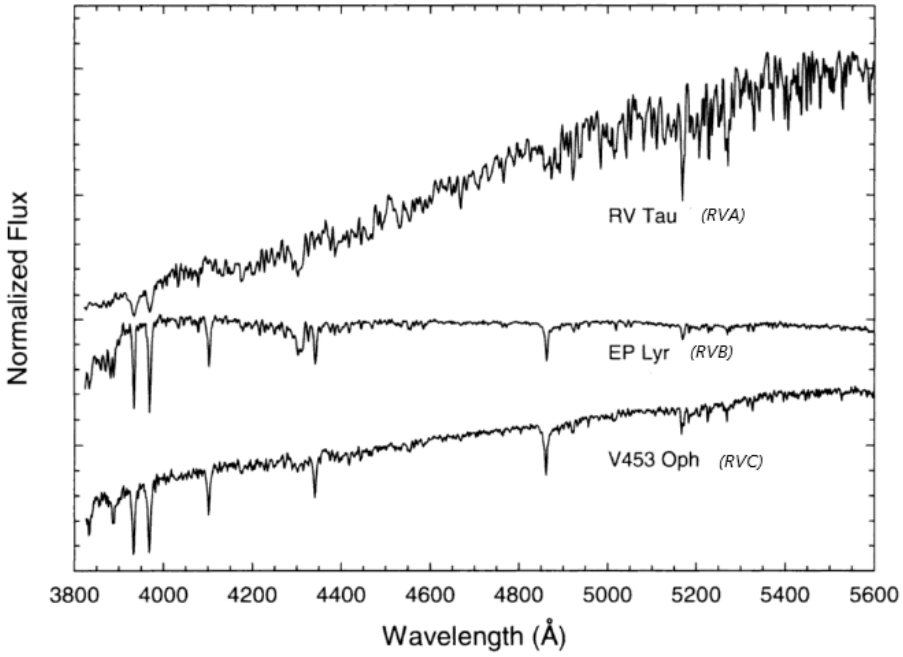


**Figure 1.11:** Spectra of RV Tau (RVA), EP Lyr (RVB) and V453 Oph (RVC) stars. Figure from Gray & Corbally (2009).

stars. A comparison of spectra of each spectroscopic type of RV Tauri stars is given in Figure 1.11. It is not clear why spectra of some RVA stars show the underabundance of some elements like Ti and Sc similar to that seen in spectra of RVB stars (Maas et al., 2005). For a detailed comparison of chemical abundances and depletion seen in RVA, RVB and RVC stars, we refer to Maas et al. (2005).

## The presence of shocks

The shock waves in the stellar atmospheres resulting from pulsations are not as well understood as some of the other properties of RV Tauri stars. Baird (1984) describes a shock as a phase lag between upper and lower atmospheric layers, where the lower layer pulses outwards while the upper layer falls inwards. A shock wave is produced as the two layers violently collide with each other. A numerical hydrodynamic shock wave model by Fadeyev & Gillet (2004) is recommended for a more detailed look at the shock structure and mechanism. The shock wave leaves two signatures on the spectra: absorption line "splitting" or doubling; and neutral helium (He I) or hydrogen-alpha (H$\alpha$) line emission despite the sufficiently cool photosphere for no such emission.

Gillet et al. (1990) suggest a model with two shocks per period for their spectral observations of RV Tauri stars R Sct and AC Her. They also calculate the accelerations associated with the primary and secondary shocks during each pulsation. The results of Pollard et al. (1997) who study eleven RV Tauri stars, are consistent with

the two shock waves propagating in the atmosphere per pulsation period. They note that the double or multi-peaked emission profile of the H$\alpha$ line seen in their sample is due to a combination of an emission component and an absorption component. Emission lines are a result of the de-excitation zone of the shock wave that propagates through the stellar atmosphere, while absorption lines are due to photospheric absorption, or H$\alpha$ self-absorption above the shock front. They also note that the variability of H$\alpha$ in the spectra of U Mon appears to have two sources: one from shock waves from short-term pulsations; and one is a consequence of the long-term RVb phenomenon.

## 1.4 Motivation for this thesis

In order the investigate further the long-term behaviour and stability of the periods in the RV Tauri stars, a photometric programme at the University of Canterbury Mt John Observatory has been established in association with the AAVSO to monitor a selection of these stars, with an emphasis of the "RVb" stars that possess the long-term period.

In Chapter 2 the photometric observations that were used in this thesis are presented and a description of the analysis techniques are given. The photometric results from the recent photometry, as well as the analysis of historic long-term AAVSO data, are presented in Chapter 3.

In addition to the photometric programme, 92 spectra of the brightest "RVb" target, U Mon, were obtained for this thesis, in order to make a detailed investigation of the current pulsational behaviour of this star. Chapter 4 contains details of the spectroscopic observations and methods of reducing and analysing them. Chapter 5 presents the results of this analysis, including the measured radial velocity curves, fitting of pulsation frequencies, as well as the investigation of the effects of shock waves in this star, as evidenced by the photospheric line doubling and line emission.

A conclusion for both the photometric and spectroscopic results is presented in Chapter 6.

# Chapter 2

# Photometry

This section gives a brief overview of the photometric data obtained and the analysis techniques used in this thesis. The aim of this analysis was to have as long a time baseline as possible to analyse the long-term brightness variations of the target RV Tauri stars, along with the short-term pulsations. Concurrent photometric and spectroscopic observations of the target stars were obtained where possible.

## 2.1 Photometric data

The photometric data in this thesis were obtained from the American Association for Variable Stars Observers (AAVSO) data archive. These data were obtained with the 0.6 m Optical Craftsman (OC) telescope at the University of Canterbury Mt John Observatory (UCMJO) in New Zealand and with the Bright Star Monitor stations (BSM) at two observatories in Australia. Photometric CCD images taken with the Johnson photometric system's $V$ and $B$ filters were chosen for short-term pulsation analysis of all targets as well as plotting $(B - V)$ colour curves.

For long-term period variation analysis, the AAVSO's visual band data was used. Most of the 20th-century observations were ocular estimates, *i.e.* the visual part of the electromagnetic spectrum, and Johnson photometric system's $V$ filter comes closest to matching these visual observations Zissell (2002).

### 2.1.1 AAVSO

The AAVSO, formed in 1911, is an international organization of amateur and professional astronomers from over 100 countries who are interested in variable stars in general. The AAVSO International Database (AID) has an archive of over 34 million photometric observations of variable stars spanning over more than 100 years. It has well observed visual light curves of at least 24 RV Tauri stars, most of which are between 30 and 75 years in length, including the target stars in this thesis. Thus it

serves as an excellent database for studying long-term variability in these stars. The visual magnitude estimates of variable stars reported in AID are obtained over the decades by various observers using telescopes, binoculars or naked eye observations of stellar brightness and comparing to that of previously established comparison stars within the field of view. However, the long term visual data are subject to limitations, as noted by Percy & Abachi (2013), that could influence Fourier analysis:

- Seasonal gaps in the data which produces aliasing in the Fourier spectra
- The Ceraski effect, a physiological effect that produces aliasing at 365.25 days (*i.e.* "when two stars of equal brightness are aligned so that the line-of-stars is perpendicular to the line-of-eyes, the observer may see the upper star brighter than the lower one".)
- The variability in the light curve if the assumed magnitudes of visual reference stars have changed over time, although AAVSO strives to minimize this effect.
- Variable visual acuity/sensitivity from observer to observer.

Visual inspection of the homogeneity of the light curve is a good way to estimate if a good comparison sequence was available throughout the star's observational history (see Kafka & Templeton (2015) for more details).

### 2.1.2 Mt John data

The University of Canterbury Mt John Observatory is located near a small South Island town in New Zealand called Lake Tekapo. Its geographic coordinates are 43°59.20'S, 170°527.90'E at an elevation of 1029 m. On average 20% of nights at Mt John are photometric according to the AAVSO website. The photometric images were acquired with the Optical Craftsman (OC) telescope (Figure 2.1) owned by the University of Canterbury (UC). The telescope is robotic and is operated in a queue-scheduled manner by the AAVSO in association with UC. The OC is a Cassegrain reflector, has a fork mount with the primary mirror 24 inches (0.61 m) in diameter and with a focal ratio of f/14.8. The CCD in use is FLI Proline PL09000 with $BVgri$ filters.

### 2.1.3 BSM data

Both BSM stations in Australia are robotically controlled refractor telescopes capable of multi-filter observing of stars in the magnitude range $V = 2.0 - 13.6$. The BSMs support automatic calibration of images, which are then directly uploaded to the AAVSO database. BSM Berry resides in Perth, whereas BSM South is stationed

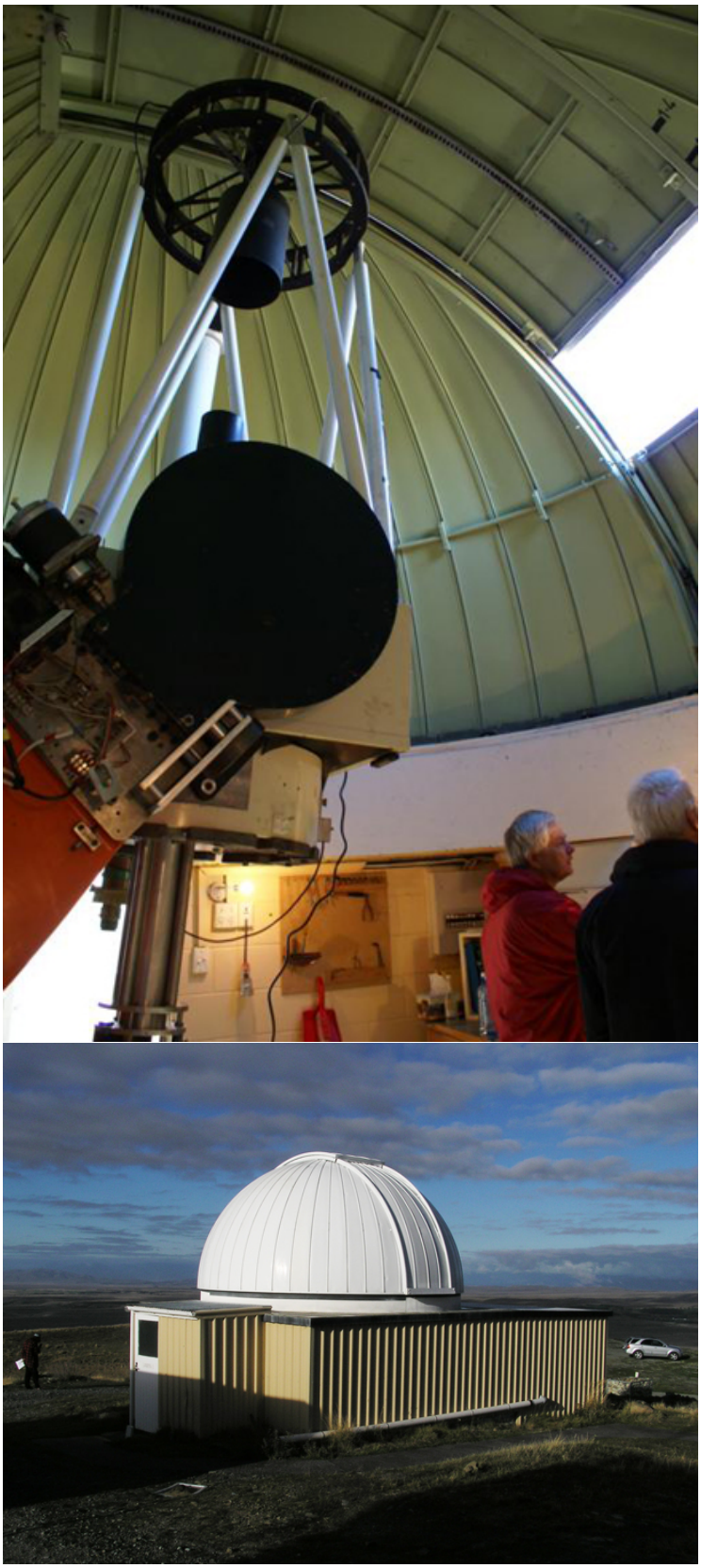

**Figure 2.1:** The Optical Craftsman fork-mounted 0.61-m telescope (top) and telescope room and dome (bottom) at Mt John. Image courtesy: www.AAVSO.org

in New South Wales. Both are in an anti-correlated weather pattern setting (east – west coast) with each other.

## 2.2 Differential photometry with VPhot

The AAVSO's web-hosted aperture-based photometry tool VPhot was used in this thesis. AAVSO's webpage mentions it as a powerful tool that can perform differential photometry with all the basic photometry functions such as stacking, aligning, annuli adjustment, time-series analysis and high quality algorithms specifically designed to analyse variable stars. AstroImageJ (Collins & Kielkopf, 2013) was also used for the same initial data set to compare the ease of use and efficiency of obtaining the differential photometry results. It was found that VPhot had faster processing, and better precision and versatility, hence was the primary photometric reduction tool used in this work.

All the photometric CCD images were automatically flat-fielded, so there was no need for an initial flat-fielding procedure. The FITS images were uploaded from the AAVSO archive to the AAVSO VPhot site to be analysed. To perform differential photometry, the target star, the check star (used as a quality control measurement) and comparison stars (stars with known or fixed magnitude to compare the brightness of target star to) were selected in the same field by using AAVSO's online catalogue of comparison stars and sequences. A sequence of comparison and check stars for each target was saved and used to automatically identify stars and perform photometry in each subsequent image. A typical CCD image analysed within VPhot is shown in Figure 2.2.

VPhot can automatically compute the photometric aperture radius by calculating the average full width at half maximum (FWHM) of the target star profile, times a constant that depends on the particular target star, for all measurements in the sequence. The resulting summary of time-series photometry is substantial and highly examinable to be able to detect and rectify any problems easily, which compensates for the otherwise fully-automated analysis well.

Problems such as bad tracking, hot pixels and intermittent clouds, *etc.* are easily detectable and removable by examining the discrepant data points in the output time-series graphs. A file with Julian Dates, airmass, star magnitudes and uncertainties, signal-to-noise ratio, FWHM, skyglow and Max ADU (see Figure 2.4) was exported as a text file to be analysed for periodicities in each dataset. Further details of the differential photometry reduction procedure can be found in the VPhot Users Guide available on the AAVSO website.

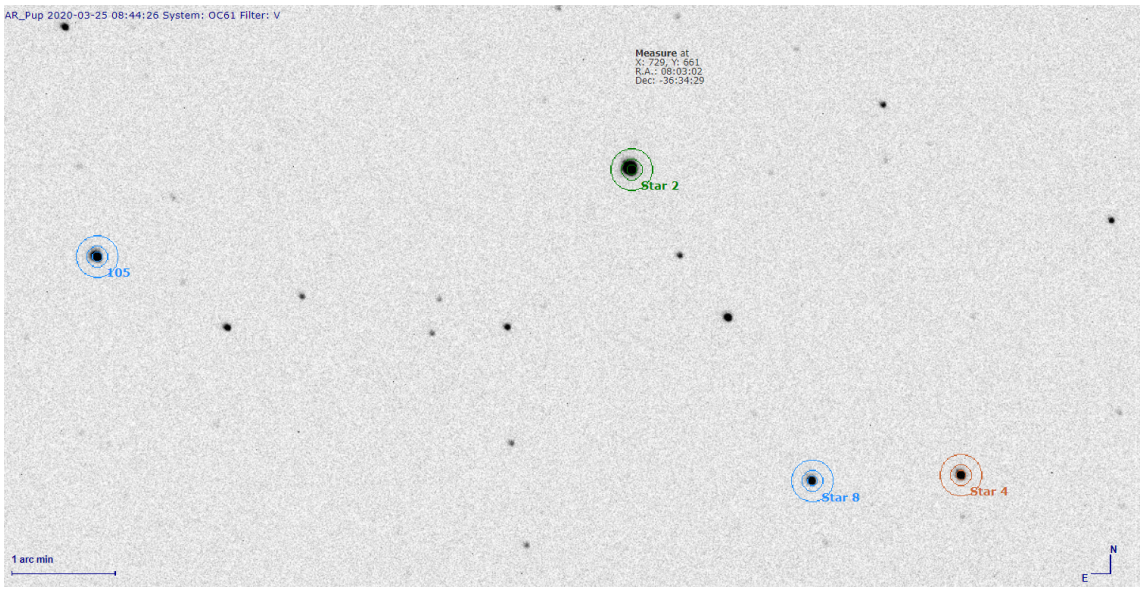


**Figure 2.2:** An example of a CCD image in `VPhot` with target star (green), check star (orange) and comparison stars (blue).

## 2.3 Frequency analysis and least-squares fitting

As we need to search for frequencies of the light output of a star due to pulsational effects, a Fourier transform is needed to analyse the photometric data in the frequency domain. This was done using the software package Period04 (Lenz & Breger, 2004). The software is based on a discrete Fourier transform algorithm (Scargle, 1982) instead of fast Fourier transform algorithm. This is due to the fact that astronomical time-series data sets are usually not equally spaced due to observational constraints.

Output of Fourier analysis is usually a plot of power (amplitude squared) or amplitude versus frequency. Such a graph is called a periodogram and it reveals the dominant frequencies that are present in the data set, which are likely to be directly related to the star's pulsations.

`Period04`, a hybrid program written in Java/C++, is particularly useful for statistically analysing large astronomical time-series data containing gaps, hence ideal for this research. Its user-friendly interface allows the extraction of multiple independent frequencies from the signal, calculation of formal uncertainties and allows multiple-frequency fits to the light curve with a combination of least-squares fitting and a discrete Fourier transform algorithm (Lenz & Breger, 2014). The general frequency analysis procedure is documented in the `Period04` user guide (Lenz, 2005).

Time series data for the target stars obtained from the `VPhot` differential photometry was imported into `Period04`. The data consisted of two columns containing Julian dates and the corresponding visual magnitudes. The light curves (a plot of

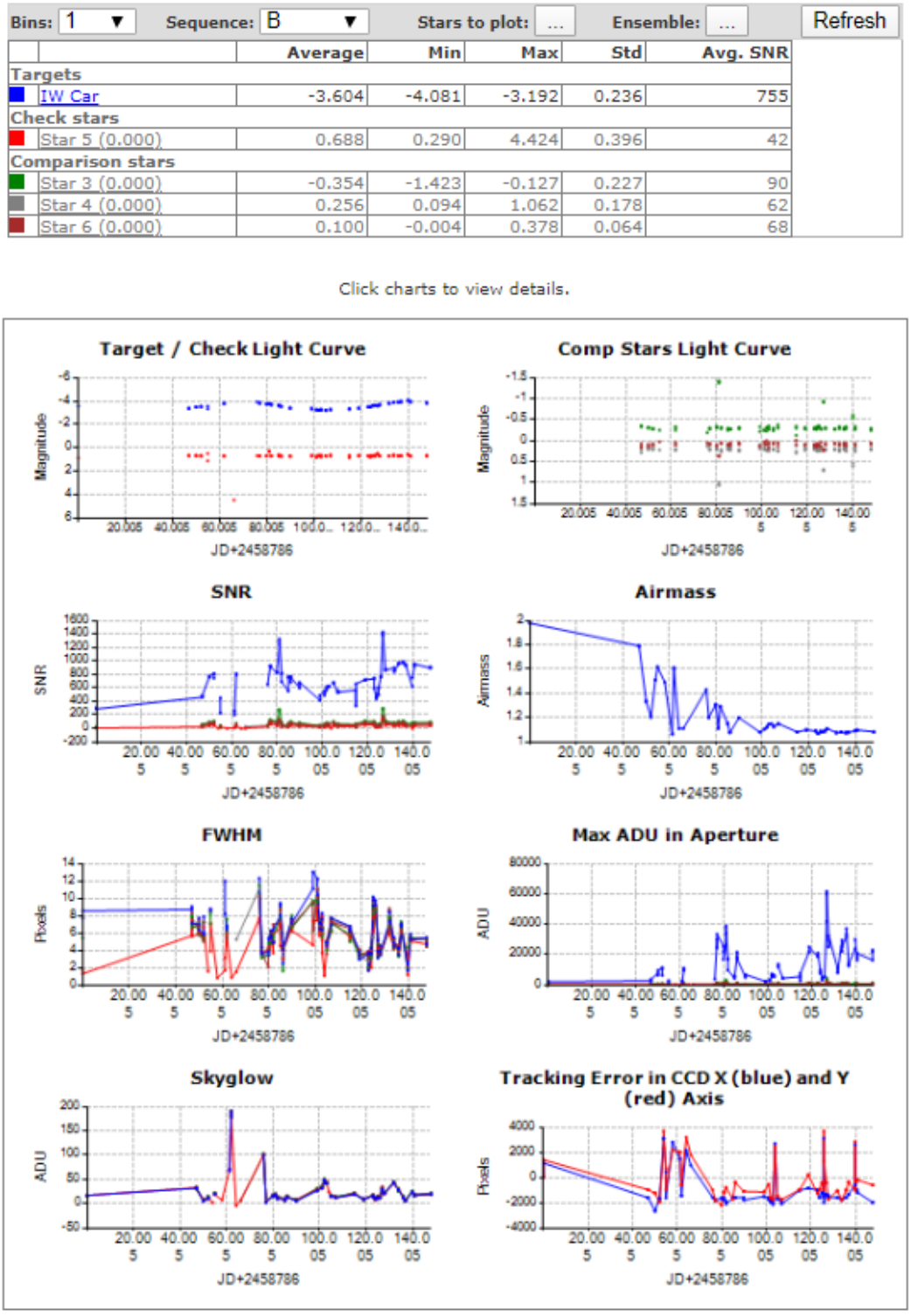


**Figure 2.3:** A screenshot of the differential photometry analysis window in `VPhot`

visual magnitude versus time) were produced and inspected for discrepant data points and/or points that lie very far from the nearest collection of data points. Such points were omitted in order to avoid extra aliasing in frequency plots and inconclusive least-square fits.

| JD | Airmass | RU Cen | Err | SNR | FWHM | Skyglow | Max ADU |
|---|---|---|---|---|---|---|---|
| 2458605.11348 | 1.04685 | 8.742 | 0.003 | 322 | 1.398 | 122.498 | 16299 |
| 2458605.11612 | 1.04944 | 8.730 | 0.003 | 327 | 1.256 | 124.082 | 19922 |
| 2458606.04976 | 1.03682 | 8.710 | 0.003 | 326 | 1.372 | 125.548 | 15418 |
| 2458606.05243 | 1.03531 | 8.743 | 0.003 | 316 | 1.539 | 128.182 | 14363 |
| 2458606.05505 | 1.03401 | 8.734 | 0.003 | 319 | 1.665 | 125.515 | 11466 |
| 2458608.04788 | 1.03499 | 8.689 | 0.003 | 319 | 1.667 | 118.198 | 11122 |
| 2458608.05045 | 1.03377 | 8.696 | 0.003 | 320 | 1.628 | 115.913 | 10930 |
| 2458608.05301 | 1.03273 | 8.694 | 0.003 | 318 | 1.855 | 118.097 | 8940 |
| 2458611.03965 | 1.03500 | 8.667 | 0.003 | 333 | 1.522 | 119.802 | 15536 |
| 2458611.04223 | 1.03378 | 8.729 | 0.003 | 332 | 1.444 | 111.588 | 15093 |
| 2458611.04478 | 1.03273 | 8.682 | 0.003 | 339 | 1.452 | 113.211 | 18784 |

**Figure 2.4:** A sample output file of the differential photometry analysis in `VPhot`.

Once the data had been prepared for Fourier analysis, a suitable frequency range for Fourier spectra was defined according to the known pulsational frequencies from the literature for the target stars. We used $(0.0 < f < 1.0)\,\mathrm{d}^{-1}$ since all known RV Tauri stars pulsate within this frequency range. In any case, the upper bound of this range is set lower than the Nyquist frequency (mean sampling frequency) which places a limit of the highest frequency typically able to be extracted from the data set. For unequally-spaced, time-series datasets, such as those used in this thesis, the Nyquist frequency is not uniquely defined but is computed from the time-difference of consecutive measurements by neglecting large gaps in the data (Lenz & Breger, 2014).

Fourier analysis requires that the data does not contain a zero-point shift in time, otherwise additional aliasing/peaks centered at $f = 0.0\,\mathrm{d}^{-1}$ would appear and may even dominate the whole spectrum. The software subtracts the average zero-point before running the analysis. The temporal span of the measurements (the time difference of the last and first measurement) defines the frequency step size, that is the frequency resolution of the Fourier spectrum. It was set to "high" for good sampling to ensure that no frequency was missed.

Weights for the archival data set not well known and hence all were assumed to have equal values to maintain consistency between the different contributors to the archival dataset. Weights, if known (for instance, for the recent photometry) for each data point, could be taken into account in the Fourier computation for increasing the accuracy of frequencies.

After carrying out the Fourier analysis, the strongest frequency was obtained and subsequently selected for performing a least-squares fit to the data set. This fitting procedure is a Levington-Marquardt non-linear least-squares fitting procedure (Gavin, 2013), based on the `curfit` routine from Bevington (1969). It makes a least-squares fit to the non-linear function with a linearization of the fitting function.

The least-squares fits are calculated through `Period04` that operates on the

sinusoidal fitting formula

$$f(t) = Z + \sum_i A_i sin(2\pi(\omega_i t + \phi_i)) \tag{2.1}$$

where $Z$ is the zero point in time, $A$ is the amplitude, $\omega$ is the angular frequency ($\omega = 2\pi f_i$, where $f$ is frequency) and $\phi$ is the phase of the sinusoid.

Once fitted, the dominant frequency was then subtracted from the data set. Fourier analysis was performed again on the residuals to find the next strongest frequency. This cycle was repeated using the previous iteration's residuals until all significant frequencies were extracted. A frequency was deemed to be significant if it reached a certain signal-to-noise level in the amplitude of the periodogram (Lenz & Breger, 2014). In this way, in each run one dominant frequency was found and subtracted from the original data via a least-squares fit to find the next dominant one in the mix of the entangled frequencies.

The above procedure is called 'pre-whitening' and is an iterative procedure of detecting a signal, removing this sinusoidal signal from the data by Fourier least-squares fitting, then analysing the residuals until no further significant frequencies are found in the data set. The results of the frequency analysis of the target stars are presented in Chapter 3.

### 2.3.1 Significance of frequencies

Noise can contaminate a signal to form spurious frequency peaks in a Fourier periodogram. Such peaks can be misleading with regards to a physical phenomenon and cause problems with identification of the true frequencies. A useful criteria is that the peaks which have a signal-to-noise ratio (SNR) above 4.0 in a typical data set are usually deemed worth investigating. This value is based on empirical results from observational analyses by Breger et al. (1993) and numerical simulations by Kuschnig et al. (1997).

`Period04` outputs the SNR for frequencies in data sets of the target stars. It is computed as the ratio of the signal which is the amplitude of highest frequency obtained and the noise which is the average amplitude of the residuals in a frequency range that encloses the same obtained frequency after it has been pre-whitened (Deb et al., 2009). The limit of SNR $> 4$ is not a hard one, and we incorporated a flexible limit depending on the star and considering the observational errors in our observational data sets.

### 2.3.2 Estimation of parameter uncertainties

In a periodogram, the uncertainty in a frequency peak of a star can easily have (and usually does have) many other superposed uncertainties from signals that arise from

various factors. These include, but are not limited to: white noise; uncertainties introduced through data reduction; human errors; equipment errors; atmospheric scintillation for ground-based observation; as well as stellar granulation (Kallinger, T. et al., 2014). These sources of noise mentioned, as well as others depending on the respective acquisition, reduction and analysis techniques used, increases the uncertainty in a real frequency and its corresponding amplitude and phase.

The software package `Period04` provides tools for the calculation of parameter uncertainties. This helps us to understand the goodness of a fit to our data points. We use Monte Carlo simulations as they are a reliable and widely used technique to determine the uncertainties. The essential idea is to obtain numerical results, and hence estimates of uncertainties, by repetition of random sampling. The significant frequencies and corresponding amplitudes and phases that were found by least-squares calculation are used as the starting point for the simulations. A set of time strings are generated in which the times of every set's data points are the time of the original time string data and the magnitude (of a parameter) of data points are magnitudes calculated by the last least-squares fit plus residuals. For each simulation, along with the parameters, the fitting procedure also outputs an error matrix from which uncertainties are calculated. The higher the number of simulations, the more reliable the calculated uncertainties.

## 2.4 Wavelet analysis

A wavelet transform is a method for period analysis in time-series data. It calculates how significant and how stable a star's period(s) and amplitude(s) is during the time-span of the observation. For the analysis we use the AAVSO's tool `VStar` (Benn, 2012). The program is based on a Weighted Wavelet Z-Transform (WWZ) from Foster (1996).

For a set of time-series data, $x(t)$, its wavelet transform is given by

$$W(\omega, \tau; x(t)) = \omega^{1/2} \int x(t) f^*(\omega(t-\tau)) dt \tag{2.2}$$

where $\omega$ is scale factor (test frequency), $\tau$ is the time shift or "lag", function $f$ (where $f^*$ is the complex conjugate) is the "mother wavelet" which dictates how the signal varies with frequency, time and position in the light curve. The mother wavelet can be any function and both waveform and time-varying weighting (like a sliding window) function can be included to find periodicities and time-dependence of the signal (Templeton, 2004).

For an adequate measure of the time evolution of a period and its amplitude, the length of the data set must be long (around 50 times the period of interest) and well-sampled. For example, if the time-span of observations is 2000 days, it would

not be meaningful to measure variability of a period of 500 days where the wavelet window covers only 4 cycles. The width of the window is user defined and affects the period and temporal resolution of the wavelet transform.

The results of the wavelet analysis of two target stars which were sufficiently well-sampled for this type of analysis are presented in Chapter 3.

# Chapter 3

# Photometry Results

The chapter presents a summary of the photometric data obtained and used in this thesis, and its analysis using both Fourier techniques and wavelet analysis. The photometric observations at UCMJO and BSM are given in Table A.1-A.10.

## 3.1 Target RV Tauri stars

The RV Tauri stars chosen as targets for observation and analysis are listed in Table 3.1. RV Tauri stars are defined photometrically as either RVa stars which have a constant maximum magnitude, or RVb stars, which have a long-term variation in the maximum magnitude (Preston et al., 1963).

**Table 3.1:** RV Tauri target stars, coordinates, visual magnitude range, mean visual magnitude and RV Tauri type.

| Star | RA (h m s) | DEC (° ′ ″) | mean visual magnitude | visual mag range | RV Tauri type |
|---|---|---|---|---|---|
| U Mon | 07 30 47 | -09 46 37 | 6.4 | 5.1 – 8.4 | RVb |
| AR Pup | 08 03 02 | -36 35 48 | 9.8 | 9.1 – 10.9 | RVb |
| IW Car | 09 26 53 | -63 37 49 | 8.4 | 7.5 – 9.7 | RVb |
| RU Cen | 12 09 24 | -45 25 34 | 8.9 | 8.2 – 10.2 | RVa? |

## 3.2 Light and colour curves

Light curves for the target RV Tauri stars were produced using visual data to search for long-term light modulations and short-term pulsational variations. In addition, $V$ and $B$ band photometric data from UCMJO was used to examine the short-term pulsational variations. Visual data was utilized in the case of unavailability of photometric $V$ band data. Visual estimates in the AAVSO database typically

**Table 3.2:** Time span and number of observations of each target RV Tauri star from the AAVSO archive (visual data), the BSM photometric telescopes and the UCMJO OC 0.6-m telescope.

| Star | time span of observations | total time span | number of data points |
|---|---|---|---|
| AAVSO visual observations | | | |
| U Mon | 1945–2019 | 75 years | 41655 |
| AR Pup | 1969–2019 | 51 years | 1270 |
| IW Car | 1966–2019 | 54 years | 4658 |
| RU Cen | 1954–2016 | 63 years | 278 |
| BSM $V$ photometric observations | | | |
| AR Pup | 21/11/2019–12/02/2020 | 84 days | 62 |
| IW Car | 08/09/2019–21/01/2020 | 135 days | 50 |
| RU Cen | 01/05/2019–21/01/2020 | 266 days | 134 |
| UCMJO OC $B$ and $V$photometric observations | | | |
| AR Pup | 30/11/2019–24/03/2020 | 116 days | 78 |
| IW Car | 14/12/2019–24/03/2020 | 102 days | 92 |
| RU Cen | 09/12/2019–24/03/2020 | 107 days | 90 |

have a precision of 0.1 magnitudes, and 0.01 magnitudes for photometric $V$ and $B$. Times of observations is in Julian Date (JD) with a typical precision of a hundredth of a day for historical visual data sets, and tenth of a minute for recent $B$ and $V$ filter observations. It is noted that the visual photometric data from the AAVSO International Database (AID) used in this thesis extends a few years longer than that of previous studies such as Percy & Kim (2014) and Percy (2015).

Table 3.2 gives a summary of the number of data points and the time span of the data in the AAVSO archive for each target RV Tauri star. The AAVSO visual data is described as "Validated" or "Prevalidated" which refers to the data point being validated manually by a human, or through a series of checks by a computer algorithm, respectively. The long-term AAVSO visual light curves are plotted together in Figure 3.1.

The number of data points and the time span of the recent $V$ photometric BSM data and the recent $V$ and $B$ photometric UCMJO data from the OC 0.61-m telescope is also listed in Table 3.2. Unfortunately, the images from recent $V$ and $B$ filter photography of U Mon at UCMJO were largely found to be saturated rendering them unusable for photometry, thus only the long-term AAVSO dataset was available for analysis.

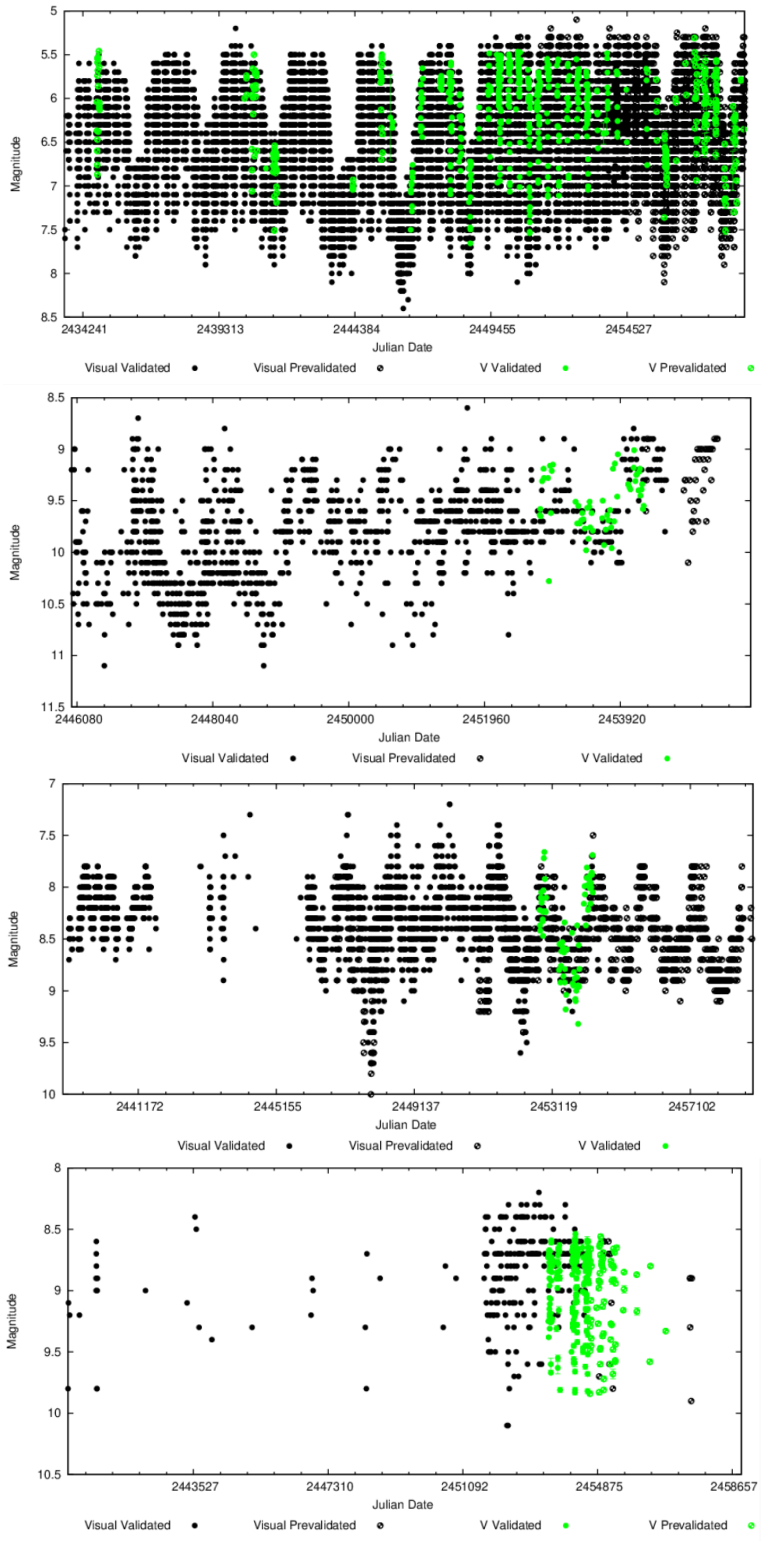


**Figure 3.1:** Long-term visual light curves from the AAVSO archive for (from top to bottom): U Mon, AR Pup, IW Car and RU Cen. Visual data is plotted in black and Johnson $V$ in green.

### 3.2.1 U Mon

On examining U Mon's light curve (Fig. 3.1, top), one can easily see a long-term "dip" repeating itself roughly every 2500 days which is consistent with the known long-term visual period of 2475 days (Percy, 1993) and its "RVb" classification. This long-term behaviour diminishes or disappears in both visual and $V$ data for about two long-term cycles from JD $2450000 - 2455000$, and seems to reappear. The cause of this is under investigation. One proposed model for the long-term photometric variations is cyclical dust obscuration as the pulsating star orbits in a binary system that has a circumbinary dust disk. Variable long-term photometric changes would therefore indicate variable dust obscuration – an effect which could be investigated further with more detailed filtered photometry.

The long-term maxima are fairly flat. Perhaps also worth noticing is that the overall brightness gradually decreases from the start until the middle of the graph then increases, which might be indicative of a longer trend than the length of the data set i.e. 75 years. Currently the star is at the maximum of its long-term variation.

### 3.2.2 AR Pup

In the visual light curve of AR Pup given in Fig. 3.1, (second to top), the time between the first two minima can be estimated as roughly 1200 days, which is close to the literature value of 1194 days (Percy, 2015). This is indicative of its RVb classification. The visual magnitude amplitude steadily decreases close to recent observations. This could mean that there exists a much larger period than the length of the data set itself, i.e. 26 years, or that the mechanism producing the long-term variations, possibly dust obscuration, is changing (in this case, weakening) with time.

The light curves produced using recent UCMJO $B$ and $V$ photometry of AR Pup (Fig. 3.2) show one cycle of the characteristic RV Tauri alternating deep-shallow-deep minima. However, previous photometry from Pollard et al. (1996) results show that this alternating behaviour doesn't repeat every cycle and appears somewhat irregular. The authors note that "the star could be experiencing 'flips' of the two minima", causing the inconsistently alternating deep-shallow minima. The overall $V$ light curve is almost a magnitude dimmer than the $B$ light curve. The $(B-V)$ colour curve (Fig. 3.2 bottom) also cleanly shows one cycle of the alternating deep-shallow minima, with a mean value around $(B-V) \sim 0.8$. It should also be noted that the bluest $(B-V)$ colours occur on each rising branch of the light curve which is a characteristic previously reported for other RV Tauri stars (Pollard et al., 1996) which is also the phase at which the shock waves are reported to be strongest.

### 3.2.3 IW Car

A total of 4658 visual observations are recorded from IW Car in a span of more than 60 years (see Fig. 3.1, third from top). The time between two successive minima is roughly 1500 days which matches the established period for this RVb star in the literature (Giridhar et al., 1994). The available $V$ data tracks the visual data well. Despite the two major gaps in data between JD 2441500 and 2446250, we use the data set in its entirety for Fourier analysis and least-squares fitting. This is because considerable observations exist before the first gap seen in data which could prove useful for searching for longer periodicities. Another feature noticeable in the visual light curve is the large dip in brightness that is observed around the middle of the light curve at about JD 2447800.

A plot of recent $B$ and $V$ photometry and the $(B-V)$ colour curve for IW Car is shown in Fig. 3.3. The $(B-V)$ colour curve is not quite as clean as AR Pup's colour curve, and shows some scatter. In contract to AR Pup, IW Car's mean colour is much bluer at $(B-V) \sim -0.05$.

### 3.2.4 RU Cen

Photometric data of RU Cen is sparse compared to other stars in this work. While the time span is quite large (with the first observation in 1954), only about 300 visual observations are recorded in AID for this star. Examining RU Cen's light curve (see Fig. 3.1, bottom), it is apparent that the majority of both visual and $V$ observations are clustered in a time span of about 4000 days ($sim$10-years) of the light curve. Visual data does not reveal any straightforward light curve behaviour. We used all the available visual observations for Fourier analysis and least-square fitting, keeping in mind that the longest period found would have the highest uncertainty. The AAVSO photometric $V$ magnitude data in green (Fig. 3.1, bottom) displays a seemingly regular variation. Although a long term variation is not seen in either $V$ or visual AAVSO data, supporting RU Cen's RVa classification, Percy (2015) report a long secondary period of 561 days.

Fig. 3.4 shows the recent $B$ and $V$ light curves, and $(B-V)$ colour curve. These recent light curves are indicative of RV Tauri-type deep-shallow pulsations, although the data to trace the depths of consecutive minima are sparse. The $(B-V)$ shows some scatter, with a mean value around $\sim 0.10$, somewhat similar to IW Car. Like AR Pup, the colour curve for RU Cen displays the bluest colours during the rising branches of the light curve.

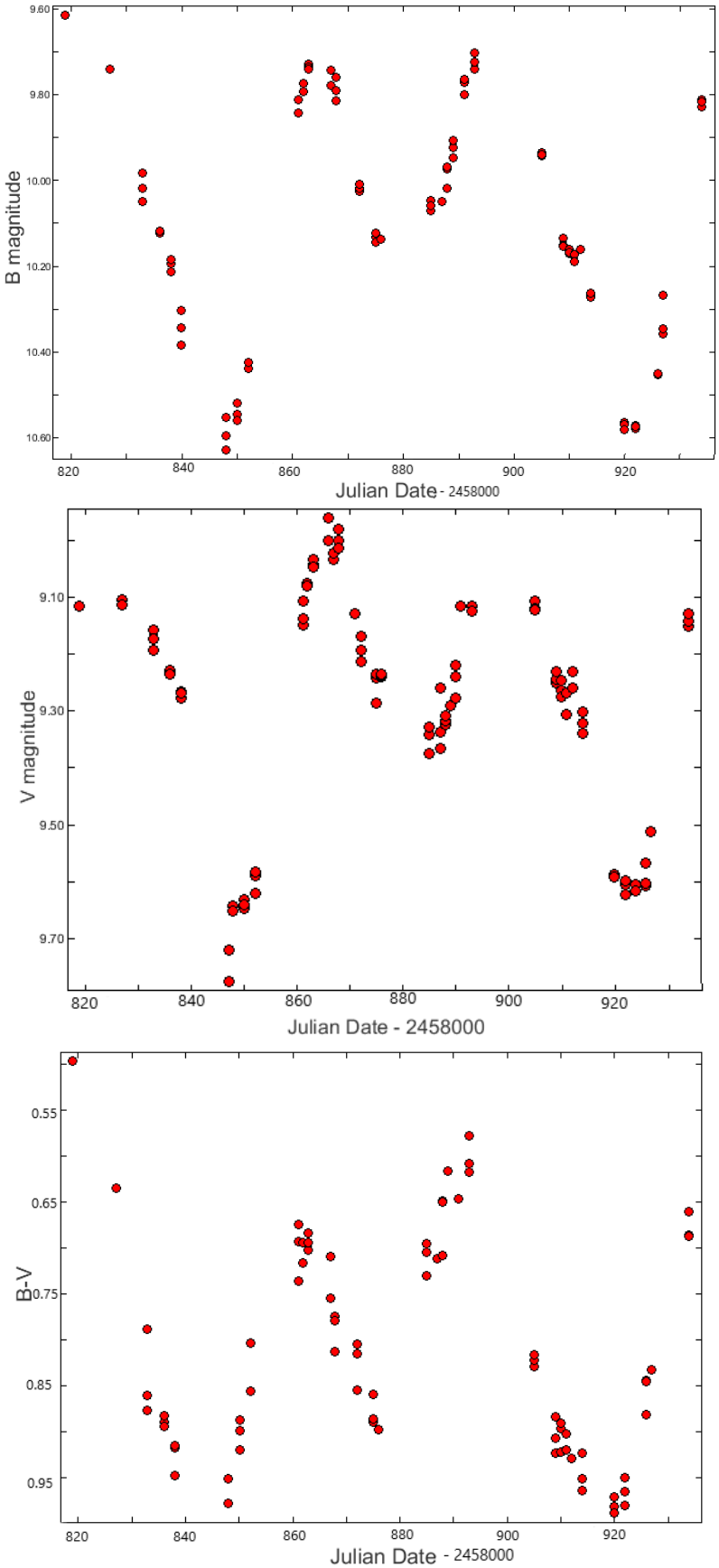


**Figure 3.2:** Recent $B$, $V$ and $(B-V)$ curves of AR Pup produced using `VPhot` differential photometry.

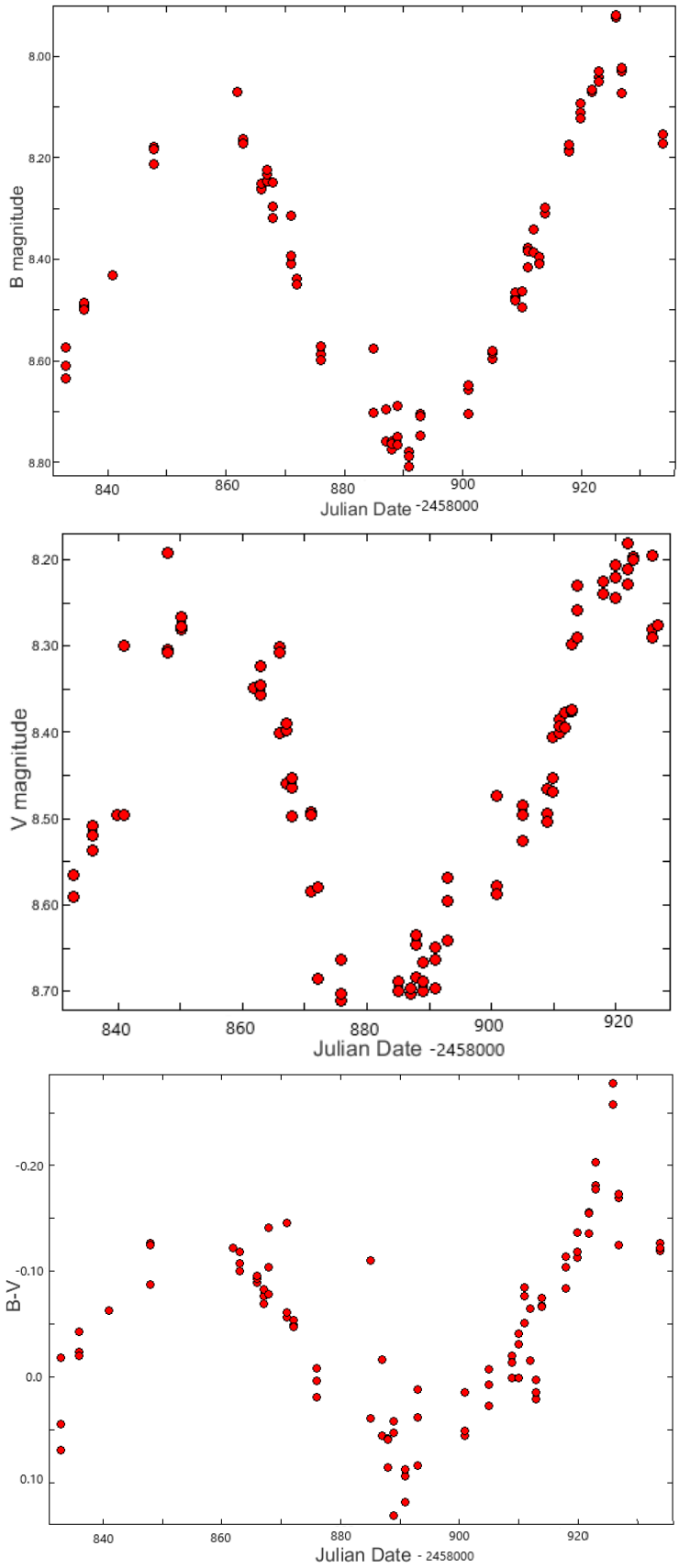


**Figure 3.3:** Recent $B$, $V$ and $(B-V)$ curves of IW Car produced using `VPhot` differential photometry.

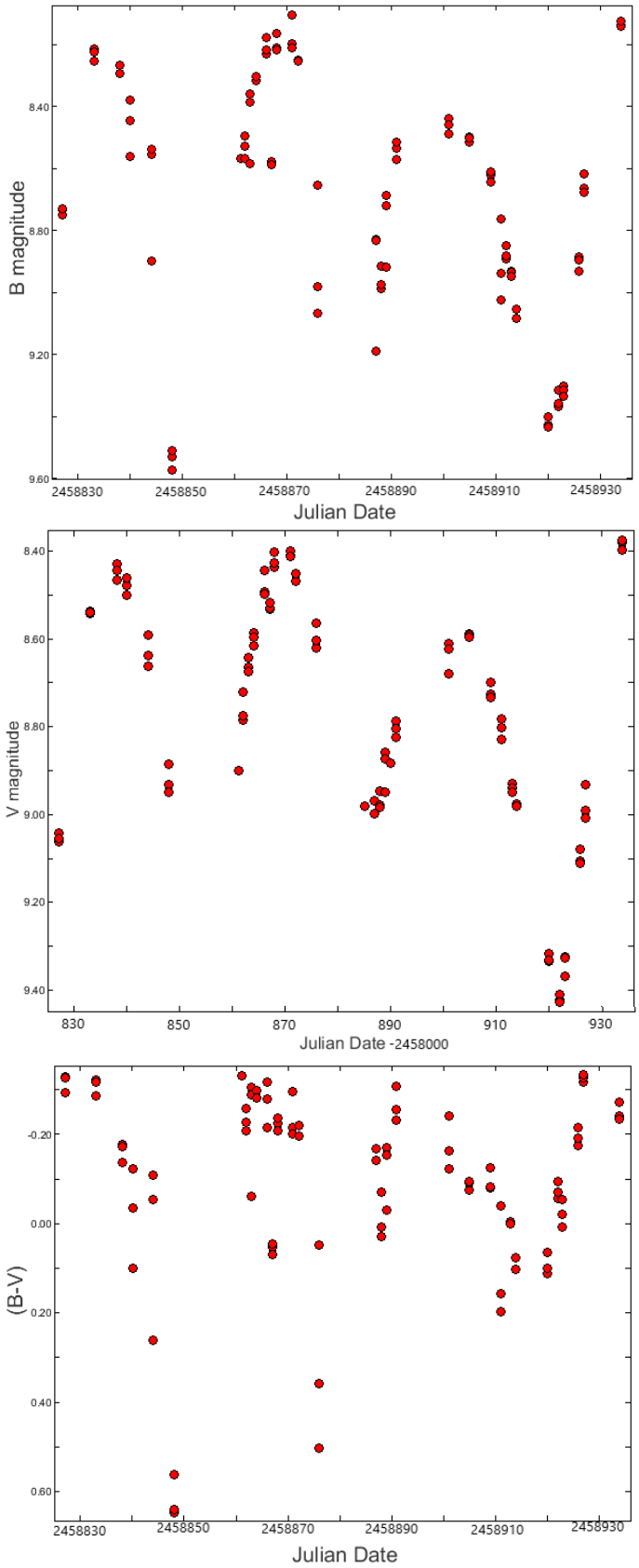


**Figure 3.4:** Recent $B$, $V$ and $(B - V)$ curves of RU Cen produced using `VPhot` differential photometry.

## 3.3 Periodograms

The periodograms shown in this section result from the Fourier analysis and frequency removal method using `Period04`, as discussed in Section 2.3. The dominant frequencies in the periodograms are marked with an arrow and their least-squares Fourier-fitted parameters such as period, amplitude, phase and noise level are stated in least-squares fit tables in this section.

As expected, aliasing is stronger in periodograms of stars with sparse data. As has been noted in papers such as Kiss et al. (2006) and Percy & Khatu (2013), the frequency peaks in RV Tauri photometry with large time spans of data are not sharp but complex, which makes it difficult to identify an exact period. The strongest peaks (periodicites) found are in fact in a peak envelope, with slightly shorter peaks very close on either side of strongest one. This complex peak structure may be due to aliasing, stellar convection-pulsation interactions as suggested by Percy & Khatu (2013), or period changes over time (see Section 3.4).

In this work, the peak with highest power in each periodogram is selected for least-squares fitting.

### 3.3.1 U Mon

Periodograms for the U Mon visual photometry are shown in Figure 3.5. The first extracted period of $2436 \pm 1$ days found for U Mon is in reasonable agreement with the periods of 2427 days and 2475 days from literature values (Percy (1993); Percy (2015); Percy et al. (1991), respectively. Pollard et al. (2006) obtained an orbital solution using radial velocities, giving a period of 2597 days. This will be discussed further in Chapter 5.

Two short-term periodicities were extracted at $46 \pm 1$ days and twice that, at $92 \pm 1$ days, which match the periods found by Pollard et al. (1996) and represents the deep-shallow nature of the characteristic RV Tauri pulsations. The longest period of 22833 days, *i.e.* 62.5 years, comes close to the length of the data set (75 years), and is hence likely to be unreliable.

Since recent UCMJO photometry of U Mon was saturated and unable to be used, older UCMJO $BVRI$ data from the time period JD 2448134 – 2452410 (August 1990 – May 2002) from Pollard et al. (1996) and McSaveney (2003) was used to obtain photometric periods for phasing. Figure 3.6 show the U Mon $V$ photometry periodograms obtained from analysing these data. A complex frequency peak is obvious with frequencies of $0.0222\,\mathrm{d}^{-1}$ and $0.0217\,\mathrm{d}^{-1}$ (periods around 45–46 days) obtained from the Fourier analysis of the older UCMJO photometry.

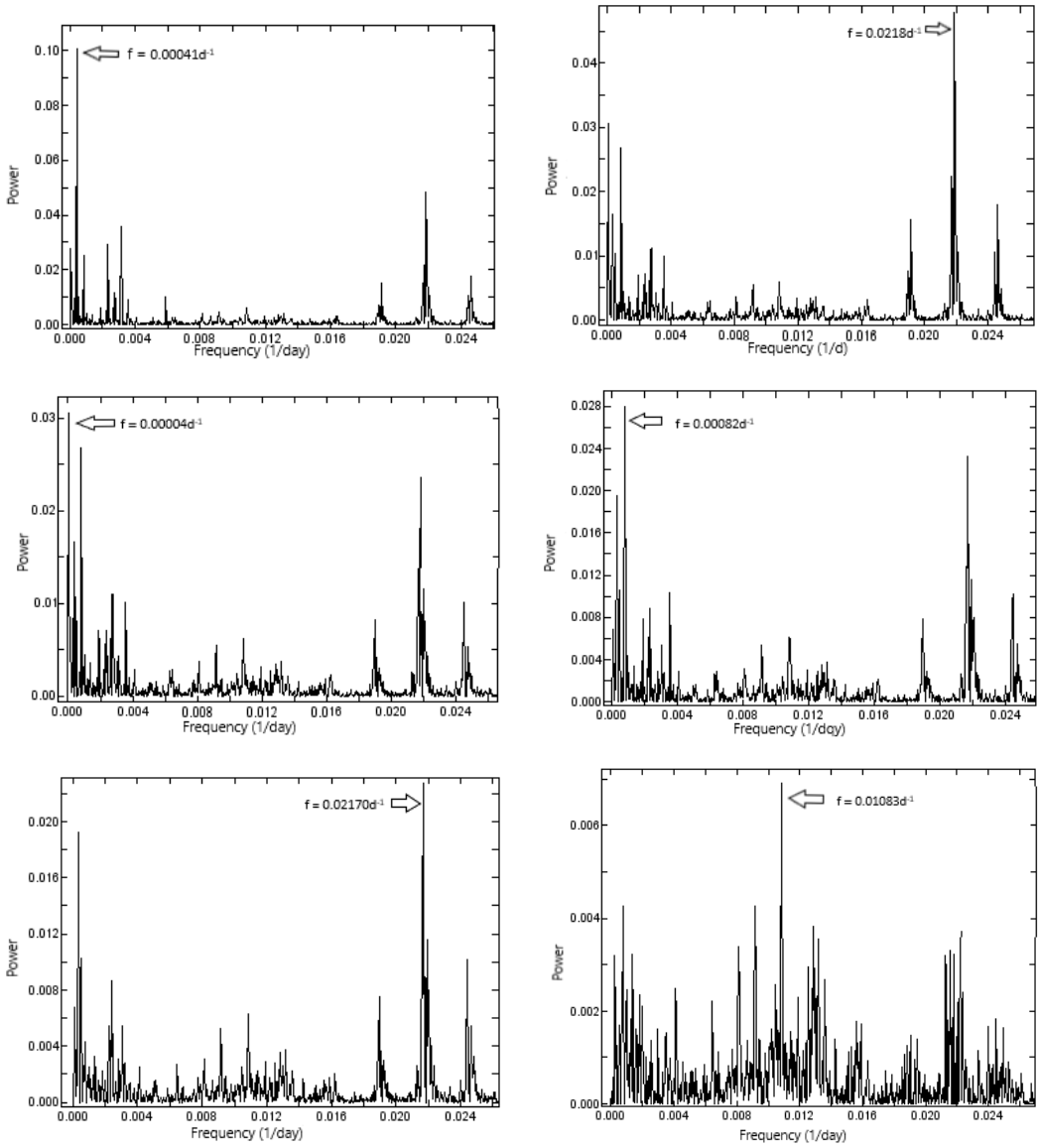


**Figure 3.5:** Consecutive power spectra of the AAVSO long-term visual photometry for U Mon.

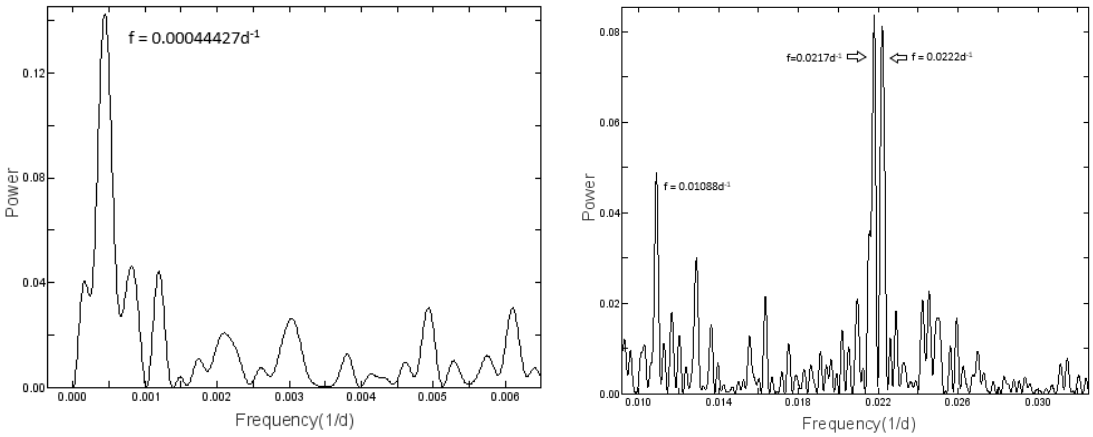


**Figure 3.6:** Consecutive power spectra of older UCMJO U Mon $V$ data from JD 2448134 – 2452410 (August 1990 – May 2002) sourced from Pollard et al. (1996) and McSaveney (2003).

### 3.3.2 AR Pup

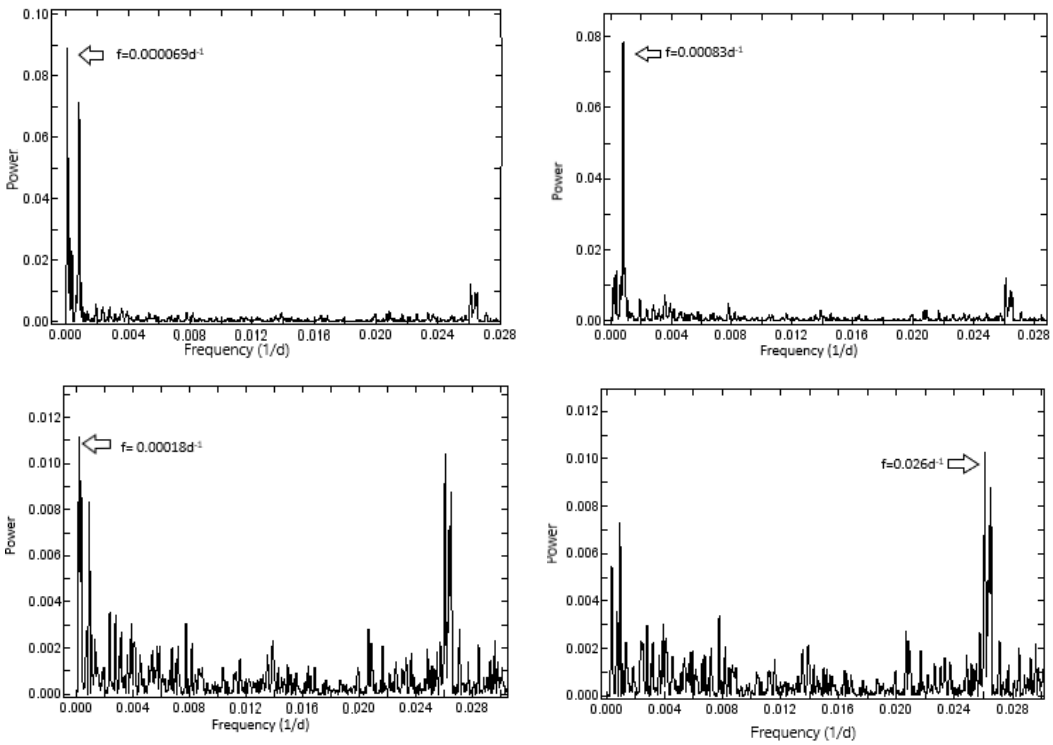


**Figure 3.7:** Consecutive power spectra of the AAVSO long-term visual photometry for AR Pup.

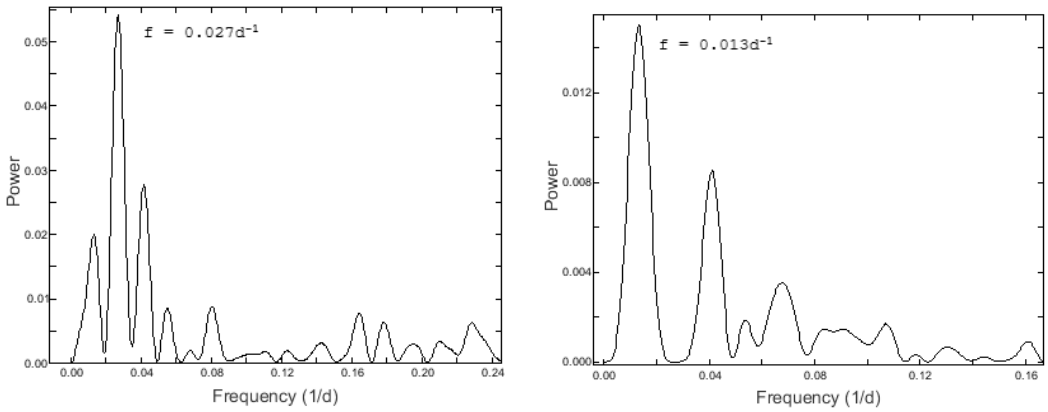


**Figure 3.8:** Consecutive power spectra of the recent $V$ photometry for AR Pup.

Periodograms for AR Pup visual photometry are shown in Figure 3.7. The period of $1205 \pm 5$ days is comparable to the period of 1194 days reported in Percy (2015). The frequency that dominated the first periodogram is at $f = 0.000069$ d$^{-1}$ (14430 days or ∼40 years), and comes close to the length of the data set of 50 years, thus is likely to be unreliable. Another periodicity was found at $5587 \pm 211$ days.

Although this frequency is above the signal-to-noise threshold to be significant, this frequency does not have a mention in the literature.

Among the short-term pulsational periods extracted from the visual photometry of AR Pup was a period of $38.33 \pm 0.96$ days, which was in good agreement with Pollard et al. (1996) who reported a strong peak at 38.91 days in their power spectra. Similar to their result, no strong peak was found at half or twice this period in the visual data. This indicates that the visual light curve does not strongly show the characteristic alternating deep-shallow natures that is usually present in the RV Tauri stars. A period of 75.62 days, which is nearly twice the pulsational period found here, is however reported by Percy (2015).

Fourier analysis of both recent $B$ and $V$ photometry reveal dominant periodicities at 37.05 days with a slight difference in amplitudes and is comparable to results of Percy (2015). Double periods extracted at 74.10 and 76.56 days in $B$ and $V$ photometry respectively are in good agreement with the pulsation period of 74.58 days stated by Percy (2015) from their analysis of AR Pup visual data.

### 3.3.3 IW Car

A frequency of 0.000692 $d^{-1}$ (period $\sim$ 1444 days) dominated the first periodogram (Figure 3.9) of IW Car's visual photometry data. This period (and its amplitude) is in good agreement with the literature values of 1433 days (Percy, 2015) and 1444 days (Pollard et al., 1996).

The sixth frequency extracted was a pulsational frequency at 0.01389 $d^{-1}$ (period of 72 days) is in good agreement with the known pulsational period of 71.96 days (Percy & Kim, 2014).

A peak, possibly due to the Ceraski effect, was present at 366 days ($f$ = 0.00273 $d^{-1}$). This period is also nearly half of the eighth extracted period of 733 days, which agrees with the period of 730 days noted in Pollard et al. (1996).

A $68 \pm 1$ day pulsation period was extracted in recent $V$ data (comparable to 72 days period found in our long term visual data) along with a second period extracted at $34 \pm 1$ days. Both of these periods are in good agreement with the pulsational period of 67.5 days and the shorter period of 36.32 days given by Percy (2015) from their visual data. Three new periods found that do not seem to be mentioned previously in literature were $5295 \pm 44$ days, $1110 \pm 1$ days and $440.7 \pm 0.4$ days. A relatively short pulsational period of $63 \pm 1$ days was found in the corresponding recent $B$ photometry, while the second period of $44 \pm 1$ days was significantly longer than the second period found in the $V$ data.

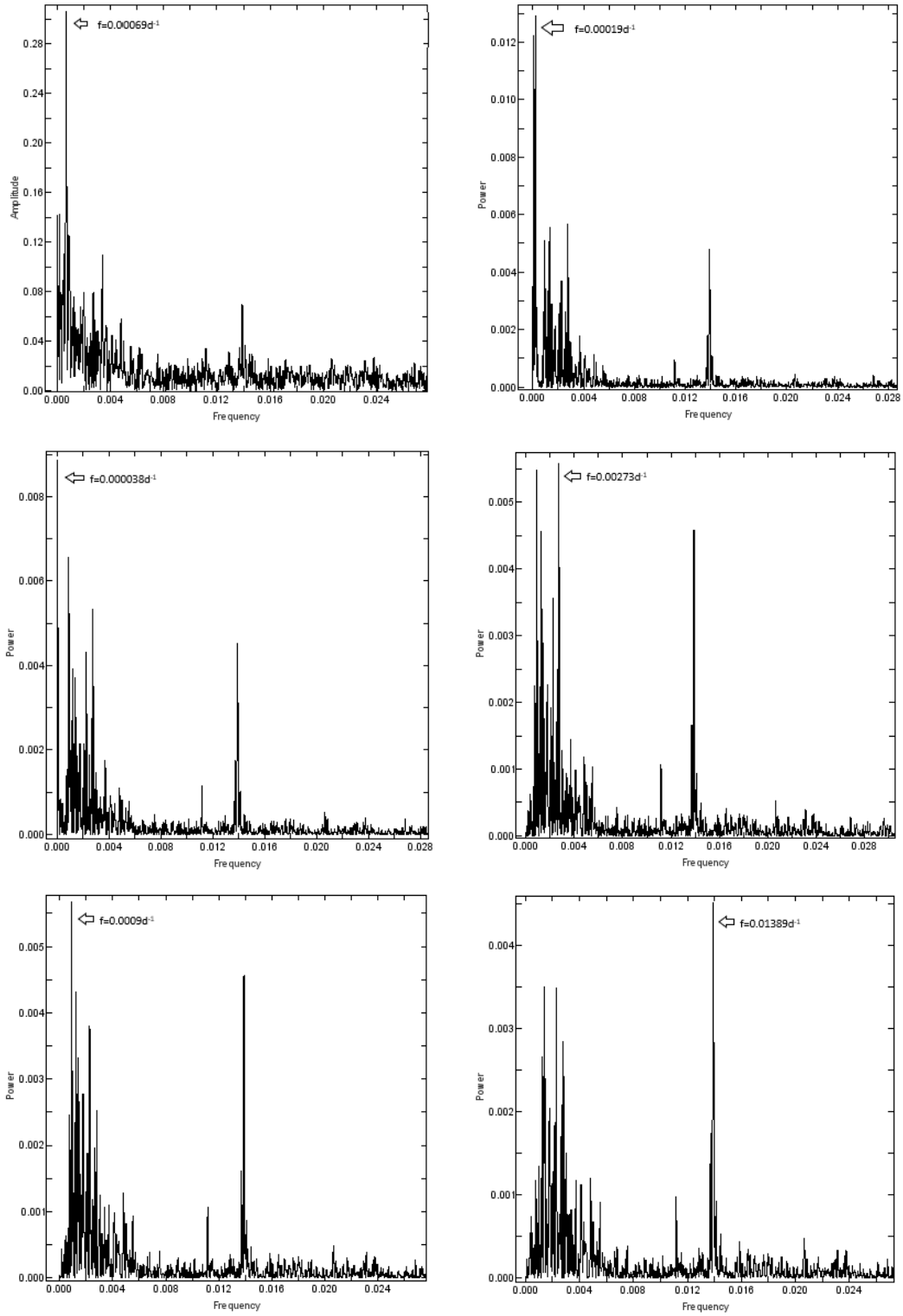


**Figure 3.9:** Consecutive power spectra of the AAVSO long-term visual photometry for IW Car.

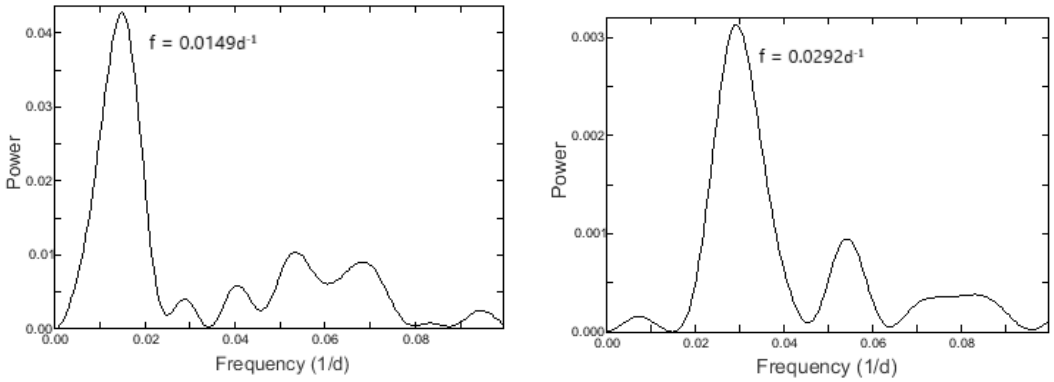


**Figure 3.10:** Consecutive power spectra of the recent $V$ photometry for IW Car.

### 3.3.4 RU Cen

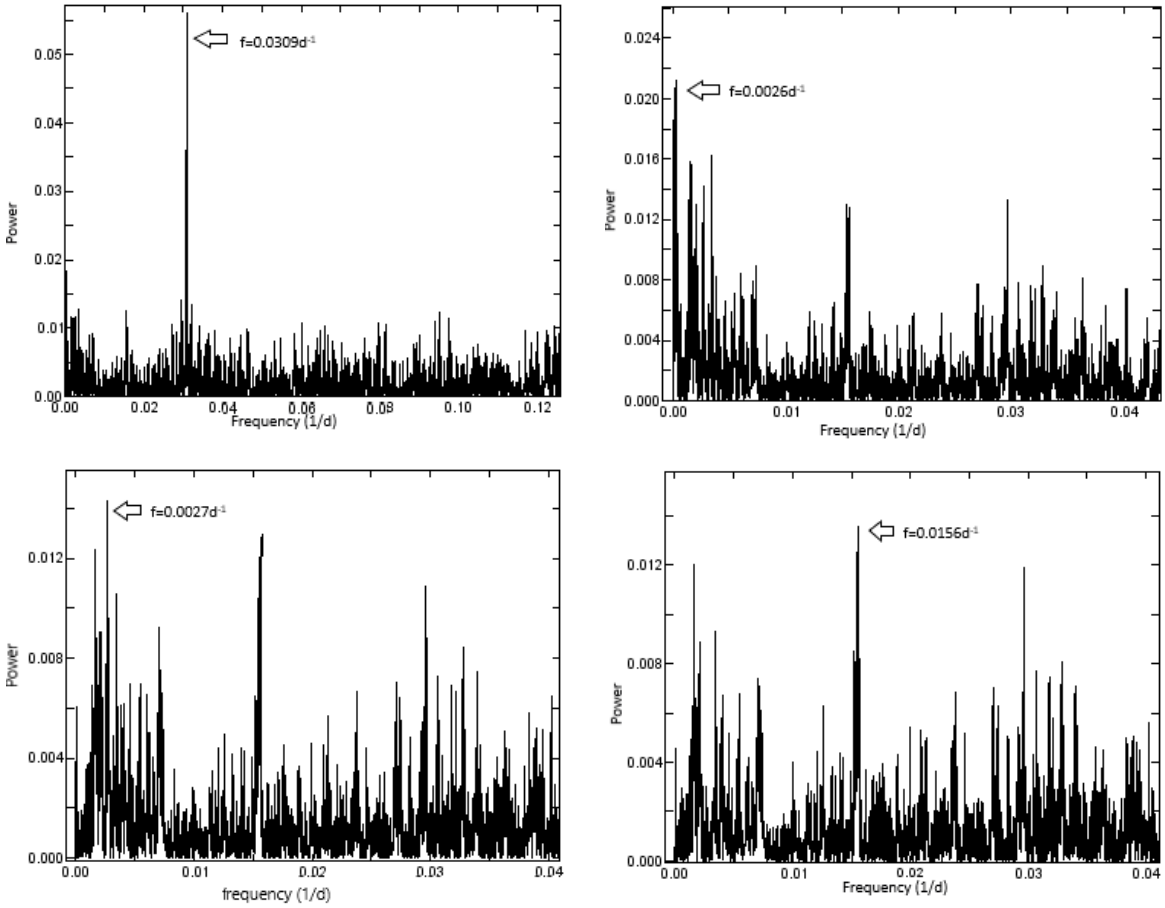


**Figure 3.11:** Consecutive power spectra of the AAVSO long-term visual photometry for RU Cen.

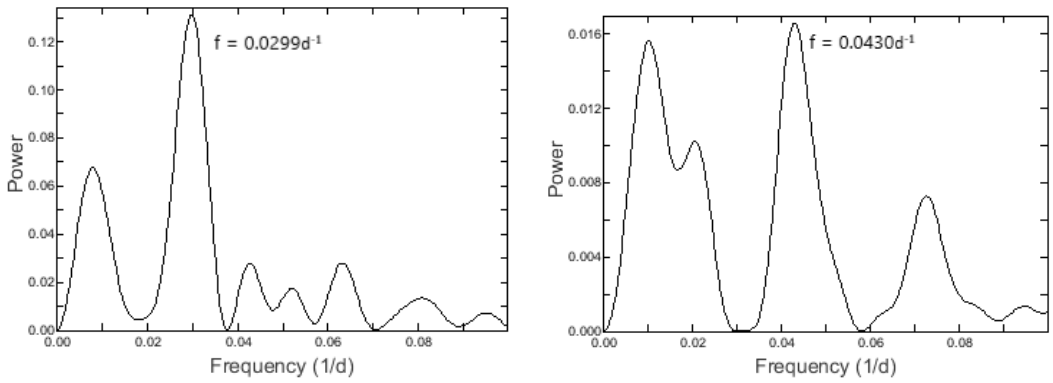


**Figure 3.12:** Consecutive power spectra of the recent $V$ photometry for RU Cen.

AAVSO visual data for RU Cen is relatively sparse and the data set has large gaps. In comparison with other stars, the overall aliasing in the periodograms (see

Figure 3.11 was quite pronounced and the signal-to-noise ratios of the frequencies extracted were relatively low (see Table 3.3). Fourier analysis of RU Cen's visual photometry gives the periodograms shown in Figure 3.11. Harmonic periods of $32.34 \pm 0.02$ days and $64.01 \pm 0.03$ days agree well with the established visual pulsational periods of RU Cen (Percy, 2015). Two longer periods of $372 \pm 1$ days and $3766 \pm 95$ days were also obtained. A binary period of 1489 days reported by Gezer et al. (2015) is not detected in our Fourier spectra.

Due to the lack of sufficient visual data, the available AAVSO $V$ band photometry was also analysed, mostly for the purpose of obtaining a long time baseline least-squares fit of the light curve (see Figure 3.17, top). Similar periods of $32.31 \pm 0.03$ and $62.41 \pm 0.28$ days were obtained and a period of half the pulsational period was extracted at $16.14 \pm 0.14$ days. A lower amplitude period at $31.22 \pm 0.13$ days was also present, which was similar to the first, strongest period found in the data set.

Dominant frequencies in consecutive periodograms of recent $V$ photometry is given in Figure 3.12. Periods of $34.36 \pm 0.12$ days in $B$ and $33.36 \pm 0.06$ days in $V$ were extracted, both of which agree well with the pulsation periods found by Percy (2015) and Pollard et al. (1996).

## 3.4 Least-squares fits

Least-squares fits, explained in Section 2.3, are calculated using `Period04`. A table of the fitting parameters is presented for all of the targets stars in Table 3.4.4. It is again noted that RVb stars typically have a long-term ($\sim 600 - 3000$ d) period superimposed on the short-term ($\sim 30 - 150$ d) pulsations. The uncertainties in parameters are calculated as described in section 2.3.2. The uncertainties in each period is stated and is derived from the standard deviation in each frequency. The mean uncertainties in amplitudes and phases were $\pm 0.05$ and $\pm 0.06$ respectively, derived from the standard deviation outputted by `Period04`.

**Table 3.3:** Least-squares fit results for the AAVSO visual photometry for U Mon, AR Pup, IW Car and RU Cen.

| Star | Frequency ($d^{-1}$) | Period (d) | Amplitude (magnitudes) | Phase | S/N |
|---|---|---|---|---|---|
| U Mon | | | | | |
| $f_1$ | 0.0004105 | 2436±1 | 0.36 | 0.86 | 52.6 |
| $f_2$ | 0.021867 | 45.73±0.06 | 0.22 | 0.42 | 42.7 |
| $f_3$ | 0.0000437 | 22833±155 | 0.20 | 0.24 | 38.6 |
| $f_4$ | 0.000826 | 1210±1 | 0.16 | 0.10 | 32.3 |
| $f_5$ | 0.0217 | 46.1±0.7 | 0.15 | 0.39 | 29.4 |
| $f_6$ | 0.010839 | 92.3±0.8 | 0.08 | 0.67 | 20.9 |
| AR Pup | | | | | |
| $f_1$ | 0.000069 | 14430±102 | 0.32 | 0.54 | 15.7 |
| $f_2$ | 0.000829 | 1205±5 | 0.30 | 0.29 | 17.9 |
| $f_3$ | 0.000179 | 5587±211 | 0.16 | 0.99 | 9.2 |
| $f_4$ | 0.0261 | 38.33±0.96 | 0.10 | 0.05 | 6.1 |
| IW Car | | | | | |
| $f_1$ | 0.000692 | 1444±1 | 0.29 | 0.61 | 32.9 |
| $f_2$ | 0.00019 | 5295±44 | 0.13 | 0.35 | 22.2 |
| $f_3$ | 0.000037 | 26455±1480 | 0.12 | 0.47 | 20.9 |
| $f_4$ | 0.00273 | 366.2±0.7 | 0.07 | 0.52 | 13.2 |
| $f_5$ | 0.00091 | 1110±1 | 0.08 | 0.26 | 13.5 |
| $f_6$ | 0.01389 | 72±2 | 0.07 | 0.52 | 11.9 |
| $f_7$ | 0.00227 | 440.7±0.4 | 0.06 | 0.12 | 10.7 |
| $f_8$ | 0.00136 | 733±1 | 0.07 | 0.46 | 12.8 |
| RU Cen | | | | | |
| $f_1$ | 0.030917 | 32.34±0.02 | 0.25 | 0.99 | 6.5 |
| $f_2$ | 0.0002655 | 3766±95 | 0.16 | 0.22 | 5.3 |
| $f_3$ | 0.002685 | 372 ±1 | 0.12 | 0.52 | 4.1 |
| $f_4$ | 0.015622 | 64.01±0.03 | 0.11 | 0.02 | 3.8 |
| RU Cen $V$ data from AAVSO | | | | | |
| $f_1$ | 0.03094 | 32.32±0.03 | 0.44 | 0.62 | 10.0 |
| $f_2$ | 0.06194 | 16.14±0.04 | 0.12 | 0.12 | 7.0 |
| $f_3$ | 0.032 | 31.25±0.1 | 0.10 | 0.75 | 5.9 |
| $f_4$ | 0.01602 | 62.4±0.3 | 0.09 | 0.55 | 4.9 |

**Table 3.4:** Least-squares fit results for the recent $B$ and $V$ photometry for AR Pup, IW Car and RU Cen.

| Star | Frequency ($d^{-1}$) | Period (d) | Amplitude (magnitudes) | Phase | S/N |
|---|---|---|---|---|---|
| AR Pup $B$ photometric data | | | | | |
| $f_1$ | 0.02699 | 37.05±0.13 | 0.33 | 0.75 | 4.0 |
| $f_2$ | 0.01349 | 74.10±0.23 | 0.22 | 0.43 | 10.1 |
| AR Pup $V$ photometric data | | | | | |
| $f_1$ | 0.02699 | 37.05±0.05 | 0.24 | 0.04 | 4.5 |
| $f_2$ | 0.01309 | 76.37±0.27 | 0.13 | 0.93 | 8.4 |
| IW Car $B$ photometric data | | | | | |
| $f_1$ | 0.01584 | 63.10±0.33 | 0.36 | 0.16 | 5.3 |
| $f_2$ | 0.02278 | 43.89±0.78 | 0.10 | 0.34 | 5.7 |
| IW Car $V$ photometric data | | | | | |
| $f_1$ | 0.01468 | 68.11±0.05 | 0.24 | 0.38 | 5.0 |
| $f_2$ | 0.02927 | 34.16±0.21 | 0.06 | 0.40 | 6.3 |
| RU Cen $B$ photometric data | | | | | |
| $f_1$ | 0.02903 | 34.44±0.12 | 0.46 | 0.77 | 4.1 |
| $f_2$ | 0.01451 | 68.88±0.14 | 0.12 | 0.01 | 2.6 |
| RU Cen $V$ photometric data | | | | | |
| $f_1$ | 0.02997 | 33.36±0.11 | 0.35 | 0.95 | 4.1 |
| $f_2$ | 0.01498 | 66.72±0.07 | 0.12 | 0.69 | 4.4 |

**Table 3.5:** Least-squares fit results for older (1990-2002) UCMJO $V$ photometry for U Mon, where the photometric data are sourced from Pollard et al. (1996) and McSaveney (2003).

| Star | Frequency ($d^{-1}$) | Period (d) | Amplitude (magnitudes) | Phase | S/N |
|---|---|---|---|---|---|
| U Mon UCMJO $V$ photometric data from 1990–2002. | | | | | |
| $f_1$ | 0.0004643 | 2153.55±0.33 | 0.35 | 0.23 | 4.0 |
| $f_2$ | 0.021778 | 45.91±0.21 | 0.29 | 0.09 | 10.1 |
| $f_3$ | 0.022277 | 44.88±0.59 | 0.24 | 0.37 | 4.0 |
| $f_4$ | 0.010887 | 91.85±0.32 | 0.27 | 0.70 | 10.1 |

### 3.4.1 U Mon

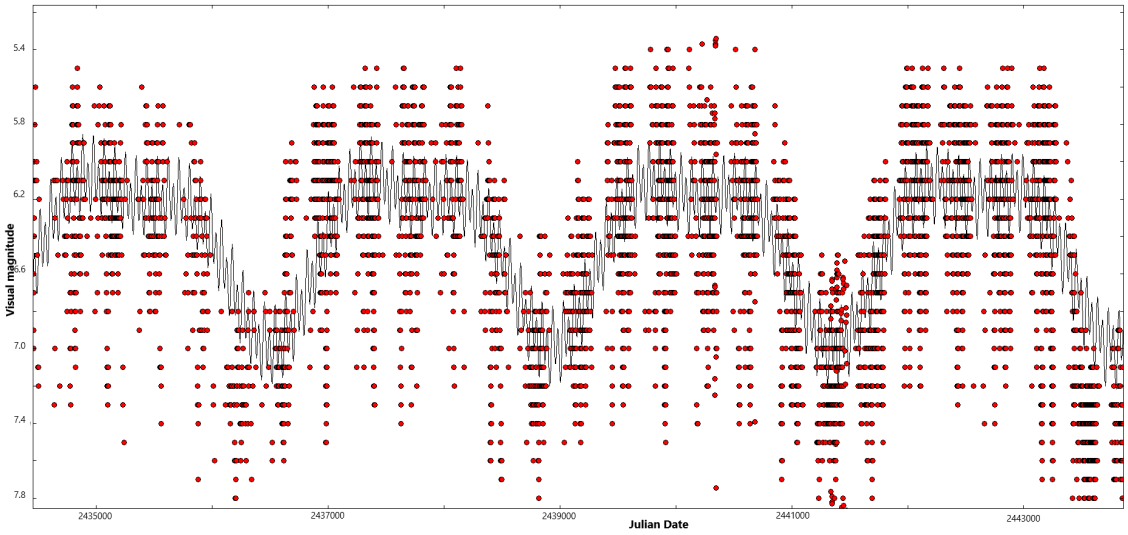


**Figure 3.13:** The visual photometric data for U Mon is plotted together with the near-harmonic fit ($\sim P + 2P$) of the periods found; with periods of 2436, 1210, 92 and 46 days included in the fit.

Figure 3.13 shows the nearly harmonic fit ($\sim P + 2P$) of the periods found with periods of 2436, 1210, 92 and 46 days included in the fit. The values of 46±1 days, $92.25 \pm 0.78$ days and $2436 \pm 0.03$ days are in reasonable agreement with the values stated by Percy (2015) of 45.73 and 91.32 days from $V$ data and 2427 days from visual AAVSO data of a few years shorter time span than that used in this work. The periods of 46 days and 92 days also match with the periodicities found by Pollard et al. (1996).

### 3.4.2 AR Pup

The least-squares fit of AR Pup visual photometry is shown in Figure 3.15 (top). Three periods of 14427 d, 1205 d and 5585 d are used to fit the light curve, out of which the period of $1205 \pm 5$ days is comparable with the period of 1194 days stated in Percy (2015) and with the period of 1389 days found by Pollard et al. (1996) in their UCMJO photometric survey. The period of 14427 days (∼39 years) is comparable to the length of the data set (∼50 years) and is mainly intended to approximately fit the shape of the long-term variation seen in the light curve.

The two pulsational periods extracted from the analysis of both recent $B$ and $V$ photometry were found to be a harmonic fit that traced the data well, as shown in Figure 3.15.

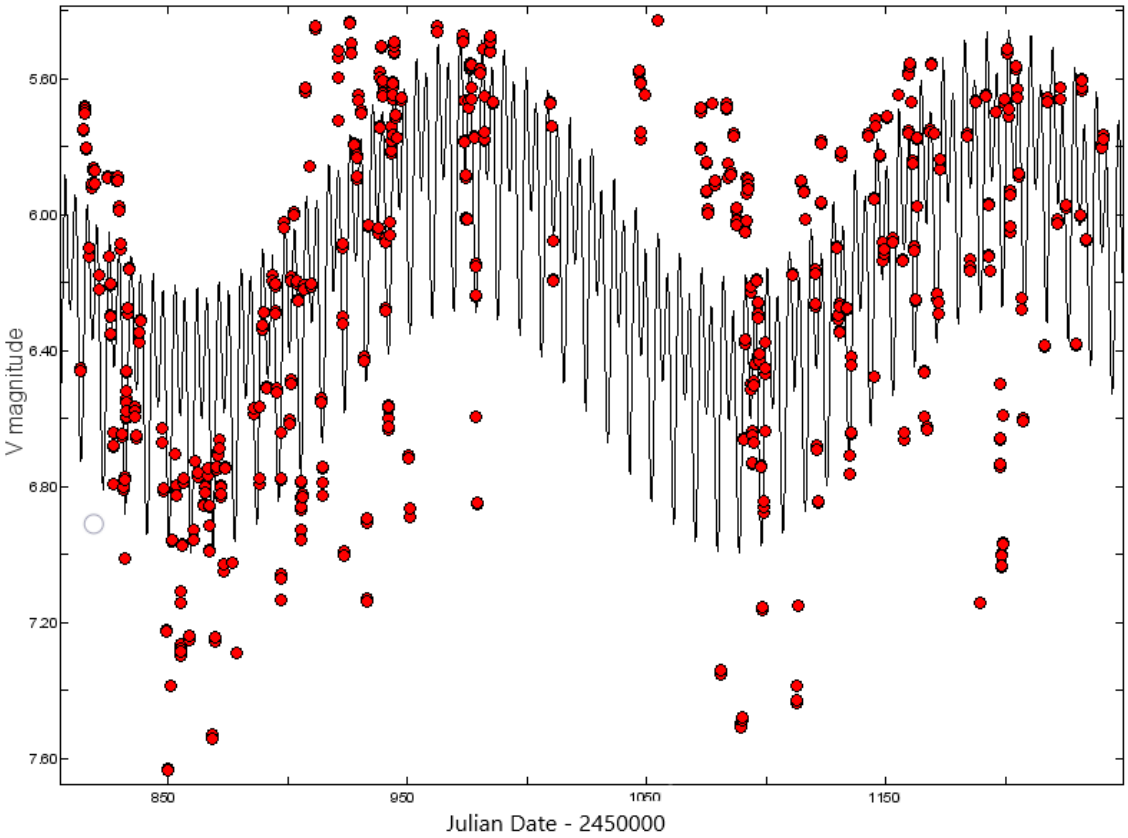


**Figure 3.14:** U Mon $V$ curve reproduced using data from Pollard et al. (1996) and McSaveney (2003), fitted with periods found of 2154, 46 and 92 days.

### 3.4.3 IW Car

IW Car's least-squares fits are shown in Figure 3.16. Three periods of 72, 1444 and the very long-term period of 26442 days are selected for the fit. The first two frequencies are the pulsational and the long-term variation periods comparable to the results of Percy & Kim (2014) and Percy (2015) respectively. The very long period of 26442 days is longer than the length of the data set and again, as done for AR Pup, is only intended to fit the overall trend of the long term variation seen in the light curve. Both recent $B$ and $V$ light curves were fitted with the two frequencies found in each of their Fourier analyses.

### 3.4.4 RU Cen

As noted previously, the data for RU Cen was sparse and with large gaps, especially the visual data, hence $V$ AAVSO data was used for least-squares fitting. Fourier spectra of the visual data revealed dominant periodicities, least-squares fit results of which are given in Table 3.4.4. Figure 3.17 shows the fit for the $V$ AAVSO data of RU Cen. All the four extracted periodicities given in Table are used for the fit as it

gives the best representation of the overall $V$ light curve. Figure 3.17 (middle and bottom panel) shows the harmonic fits with periods of 34.44 days and 68.88 days for recent $B$ data, and 33.36 days and 66.72 days for recent $V$ data.

### 3.4.5 Summary of Fourier fitting results

The Fourier fitting results show a strong near 2:1 ratio between fundamental mode and the first overtone for the pulsational period in all the RV Tauri stars studied in this work. This resonance hypothesis has received support by Takeuti & Petersen (1983), Tuchman et al. (1993) and Fokin (1994) for characterizing the alternating behaviour in RV Tauri star light curves. Harmonic periods are used for fitting where possible to show this behaviour.

It can be seen that the amplitude of the long-term multi-frequency fits is smaller than expected, and doesn't coincide completely with the data points, especially for U Mon. This is often due to the variable nature of the amplitude of the long-term period, which is unable to be modelled well with a single sinusoidal fit. The obvious fact that all the long-term amplitudes vary over time may give clues as to it underlying physical cause being cyclical rather than strictly periodic. It is confirmed that fits that included more frequencies, gave better fits to the light curve, as expected.

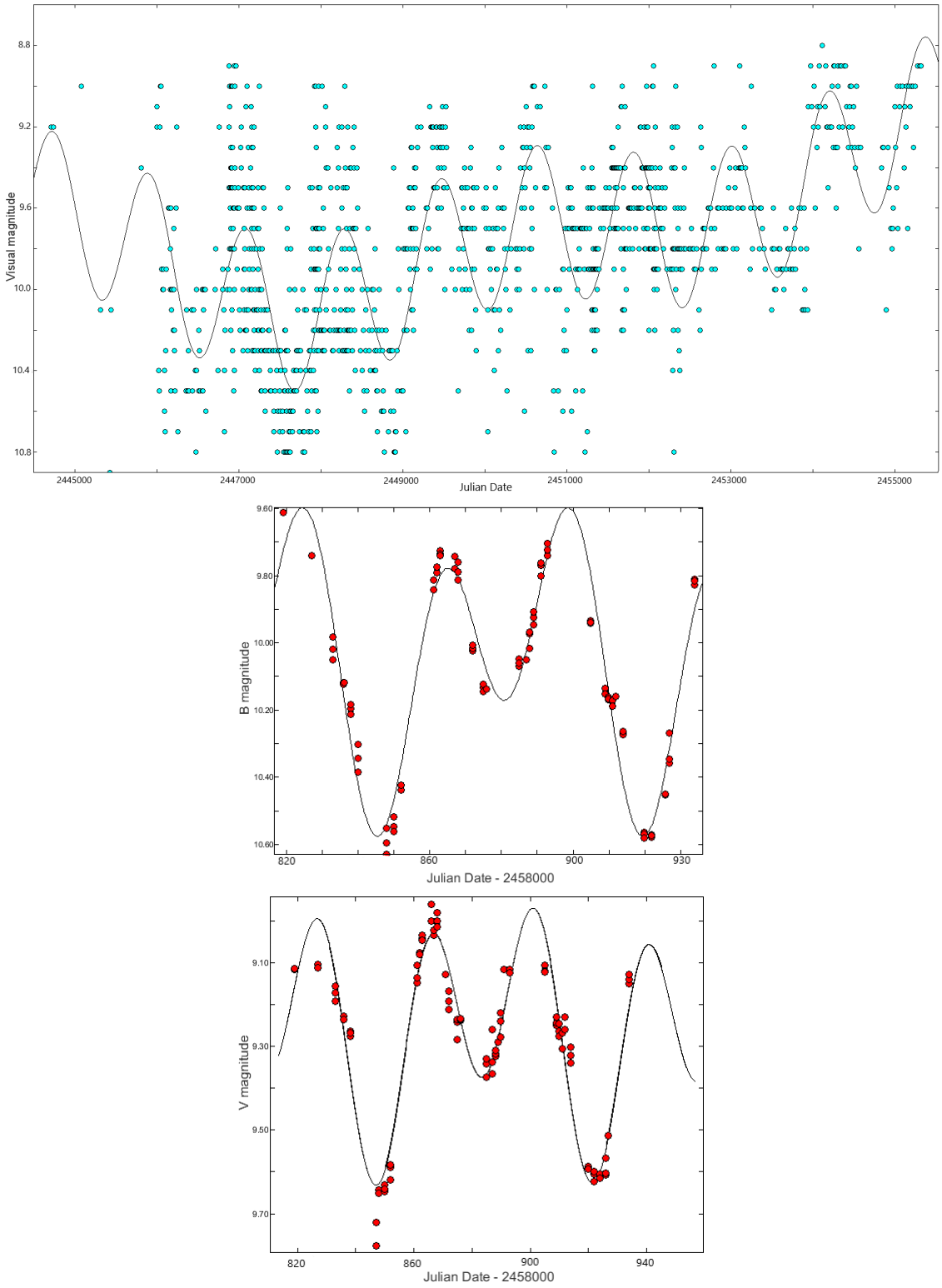


**Figure 3.15:** (Top) The long-term visual data for AR Pup is plotted with the least-squares fit using three long-term periods of 14427, 1205 and 5585 days. The recent $B$ (middle) and $V$ (bottom) photometric data is plotted with the least-squares harmonic fit of two short-term pulsational periods of 37 and 75 days, and, 37 and 76 days, respectively.

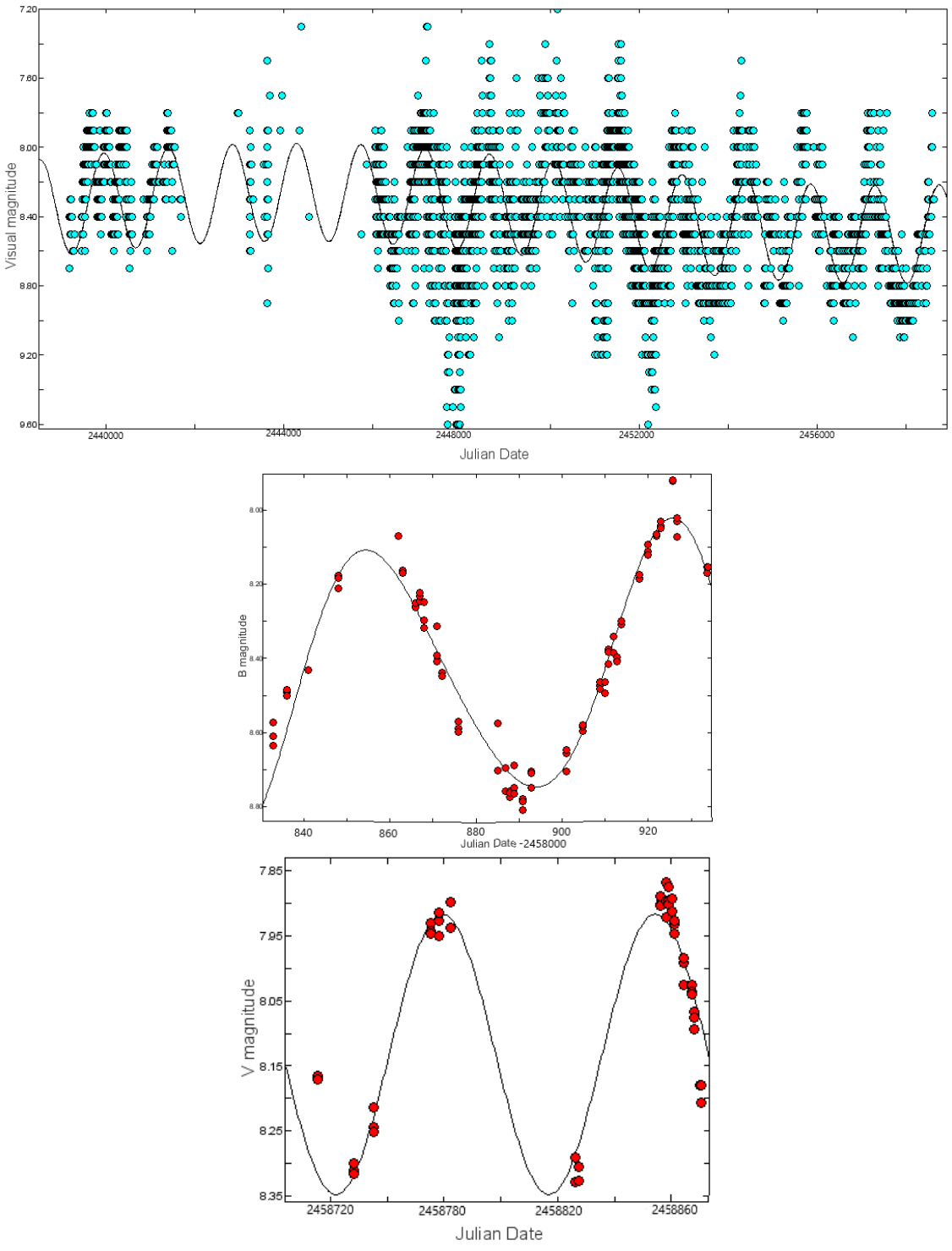


**Figure 3.16:** (Top) The least-squares fit to the AAVSO visual data for IW Car, with three periods of 72, 1444 and 26442 days. The least-squares fits of recent $B$ (middle) and $V$ (bottom) data with periods of 63.1 and 43.89 days, and, 68.11 and 34.16 days, respectively.

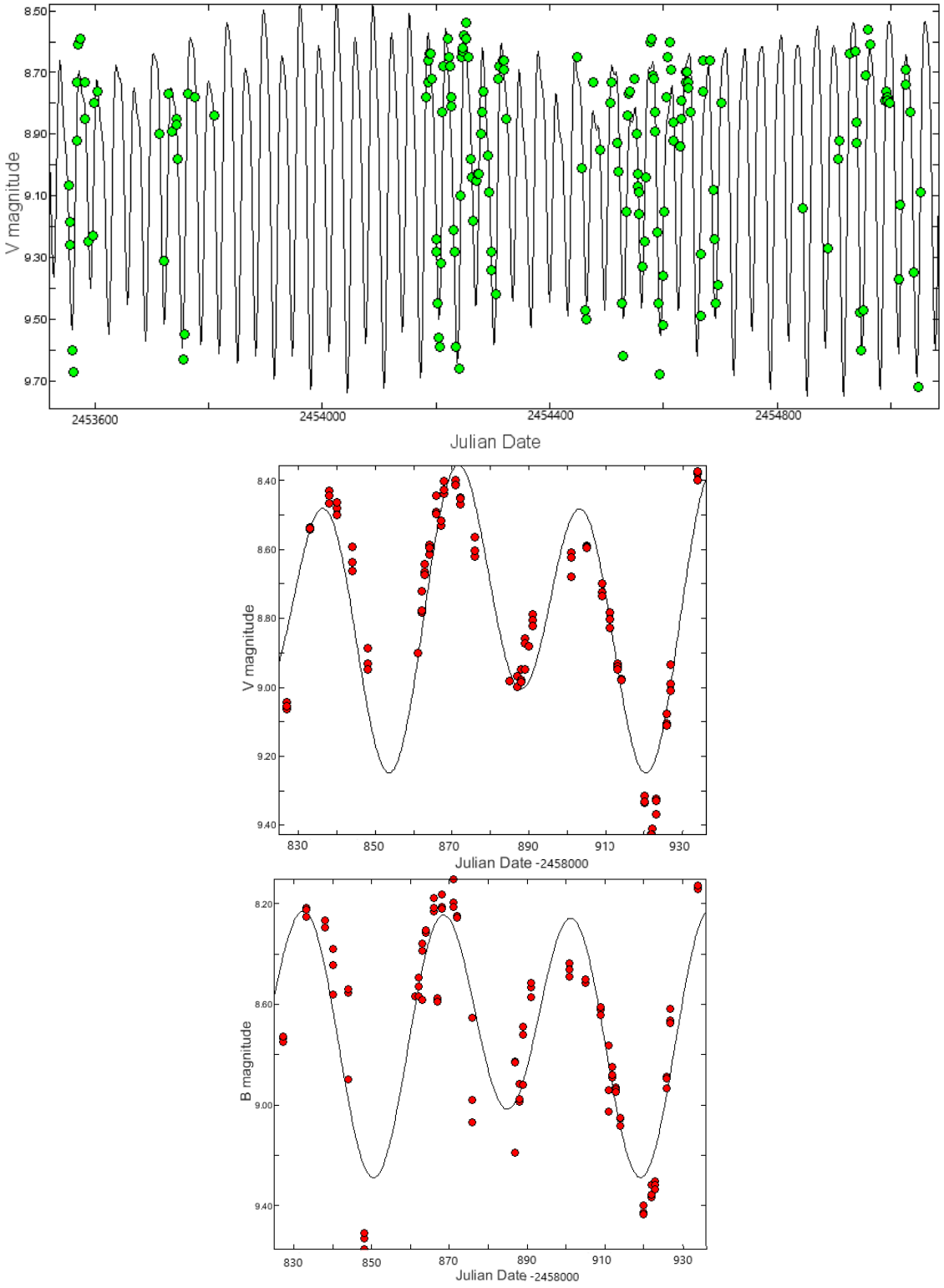


**Figure 3.17:** (Top) The least-squares fit of AAVSO $V$ data for RU Cen using all four extracted periods of 32, 16, 31 and 62 days. The harmonic least-squares fits of recent $B$ (middle) and $V$ (bottom) data for RU Cen with two periods of 32 days and the double period of 64 days extracted from the Fourier analysis.

## 3.5 Wavelet analysis results

This section contains the results of WWZ period and amplitude variability determinations using AAVSO's `VSTAR` time-series analysis package. Analysis is carried out for U Mon and IW Car as they had sufficient data for wavelet analysis. IW Car has two large seasonal gaps in the data that must be considered while inspecting the wavelet plots. In a similar way to Percy & Khatu (2013), default values for the decay constant ($c = 0.001$) and time division ($\Delta t = 50$ days) were used in the analysis. The results are only sensitive to decay constant $c$. Using values higher than 0.001 for $c$ showed more scatter in the amplitude-time curves.

The graph of period versus time shows the strength of the period at a particular time. The color scheme given in the graphs in this section are related to the value of WWZ as a measure of strength; red being the strongest and pink being the weakest. White areas in the graph are indicative of unavailability of data at the time. As Percy & Kim (2014) note, amplitude (the strength of the variation), is similar to semi-amplitude, which is the coefficient of the fitted sine curve found using the date compensated discrete Fourier transform (DCDFT) in `VSTAR`, the value of which was found to be similar to Fourier analysis done through `Period04`. The graphs which show amplitude variations is a graph of semi-amplitude versus time.

### 3.5.1 U Mon

Figure 3.18 shows the variations in pulsational periods (top panel) of 46 and 92 days and long-term period (bottom panel) of 2436 days in long-term AAVSO visual data for U Mon. Periods of 45.73±0.06, 46.08±0.66 and 92.25±0.98 found in this thesis are in good agreement with the mean periods found by McSaveney et al. (2002). They analysed visual estimates of U Mon from 1961–2000 through the AAVSO WWZ wavelet analysis program and state mean periods of 46±2 and 91±2 days for first half of their data set, and 46±1 and 92±1 days for the second half. They also note the pulsational period of 92 days is less often detectable in the first half of their data set, which agrees with our result seen in the WWZ plot of short-term pulsations (see Figure 3.18 top panel). The period of 92 days is more transient compared to the 46-day period and is seen more strongly in the later half of the observations. The strongest presence (in red) seen of the long-term period is between 2400–2500 days and is strongest during JD 2437000–2446500 (see Figure 3.18 bottom panel).

Figure 3.19 shows that the variation in the period and amplitude of the pulsation mode of 46 days is more rapid compared to that of the long-term period of 2436 days. However, the variations appear reasonable random and no long-term increase or decrease of the short-term period is obvious. The graph of the long-term period

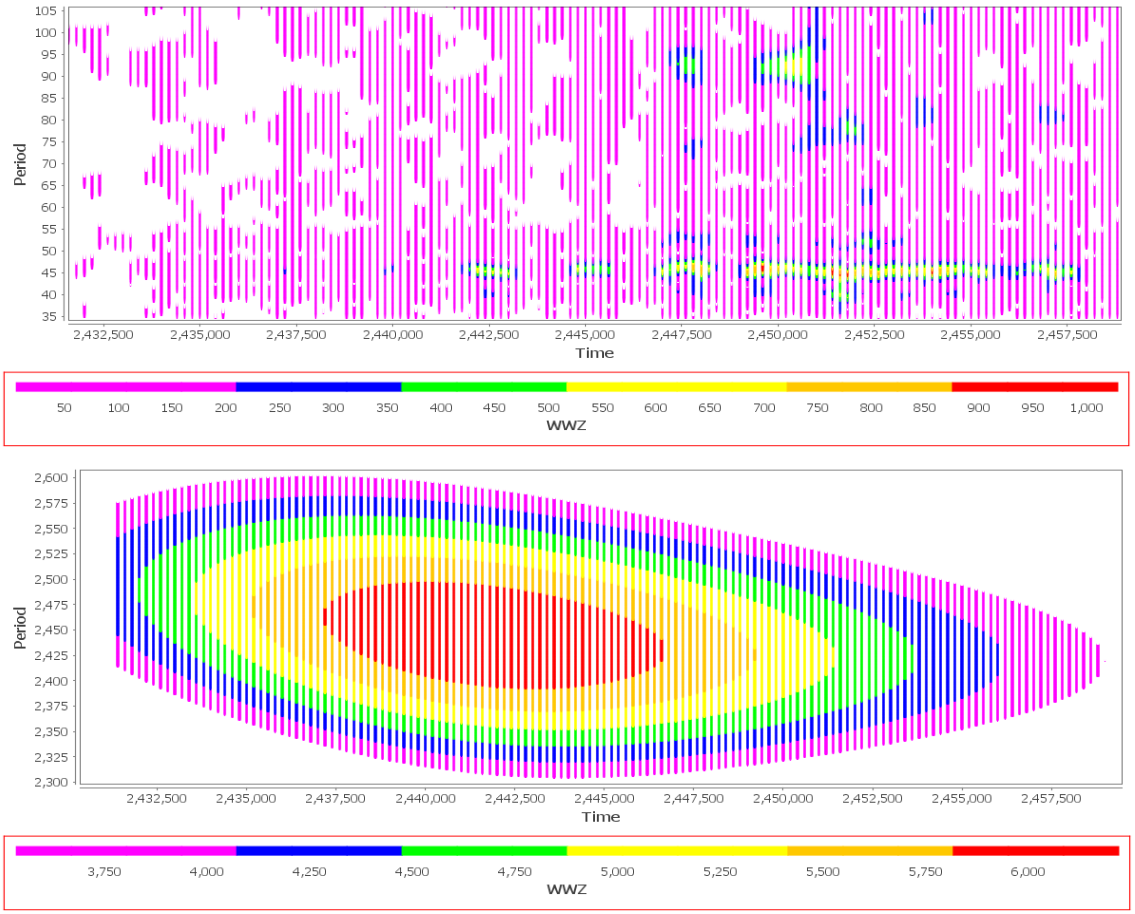


**Figure 3.18:** The result the WWZ wavelet analysis of the long-term AAVSO visual data for U Mon. (Top) Pulsational variability in the mean periods of 46 and 92 days. (Bottom) Long-term variability in the mean period of 2436 days.

shows that the amplitude of the long-term variation decreases, and period also decreases with time. There is a relatively quick initial change in mean period value, which slows down and almost flattens towards the end. Throughout the same time span, the amplitude decreases significantly, with the semi-amplitude changing from 0.425 to 0.275 magnitudes, in a relatively smooth manner.

### 3.5.2 IW Car

For IW Car, the changing short-term pulsation of 67.5 days and 71.96 days mentioned in the literature can be seen in the WWZ plot (Figure 3.20 top panel). These pulsations are detected most strongly before JD 2440000 and are neither distinguishable nor detectable from ∼JD 2442150 to the end of the observations. The long-term period variation around the mean period of 1444 days is strongly detected between ∼JD 2448750–2458000 (Figure 3.20 bottom panel).

The long-term variability and amplitude of the mean period of 1444 days of

**Figure 3.19:** (Top) The variations in the U Mon pulsational period of 46 days (left) and its semi-amplitude (right) using the WWZ wavelet analysis. (Bottom) The variation in the long-term mean period of 2436 days in U Mon (left) and its semi-amplitude (right).

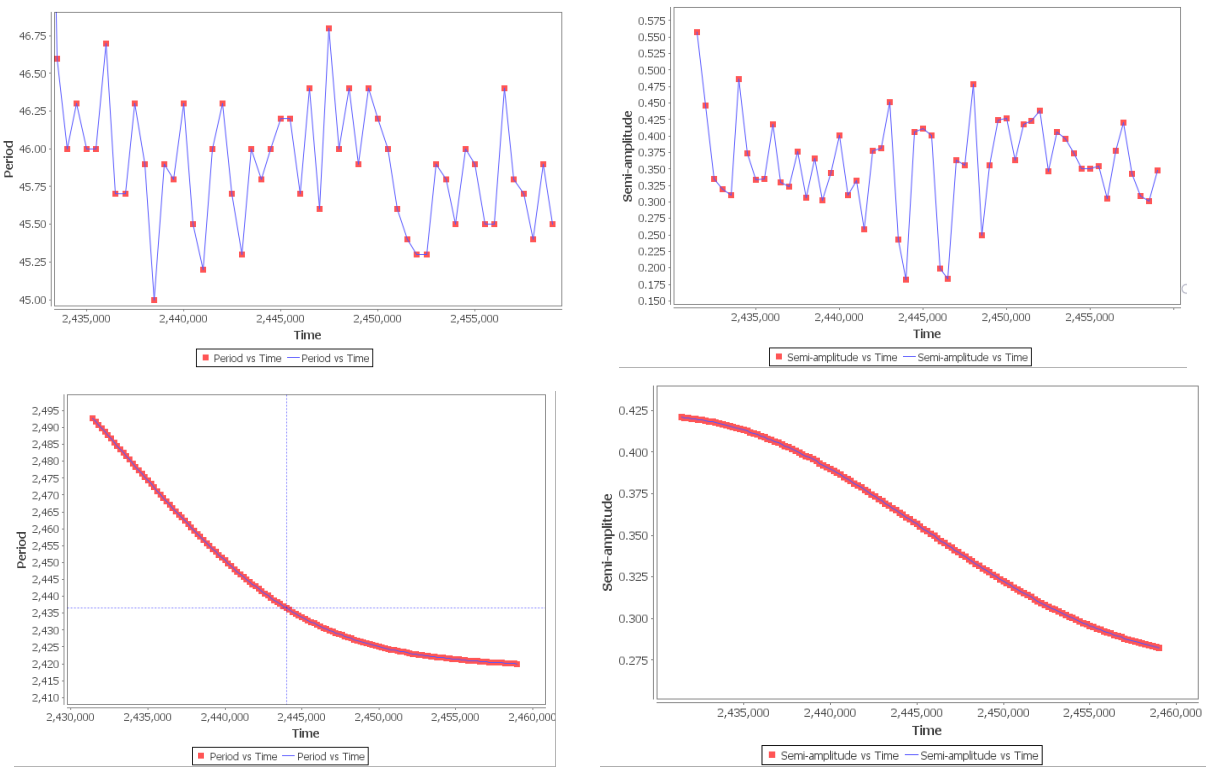


IW Car is seen in the top panels of Figure 3.21. The period and its amplitude seems to be the most stable between JD 2450000–2458000.

The changing short-term pulsation is only detected from the start of the time span of observations until around JD 2442150, as shown in Figure 3.21 (bottom left panel). It is seen to start off at around 67 days, maintaining stability for around 500 days before rapidly changing to ∼72.5 days until it is not detectable. This could be either due to high period - low temporal resolution of the wavelet analysis, or due to the highly unstable pulsational signal (as indicated from the variability in Figure 3.20: top) intrinsic to the star; rapid period fluctuations every few cycles. The latter possibility could turn out to be reasonable as Pollard et al. (1996) notes "very irregular light variations in both period and amplitude". The range of pulsation periods found in this work and mentioned in literature may support this view.

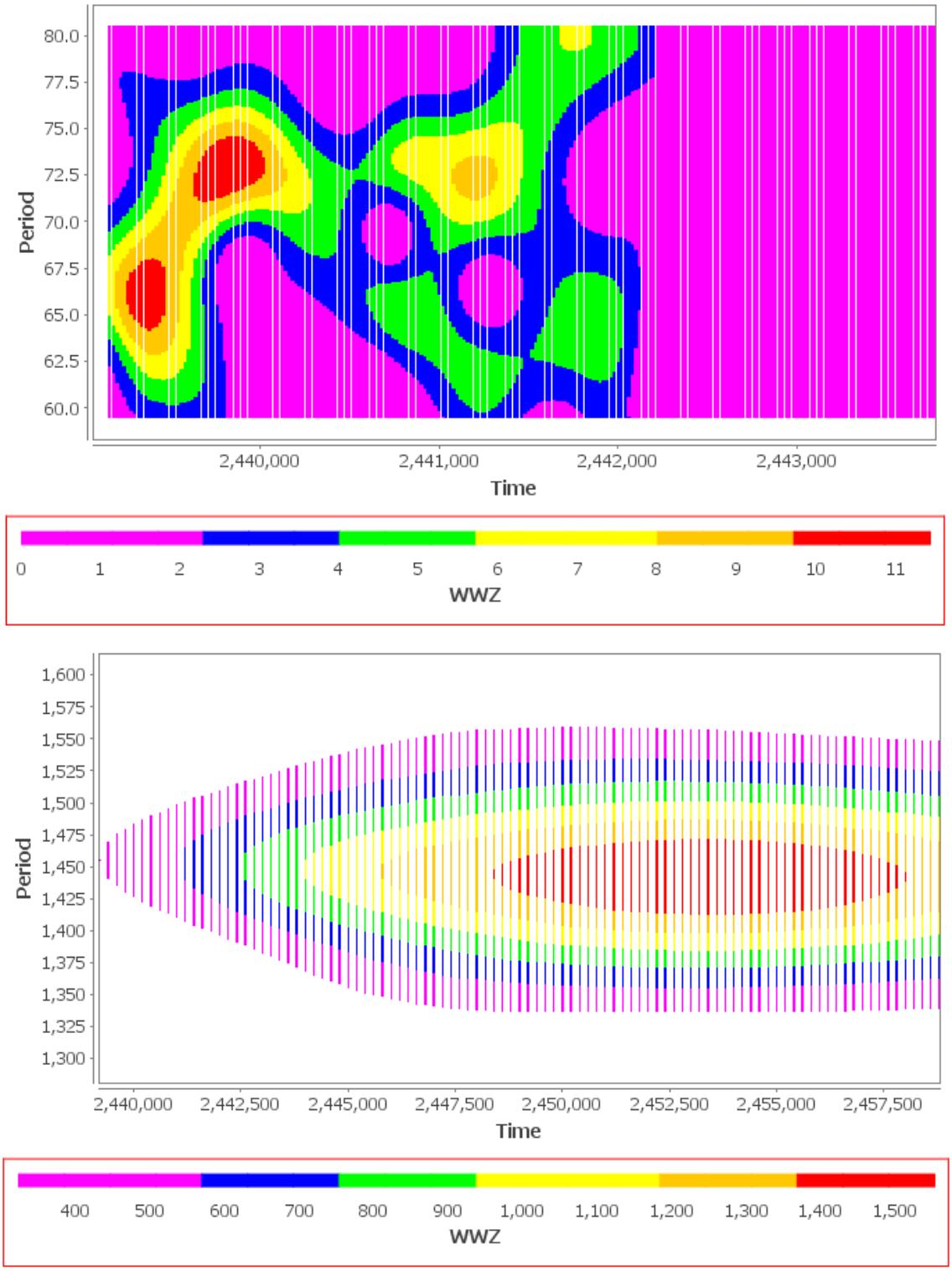


**Figure 3.20:** The WWZ wavelet analysis results for IW Car. (Top) Pulsational variability in the mean period of 71 days. (Bottom) Long-term variability in the mean period of 1444 days.

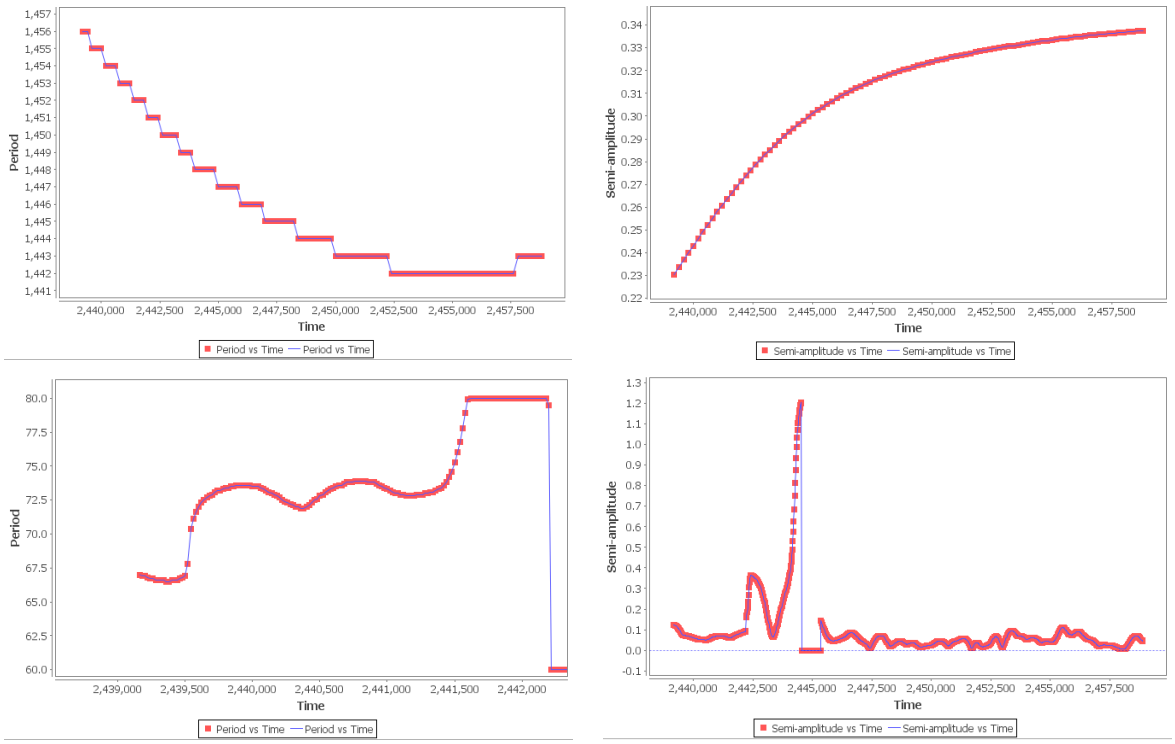


**Figure 3.21:** (Top) The WWZ wavelet analysis results for IW Car for the long-term period of 1444 days (left) and its semi-amplitude (right). (Bottom) The variation in the mean pulsational period of 72 days (left) and its semi-amplitude (right).

## 3.6 Summary

For the brightest target star in our sample, U Mon, the long-period variation of $2435.53 \pm 0.03$ days is seen in the visual data which confirms its RVb classification. Short-term pulsations at $46.1 \pm 0.7$ days and $92.3 \pm 0.8$ days were extracted out of which the former was more strongly detected in the wavelet analysis. All of these periods were used in obtaining a least squares fit which was a good representation of the visual light curve.

For AR Pup, the visual photometry revealed long term variation of $1205 \pm 5$ days confirming its RVb classification. A longer period of $5585 \pm 211$ was present with a relatively low signal-to-noise ratio. Recent photometry revealed the characteristic RV Tauri alternating deep-shallow nature of the light curve. A harmonic fit of the likely fundamental and first overtone pulsation periods extracted at $74.10 \pm 0.13$ and $37.05 \pm 0.32$ days was a good representation of the $B$ light curve.

The RV Tauri characteristic deep-shallow behavior in not seen in IW Car. A long-term variation is evident however. A long period of $1444 \pm 1$ days confirms its RVb classification. A longer period of $5295 \pm 44$ days was also detected but does not appear to be reported previously in literature and is of low significance. Recent UCMJO $V$ photometry revealed likely fundamental and first overtone pulsational periods of $68.11 \pm 0.76$ days and $34.16 \pm 0.12$ days. The former period is subject to high variability as seen in wavelet analysis.

Previously classified as an RVa-type RV Tauri star (Pollard et al., 1996), newer literature suggests RU Cen might be actually be an RVb-type star. Percy (2015) state a "long secondary period" of 561 days. This frequency was not detected in our analysis. A binary period of 1489 days stated by Gezer et al. (2015) is also not detected in our Fourier analysis. A period of $3766 \pm 95$ days was found, but perhaps due to aliasing from seasonal gaps and sparsity of the data, this period was detected at low signal-to-noise ratio, so may not be real. Employing a harmonic fit by fixing the second period as double of the first proved to be a good representation of the recent UCMJO $B$ and $V$ photometry for this star.

All target RV Tauri stars indicated a fundamental and first overtone radial pulsations. Fourier analysis of each star revealed a second pulsational period that was close to twice the fundamental period of the short term pulsation, resulting in the characteristic deep-shallow nature of the RV Tauri star pulsations to a greater or lesser degree, depending on the star.

In the filtered photometry, the $B$ light curves have larger amplitudes than the $V$ light curve for all target stars, and generally slightly lead in phase, although the periods are consistent. The $(B-V)$ colour curves are typically slightly out-of-phase with the light curves, displaying the bluest colours at the phase when the light curve is rising from a minimum to a maximum and shock wave phenomena are seen in the spectra (see Chapter 5).

# Chapter 4

# Spectroscopy

This chapter summarizes the spectroscopic data acquisition and reduction done for this thesis. All the observations were obtained with the High Efficiency and Resolution Canterbury University Large Échelle Spectrograph (HERCULES) on the 1.0-metre McLellan telescope. Although a few spectra were acquired of all targets in this thesis, the priority for a detailed analysis was focused solely on the brightest "RVb" type RV Tauri star U Mon. With a $V$ magnitude of 5.82[1], U Mon was the brightest target allowing high signal-to-noise spectra to be obtained. It also had the best visibility during the time period available for observation from November 2019 to April 2020. Its relatively long pulsation period of 92 days meant that few pulsation cycles could be sampled, but the cycles observed would have a reasonably good phase coverage. This phase coverage is important in order to carry out the aim of this project, namely to characterise the pulsational behaviour, including the radial velocity variations and the shock-related features visible in its spectra.

## 4.1 The 1.0-metre McLellan telescope

The 1.0-metre McLellan telescope (Fig. 4.1) is a Dall-Kirkham reflecting telescope which had its first light in March of 1986[2]. The optics were polished by Industrial Research Ltd. while the mechanical and electronic work was done by University of Canterbury's (UC's) Physics Department workshop staff in Christchurch.[2] The telescope has 2 configurations of Cassegrain foci, at f/7.7 and f/13.5, of which the latter is used for spectroscopy with HERCULES. The dome is coupled with telescope and both automatically move when tracking a star. Other available UCMJO instruments, such as the Fingerlakes CCD, are generally used for imaging with the wider field of view offered by the f/7.7 configuration[2]

[1] http://simbad.u-strasbg.fr

[2] https://www.canterbury.ac.nz/science/field-and-research-stations/mount-john-observatory/facilities/

**Figure 4.1:** Top: The 1.0-metre McLellan telescope building and dome at UCMJO. Bottom: The 1.0-metre McLellan telescope with fibre-feed unit attached.

## 4.2 HERCULES

HERCULES is the fibre-fed spectrograph on the 1.0 m McLellan telescope that was used to acquire the spectra for RV Tauri stars, including the primary target, U Mon. Designed and built at UC, it has been in operation at UCMJO since April 2001. HERCULES is installed inside a large vacuum tank in a thermally-isolated and insulated room, and has no moving parts, to achieve high wavelength stability (with a precision better than $10\,\mathrm{m\,s^{-1}}$ in radial velocity under optimal conditions) (Hearnshaw et al., 2002). It uses an échelle diffraction grating to achieve the high spectral resolution required for a detailed analysis of spectral line profiles in stellar spectra. HERCULES receives star light from the telescope through an optical fibre. The fibre-feed unit is attached at the Cassegrain focus of the telescope and there are three optical fibres available at site which allows different resolving powers. The fibre used for the purpose of this work has a core diameter of $100\,\mu$m with a resolving power $R = 41000$, which is optimised for the typical seeing conditions at Mt John. The Spectral Instruments 600 series CCD system has a back-illuminated Fairchild 486 CCD chip comprising of 4096 by 4096 square pixels, $15\,\mu$m in size.[3]. The large CCD size allows the full free spectral range to be observed without moving the CCD. The typical useful wavelength range for HERCULES spectra is between about 380 nm and 880 nm. (Hearnshaw et al., 2002).

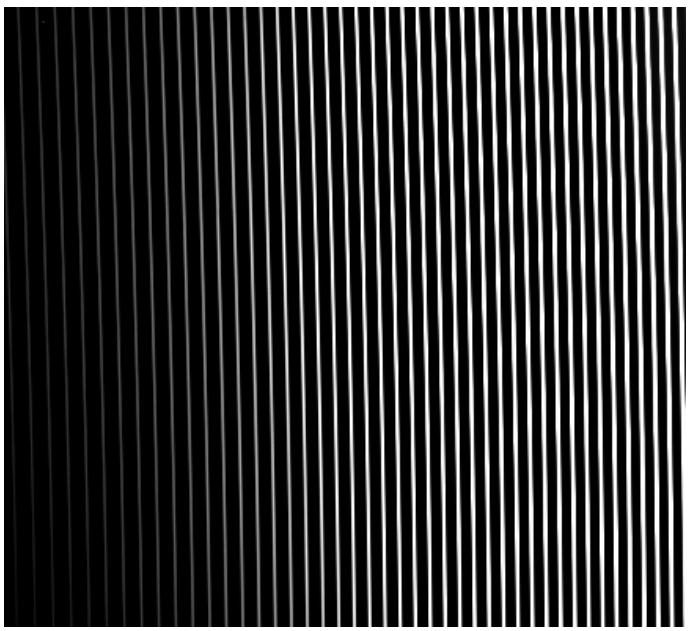

**Figure 4.2:** A region of a flat-field (white light) calibration image, showing that the spectrum is relatively featureless with no absorption or emission lines.

[3]https://www.canterbury.ac.nz/science/field-and-research-stations/mount-john-observatory/facilities/

**Figure 4.3:** A region of a thorium-argon arc calibration image showing the emission lines of thorium and argon at specific and known wavelengths.

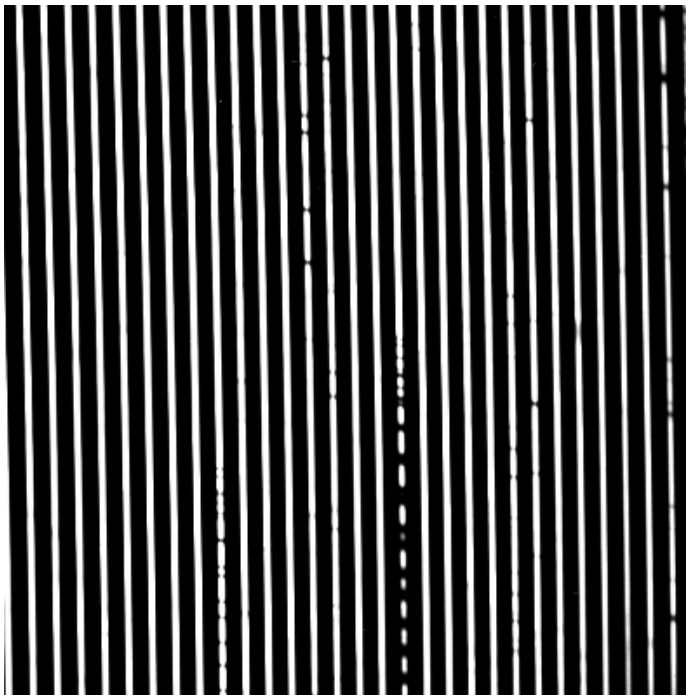

**Figure 4.4:** A region of a U Mon spectral image showing the spectral orders containing stellar and telluric absorption lines.

## 4.3 Observations

Several different types of calibration images were acquired in order to successfully reduce the HERCULES spectra.

Ten 5-second flat-field (or white light) images using an incandescent tungsten lamp were taken at the start of each observing night. The resulting spectrum is featureless (no emission or absorption lines), hence used to account for any pixel to pixel response inconsistencies and variations on the CCD. The combined and median-clipped spectrum of ten flat-fields for each night is also used for tracing the positions of shaped of the spectral orders and removing the effects of dust, and correcting for the blaze function response of the spectrograph.

Five-second exposure thorium-argon arc lamp spectra were used to calibrate the U Mon stellar spectra. A thorium-argon lamp is used to pass its light through the spectrograph and standard observing procedure is to obtain an arc spectrum before and after each target star observation, or every 60 minutes if observing the same target. Since each thorium-argon arc spectrum has thousands of emission lines of which the wavelength values are established, it can be used to compare and determine and model the variation in the values of the wavelengths across each spectral order and across orders in the stellar spectra.

The exposure time to obtain a good stellar spectrum of U Mon was about 15 minutes (900 s) depending on weather and seeing conditions. At least two spectra of U Mon were obtained each observing night. Although the tracking was done automatically with the autoguiding camera, any initial offset had to be manually adjusted and the target identified before beginning the exposure.

An observing log was kept and comments were made of any consequential events during and between each observation.

## 4.4 Reduction and processing

The reduction of the observed raw CCD data to usable reduced spectra is achieved via a MATLAB code produced by Dr Duncan Wright (Wright et al., 2007), which has been further developed as *MEGARA* by Dr Emily Brunsden (Brunsden, 2013).

The reduction begins with the stellar images being flat-fielded using the images of white light taken at the start of each observation night. All the flat-field images are summed and median clipped to produce a master flat-field image for each night or each run. Pixel-to-pixel variations in sensitivity for the CCD are found in this way and stellar spectral images can be corrected. These flat-field images are also used to determine the location and width of the spectral orders.

Automated statistical comparisons are done for all three types of spectral images:

flat fields, thorium-argon arcs and stellar images. The user is notified to inspect the quality of a spectral images in comparison to the template spectra for over-saturation, under-saturation, bad sampling and other common problems.

The bluer spectral orders with small wavelengths are typically very faint and therefore too noisy to be useful, hence data from the first 500 rows of pixels where these bluer orders exists in this region of CCD, is removed from all the images. This "blue chop" value can be adjusted if the user wishes; for instance if very blue stars are being observed and the blue orders are important. Using the well defined line positions and established wavelengths of the thorium-argon spectra, the spectra were wavelength calibrated and separated into spectral orders. This is achieved by locating the emission lines on each image by a calibration matrix containing pixel coordinates of the known thorium-argon spectral lines. The user is notified if fewer than minimum (less than 800) emission lines are located. If so, the next nearest thorium-argon image can be used as a template to perform a new calibration. A fourth-order polynomial is fitted to the located spectral line positions to find a pixel to wavelength solution. This specifies the wavelength range for each spectral order.

The wavelength solution from the thorium-argon images and information from flat-field images are applied to stellar spectral images to calculate wavelengths. A cosmic ray removal process is also carried out to correct for the occasional cosmic ray that is detected in any of the spectral images. A total of 92 stellar spectra of U Mon were reduced (see Table 5.1 and each reduced spectrum was saved as a MATLAB readable .mat file ready to be processed further.

The reduced stellar spectra are then wavelength-shifted (or barycentric corrected) to correct for the Earth's motion around the solar system barycentre. The value of this shift was obtained through using the barycentric correction routine from the HERCULES Reduction Software Package (HRSP) version 7.0, created by Dr Jovan Skuljan (Skuljan, 2004), and using the star's position, the mid-time of observation, and observatory position on the Earth (latitude, longitude and altitude).

In the next step, the stellar spectra were continuum-fitted. First a synthetic spectrum was created using a Fortran program called SynSpec, using parameters similar to the target stars, *i.e.* a similar effective temperature ($T_{\rm eff}$), surface gravity ($\log g$) and $v\sin i$. [4] By comparing the synthetic spectrum with the observed spectrum, spectral regions corresponding to the continuum level can be identified and used to determine the continuum level throughout each order of each stellar spectrum. By doing a continuum-fit, each spectral order is fitted with a variable-order polynomial depending on the variations in the overall intensity in the spectral order.

[4] $v\sin i$ is the projected rotational velocity of the star where $v$ is the equatorial rotation velocity and $i$ is the angle of inclination to the line of sight of the observer. In general, only $v\sin i$ (not $v$) of a star can be determined spectroscopically Gaige (1993).

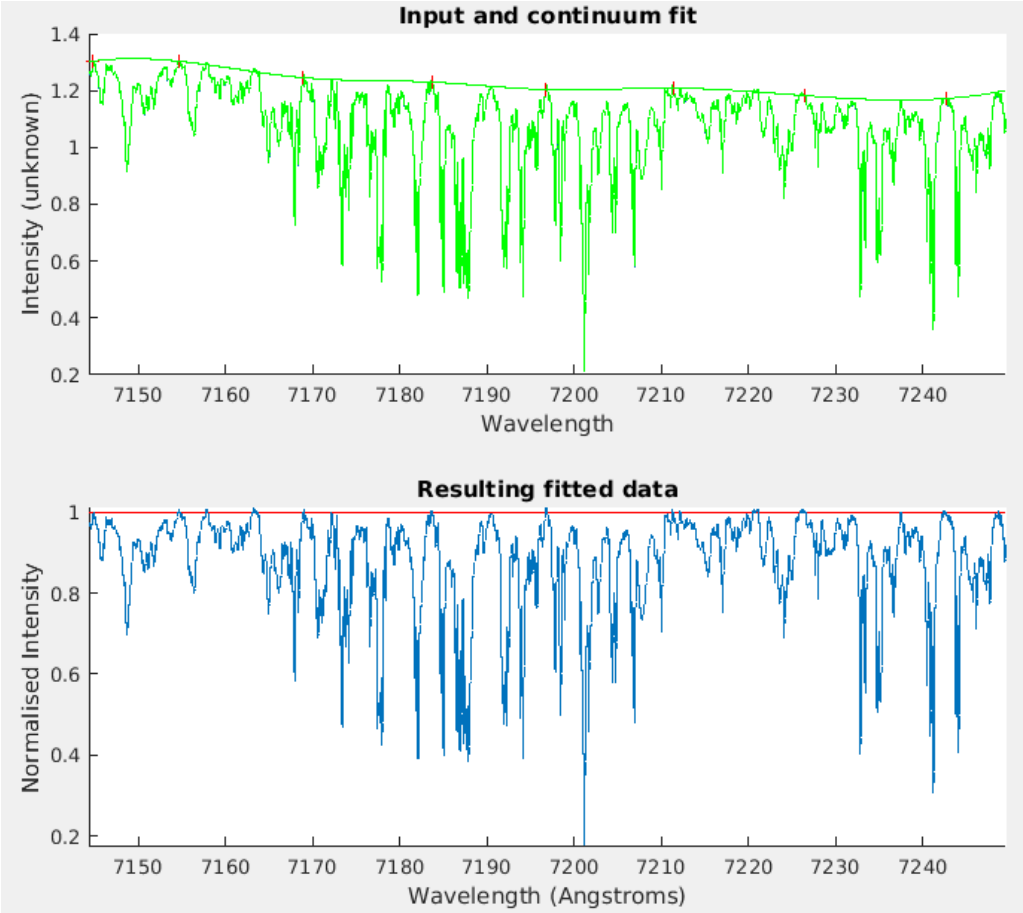


**Figure 4.5:** Continuum fitting of a spectral order of U Mon. The graph on top shows the variations in the overall intensity fro this spectral order, while the bottom graph shows the continuum-fitted normalized spectral order.

The stellar orders are then divided by the fitted continuum to obtain the normalized spectral orders. Spectral orders are then merged together to produce a continuous and normalized stellar spectrum. Figure 4.5 shows an example of continuum fitting of one order of a U Mon spectrum. These normalized stellar spectra can then be plotted as time sequences to identify spectral lines and measure the shifts in wavelength due to radial pulsational velocities. These spectra can also be plotted versus pulsational phase to examine the spectral line emission and splitting that occurs at certain pulsational phases when strong shock waves propagate through the stellar photospheric layers where the spectral lines are forming.

A final step in the data processing was the creation of a cross-correlated line profile for each stellar spectrum. Each stellar spectrum is converted from wavelength space to radial velocity space. Next, the spectral regions with strong telluric and hydrogen lines are removed from the spectrum by masking these wavelength region. Telluric lines are a result of absorption by atoms and molecules in the Earth's atmosphere and would reproduce the barycentric motion if cross-correlated. Hydrogen

lines are known to shift and split due to the Stark effect, while some broad hydrogen lines may blend in and distort other lines, and strongly affect the cross correlation profiles, hence they are generally unsuitable for the cross-correlation process.

Next, the stellar spectrum is cross-correlated with a synthetic template of similar $T_{\rm eff}$, log$g$ and $v$sin$i$ as the target star. The number of spectral lines to be included in the cross correlation process can be changed by increasing or decreasing the minimum strength (in equivalent width in mÅ) of the spectral lines to be included. The output is a mean cross-correlated line profile for each stellar spectrum. This cross-correlated line profile is of very high signal to noise, as it results from the cross correlation of many thousands of metallic lines in the spectrum with those in the template. Since many thousands of lines are used, the cross-correlation profile represents the average behaviour of all photospheric lines in the stellar spectrum weighted by their relative strengths.

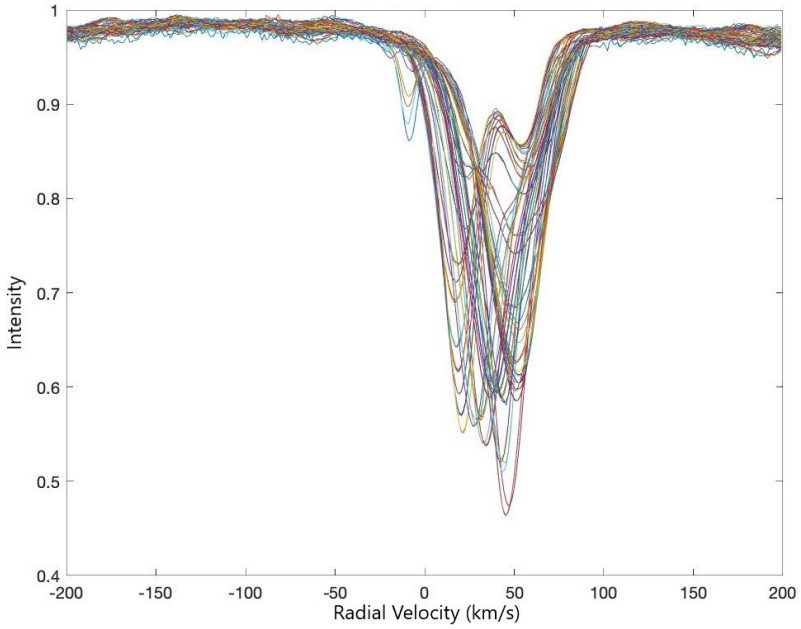


**Figure 4.6:** Spectral line profiles in U Mon spectra obtained from cross-correlating the observed spectra with the synthetic template. The radial velocity range of the lines is roughly $0 - 60\,\mathrm{km\,s^{-1}}$.

The mean radial velocity motion of the stellar atmosphere can be obtained from the high signal-to noise cross correlation profiles as shown in Figures4.6 and 4.7. However, individual photospheric lines can show dramatically different behaviour from the mean, since they are formed at specific depths in the stellar atmosphere (governed by a number of factors including their species, ionization and excitation potential, energy level, and oscillator strength, log$gf$. In general, spectral lines from the same species and excitation state and with similar excitation potential and

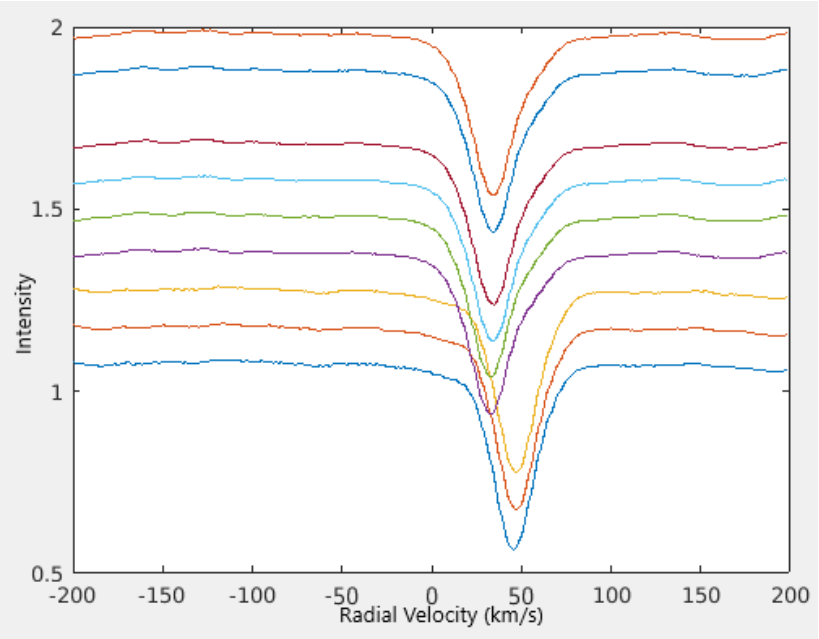


**Figure 4.7:** A sample of a few of the individual cross correlated line profiles for U Mon, each with an offset of 0.5 in intensity. The profiles are stacked with time increasing from bottom to top, and clearly show the shift in the radial velocity of the profile with time.

oscillator strength (log *gf*) are expected to behave in a very similar manner when exposed to velocities, velocity gradients or shock waves in the stellar photospheric layers (Gray, 2005).

In a similar manner to Pollard et al. (1997), the radial velocities of selected spectral lines were measured using the reduced and wavelength-calibrated, but *not* cross-correlated, spectra. The chosen spectral lines was measured, spectrum by spectrum, by fitting a Gaussian curve to the spectral line and determining its position, width and depth (see Figure 4.8).

To convert from the wavelength axis of the spectra to velocity axis, the Doppler equation was used, where the radial velocity, $V_r$ is

$$v_r = \frac{\lambda - \lambda_r}{\lambda_r}.c \tag{4.1}$$

where $\lambda$ is the observed wavelength for that particular atomic transition (from the moving object), $\lambda_r$ is the rest wavelength for this transition and c is the speed of light. If the target star is moving away from the observer, then the observed wavelength will increase in magnitude (red-shift), giving a positive radial velocity. If the target star is moving towards the observer, the observed wavelength will decrease in magnitude (blue-shift) and giving a negative radial velocity.

The individual spectral lines were Gaussian-fitted to extract the position (with the shift directly related to radial velocity of the star), depth and width. The radial

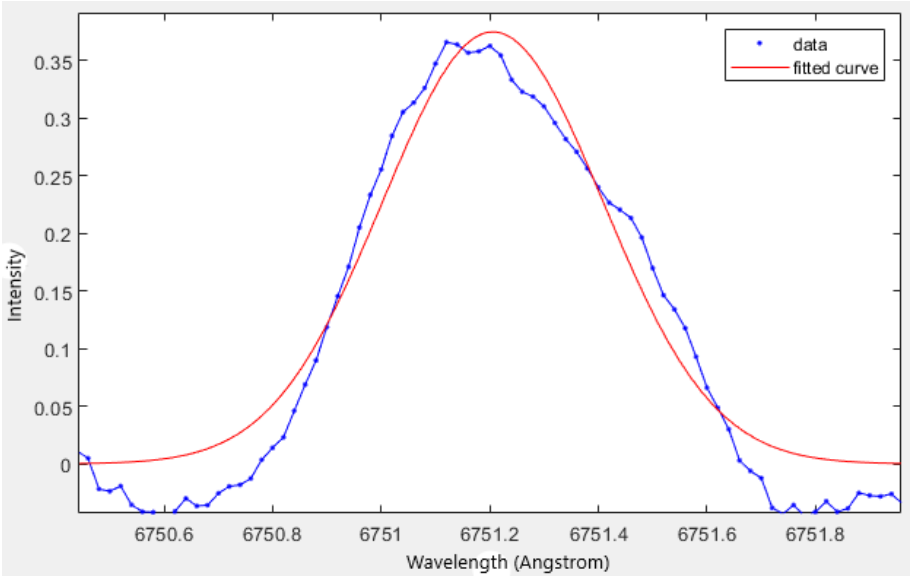


**Figure 4.8:** The Gaussian fitting process for one of the neutral iron (Fe I) line profiles in U Mon. The blue line is the inverted stellar absorption line profile and red line is the best-fit Gaussian to the line profile.

velocities can then be plotted against the time or the phase of the pulsation cycle. to examine the effects of the stellar pulsations and shock waves. The results of this analysis are presented in the next chapter.

# Chapter 5

# Spectroscopy Results

This chapter presents a summary of the results and analysis of the spectroscopic data of the target RV Tauri star U Mon. All the observations were made using the HERCULES spectrograph instrument on the 1.0 m McLellan telescope at the University of Canterbury Mount John Observatory (UCMJO). A total of 92 spectra were obtained between November 2019 and March 2020, spanning about 1.5 cycles of the 92-day pulsation period. A summary of the spectroscopic observations obtained for this thesis is given in Table 5.1. All measured radial velocities are given in Table B.1-B.2.

**Table 5.1:** Times and number of spectra obtained of the bright RV Tauri star U Mon using the HERCULES spectrograph on the 1.0-m McLellan telescope at the UC Mt John Observatory. The typical exposure time was 900s (15 minutes) for each stellar spectrum.

| Date | JD range | number of spectra | observer |
|---|---|---|---|
| 02-03 Nov 2019 | JD 2458790 - 2458791 | 4 | Kunal Bhardwaj and Fraser Gunn |
| 08-15 Dec 2019 | JD 2458826 - 2458833 | 9 | Fraser Gunn |
| 06-16 Jan 2020 | JD 2458855 - 2458865 | 25 | Kunal Bhardwaj and Fraser Gunn |
| 06-16 Feb 2020 | JD 2458886 - 2458896 | 27 | Ed Budding |
| 05-15 Mar 2020 | JD 2458914 - 2458924 | 27 | Fraser Gunn |

Spectra, light and radial velocity curves are phased using a pulsation period of 91.85 days obtained from the Fourier analysis of the UCMJO photometry from JD 2448134 – 2452410 (August 1990 – May 2002) from Pollard et al. (1997) and McSaveney (2003). The epoch used for phasing the spectra and the radial velocity curves for this work is JD 2458790.056. The epoch used for phasing the light and

colour curves is JD 2450808.043.

Figures are generally inclusive of all the 92 spectra, sequentially stacked with a consistent offset in intensity, zoomed in on specific wavelength regions of interest.

The stellar spectra of Arcturus (K1.2 III type) from *SpectroWeb*[1] (Lobel, 2006) was chosen as a reference for identifying the spectral lines in the U Mon spectra, and most line identifications were taken from the VALD-2 database (Kupka et al., 1999).

Figure 5.1 shows the U Mon spectrum obtained on JD 2458790.056 (2019 November 8) at three separate wavelength regions. The line identifications for some of the stronger lines are indicated and labelled with their species.

## 5.1 H$\alpha$, metallic and molecular line behaviour

Sequences of U Mon spectra stacked in time sequence, and labelled by pulsation phase (Figure 5.2), show the H$\alpha$ line (at ∼6563 Å) in emission and variable in line shape. Unfortunately the H$\alpha$ emission line is saturated during phases 0.71–82 (with tops of emission lines appearing "flat-topped"). The line profile is characterised by blueshifted emission and redshifted absorption. Emission behaviour in the H$\alpha$ line and line-profile variability is consistent with the model of two shocks waves passing through the stellar photosphere at around phases 0.1 and 0.6 (Pollard et al. 1997; Pollard & Cottrell 1995). There also seems to be an enhanced absorption component with H$\alpha$ emission during these phases which is consistent with the results of Pollard et al. (1997), who state a probable explanation for emission and absorption lines as; emission lines are a result of the emission in the de-excitation zone of the shock wave propagating through the stellar atmosphere, whereas absorption lines are formed as a consequence of either photospheric absorption or H$\alpha$ self-absorption above the shock front.

In Figure 5.3, the absorption line of Fe I at 6546.238 Å (Kupka et al., 1999), possibly blended with a Ti I line at 6546.268 Å (see Fig. 5.1), shows a dramatic blueshift in wavelength between phases 0.0–0.39, 0.47–0.71 and 1.15–1.35. A redshifted emission component is seen during the shock wave phases 0.71–0.82. In the same figure, there is evidence of shock-related behaviour of the Ti I lines at 6554.223 Å (Kupka et al., 1999) as the line goes into emission during phases 0.71–0.82. This behaviour is weakly apparent during phases 1.05–1.15.

Figure 5.4 shows that the strength of Fe I 6200.313 Å line (Kupka et al., 1999) appears to be weakest at phases 0.71–0.82 and 1.15. For the Fe I 6191.558 Å line (Lobel, 2008) (possibly blended with Ni I 6191.171 Å line (Kupka et al., 1999)), an emission component during phases 0.71–0.82 is seen. The emission is not evident

[1] http://spectra.freeshell.org/whyspectroweb.html

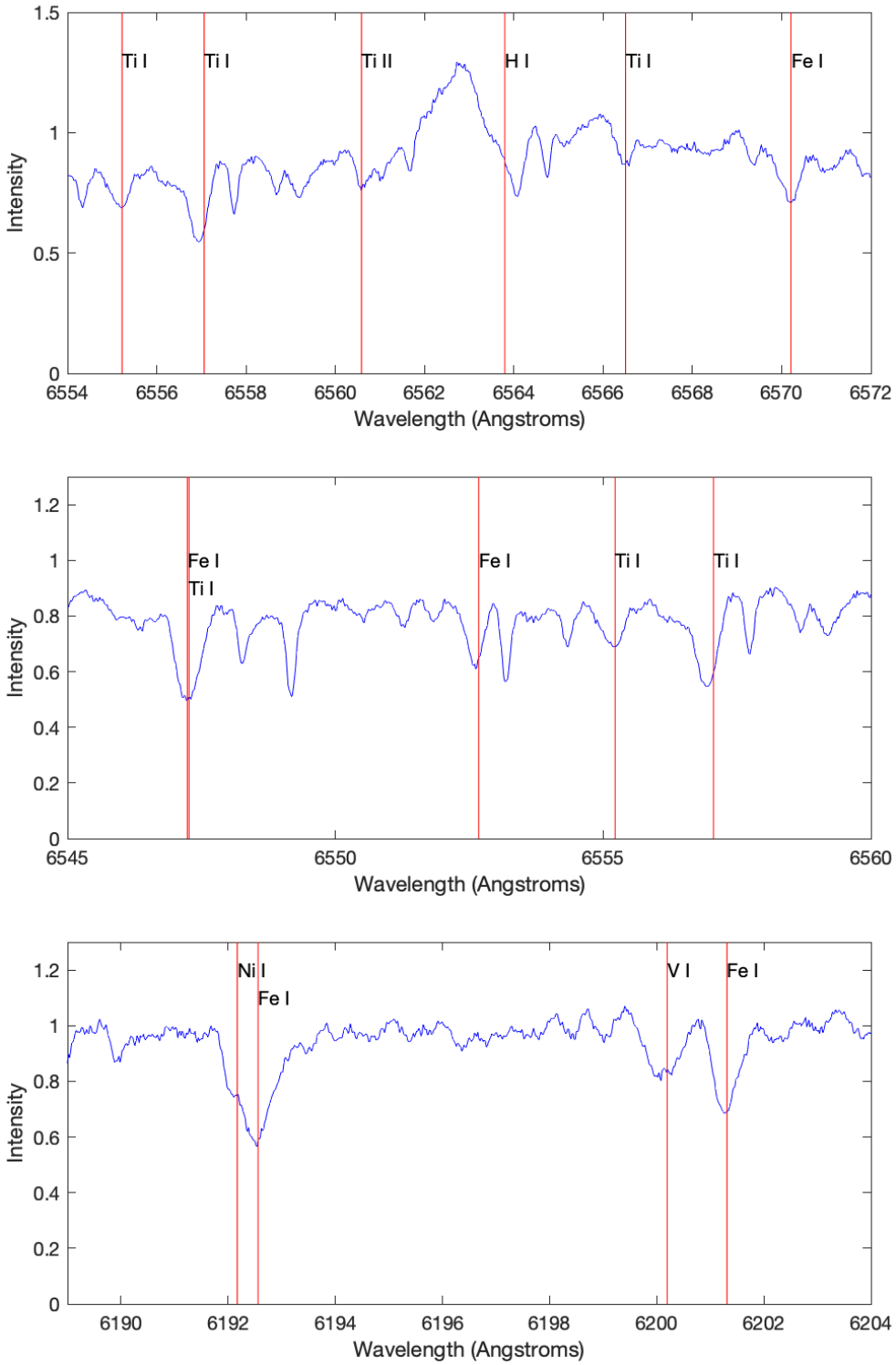


**Figure 5.1:** Line identification from *SpectroWeb* line list using the stellar spectrum at JD 2458790.056 (2019 November 8), phase=0.00. This spectrum has a wavelength offset of $\sim$+1.0 Å due to the stellar systemic and pulsational radial velocity at this phase.

during the observed phases 1.04–1.15. Line splitting or doubling is most apparent during phases 1.34–1.38.

Spectra taken around the two light curve minima at phases ∼0.0 and ∼0.5 display more "ripples" in the continuum level, indicative of the presence of weak molecular lines of TiO, and possibly CN, as observed in stars of later spectral type (Kupka et al. (1999), Pollard et al. (1997)).

Radial velocities measured from the Fe I line at 6200.313 Å (Kupka et al., 1999) and from cross-correlated line profiles are graphed in Fig. 5.5 in red and orange respectively. Line profile of Fe I 6750.150 AA appeared to be strongly affected by the shock waves and were unsuitable for Gaussian profile fitting. The Fe I line at 6200.313 Å was selected as it appears as a reasonably clean and unblended line in the spectra. This line was also one of three Fe I lines measured by Pollard et al. (1997) and McSaveney (2003), so a direct comparison with this older data could be undertaken. The radial velocity curve reproduced from Pollard et al. (1997) for the same 6200.313 Å Fe I line is shown in green in Fig. 5.5. All are phased using a pulsation period of 91.85 days, which was obtained using older (August 1990 - – May 2002) UCMJO photometry (Pollard et al. (1996) and McSaveney (2003)). The epoch used to phase the spectroscopic observations acquired in this study is JD 2458790.056. whilst the epoch used by Pollard et al. (1997) for the older radial velocities is JD 2448286.969. The radial velocity data from Pollard et al. (1997) are consistent with the results in this work as seen in Figure 5.5. The discontinuities at ∼0.2 and ∼0.6 in the radial velocity curves are apparent and are also in agreement with the results of Pollard et al. (1997).

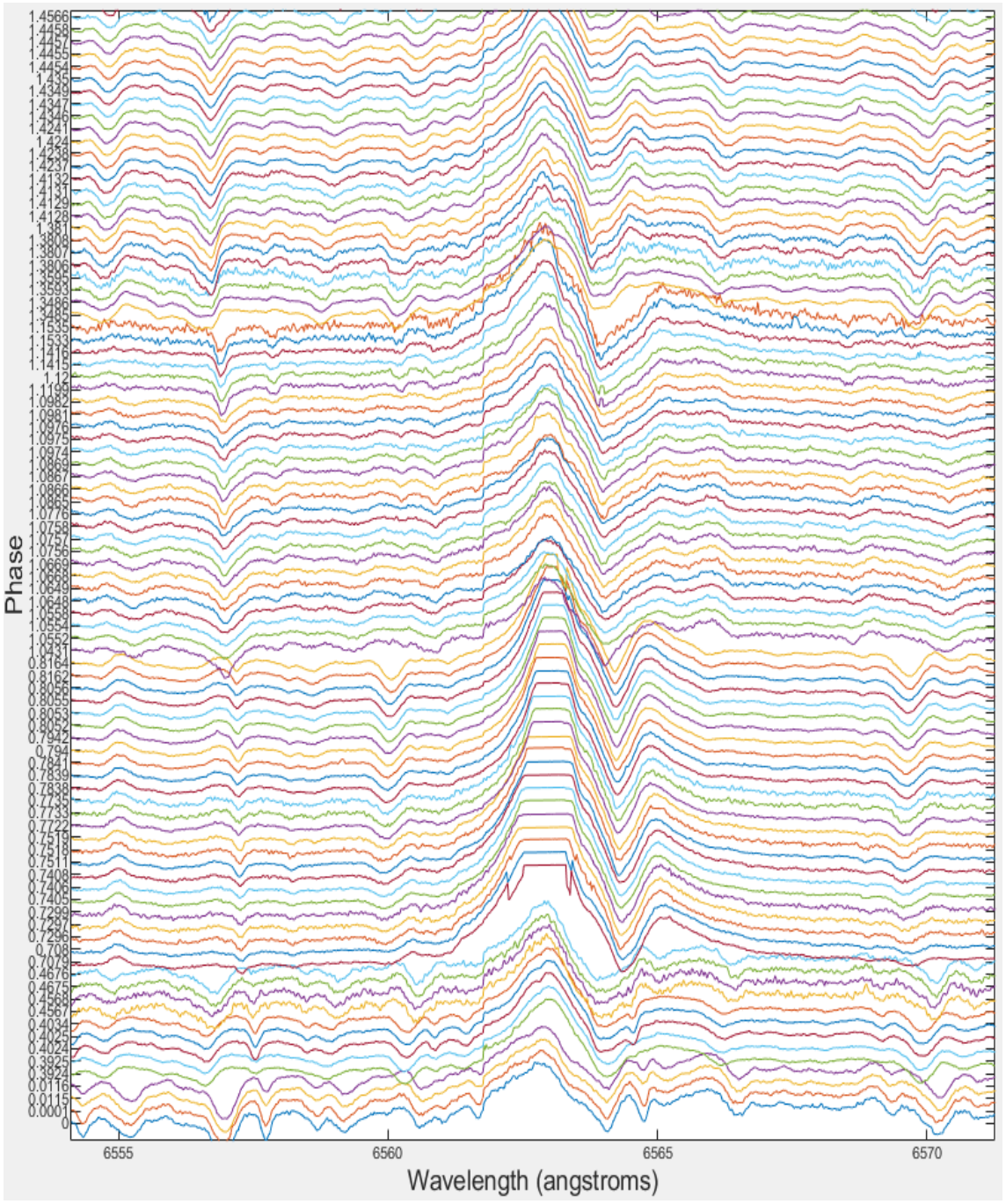


**Figure 5.2:** U Mon spectra in the wavelength region around the H$\alpha$-profile. The spectra are plotted in a time sequence from bottom to top, with pulsation phase indicated to the left of each spectrum (phased with period = 91.85 d and epoch = JD 2458790.056).

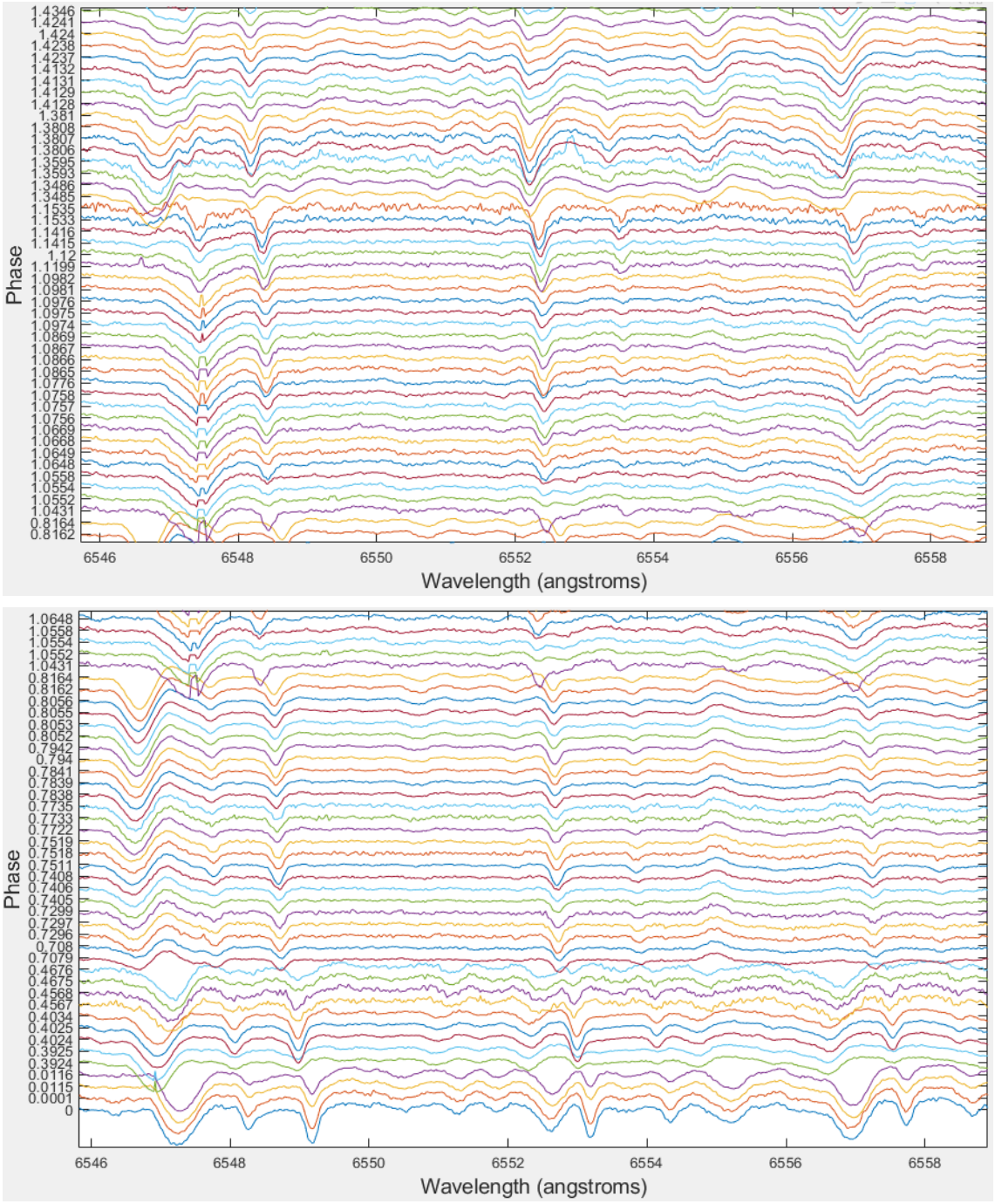


**Figure 5.3:** Stacked spectra of U Mon in the wavelength region around the Fe I 6546.238 Å line and the Ti I lines at 6554.223 and 6556.062 Å (phased with period = 91.85 d and epoch = JD 2458790.056).

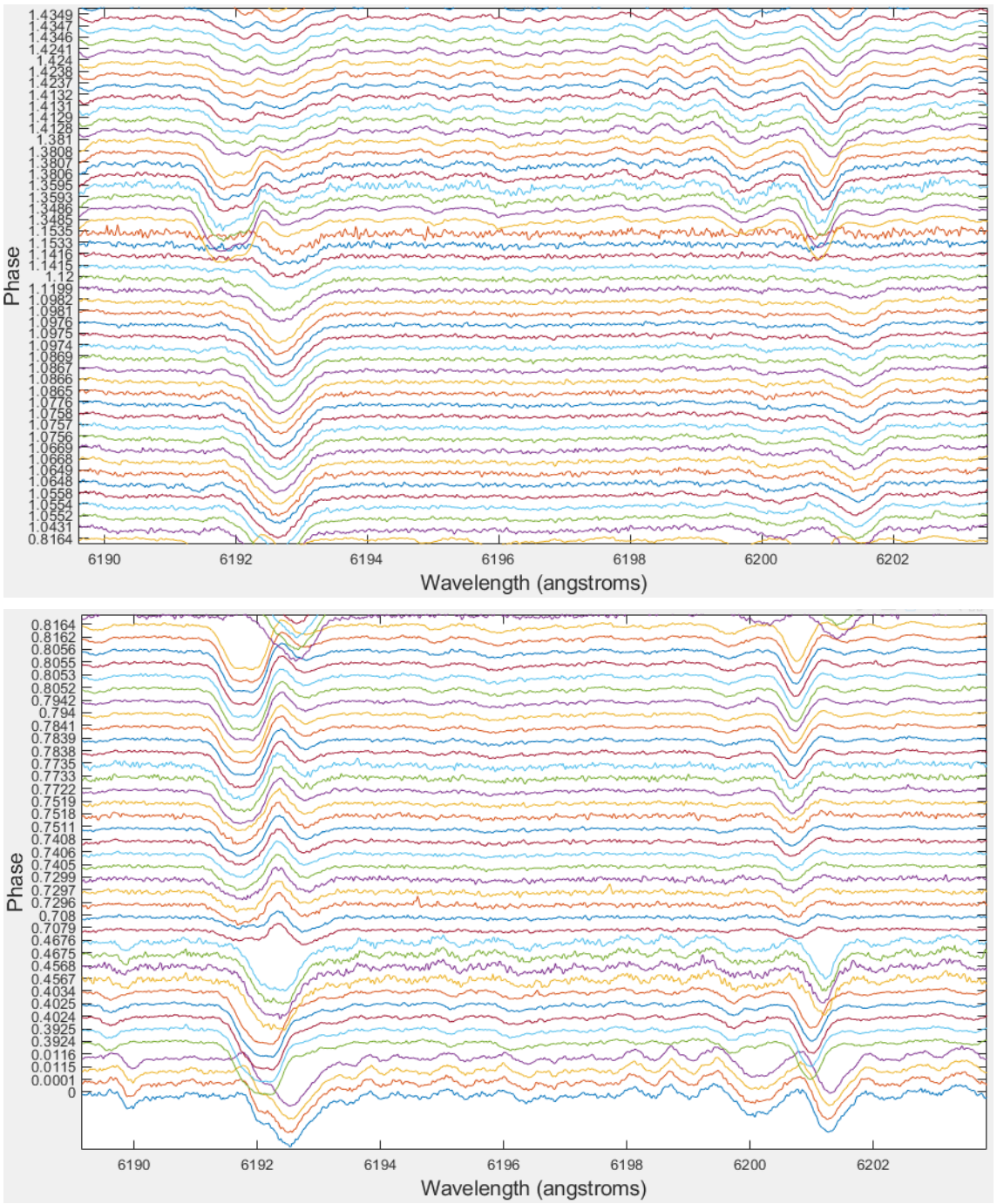


**Figure 5.4:** U Mon spectra of the region around the Fe I 6200.312 Å and Fe I 6191.558 Å line (phased with period = 91.85 d and epoch = JD 2458790.056).

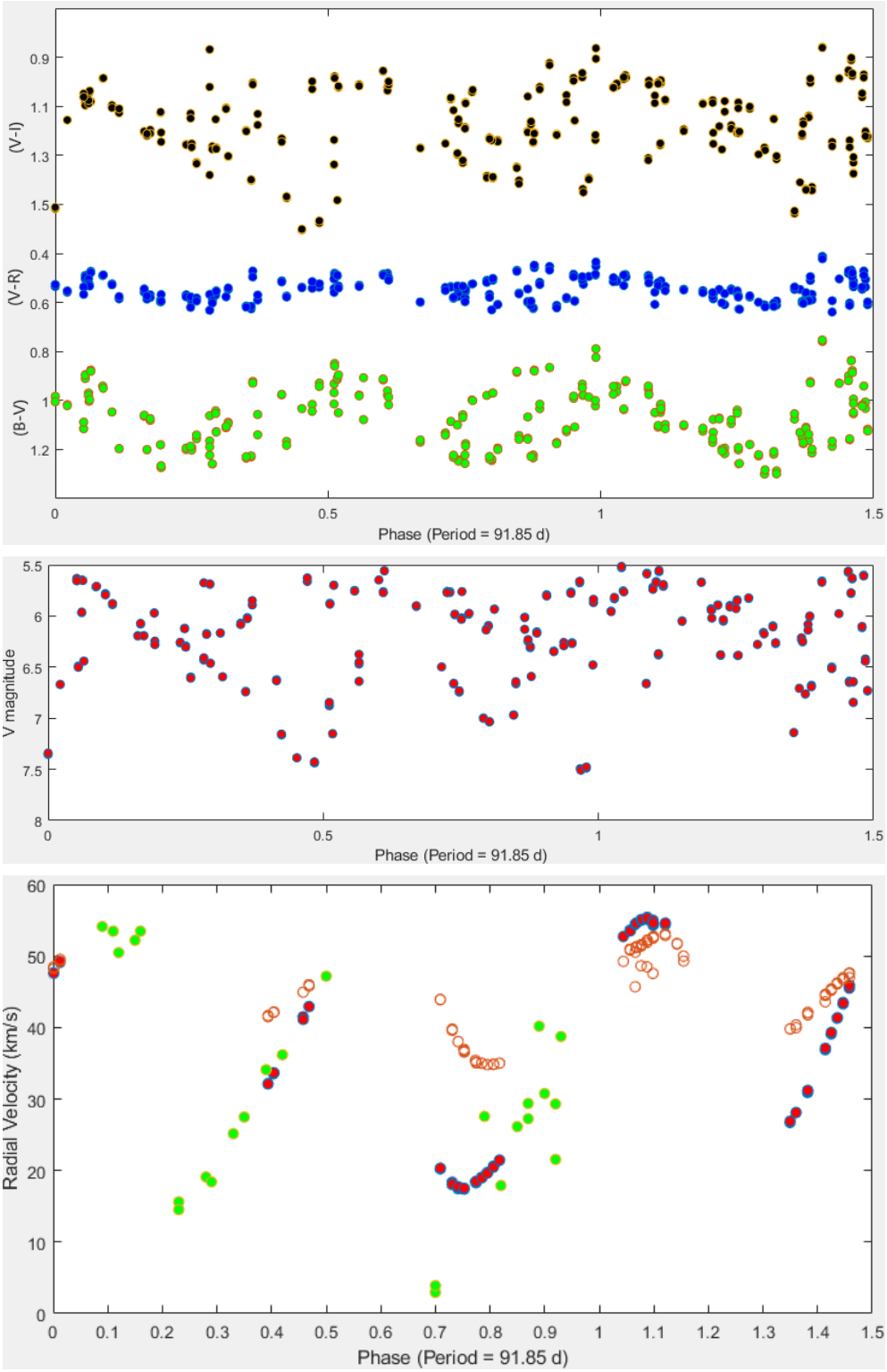


**Figure 5.5:** (Top) U Mon light and color curves reproduced using data from Pollard et al. (1996) and McSaveney (2003) (period = 91.85 d and epoch = JD 2450808.043). (Bottom) Radial velocities measured from: the cross-correlation profiles (orange); using the Fe I 6200.313 Å line from recent spectra (red); and reproduced using data from Pollard et al. 1997 (green); all phased with period = 91.85 d and epoch = JD 2458790.056 (this study) and JD 2448286.969 (from Pollard et al. 1997).

Radial velocities computed via cross correlation profiles and using the Fe I line at 6200.313 Å line both seem to be consistent with each other in phase and overall shape, but they do differ in amplitude, especially during phases ∼0.7–0.8. This is likely a testament to the varied shock-related behaviour of the numerous metallic lines used in cross-correlation process, caused by the constituents in different depths of the star's photosphere. During the shock phases, line-doubling and emission is seen in many metallic lines and the cross-correlation process will effectively "average-over" these velocities giving a mean velocity at certain phases and a smaller pulsation amplitude. This is in contrast to the spectral lines of a specific atomic species (such as the Fe I at 6200.313 Å), which form in a very localised part of the photosphere, and therefore give radial velocity curves which trace a very specific layer of the photosphere.

# Chapter 6

# Conclusions

Four RV Tauri stars (U Mon, AR Pup, IW Car and RU Cen) were analysed using visual and $V$ magnitude photometry from the AAVSO database and using recent $BV$ photometry from the UC Mt John Observatory and the Bright Star Monitor telescopes in Australia. The time baselines were extended on previous studies where possible. Differential photometry was carried out using AAVSO's `VPhot` while Fourier analysis and least-squares fitting was done in a pre-whitening manner through `Period04`. All the stars studied varied in both short and long-term brightness in a semi-regular (to greater or lesser extent) manner. The short-term periods and most of the long-term periods of the stars studied were found to be in reasonable agreement with the published values. Long-term variations were confirmed in all stars, the amplitudes of which appeared to be extremely variable. In the framework of the dust obscuration/stellar interaction model, this would indicate variable or clumpy dust, or variable degrees of interaction between stellar components.

Much longer-term variations were also seen for U Mon ($\sim$ 62.5 years), AR Pup ($\sim$ 39.5 years) and IW Car ($\sim$ 72.4 years). A conservative approach is required to draw conclusions about the authenticity of these very long-term periods. These periods may arise from the long-term irregular variations intrinsic to the stellar system, but their significance is low due to their similarity to the length of the dataset.

Multiple pulsational frequencies were apparent in the long-term visual data periodograms. Periodograms from the Fourier analysis had complex peak structures, possibly due as to changes in pulsational periods over time, or arising from "flips" in the deep-shallow light curve alternation with time. This may be either due to the dynamics of the complex system including interactions with the binary or the circumstellar disk, or due to the evolutionary changes in the stellar structure. Although the least-squares harmonic fits on the both short and long-term variation were generally good, the long-term behavior was quite variable, especially in the

amplitudes of the long-term periods. Wavelet analysis of two stars, U Mon and IW Car, explores the stability of the periods in these stars over longer time spans. This analysis revealed period changes in these stars with graphs of both long-term period and its amplitude showing changes in these parameters over time. Wavelet analysis of U Mon in particular revealed the period and amplitudes of its long-term periods to be quite variable.

U Mon was studied spectroscopically. Nearly 100 spectra were acquired over the course of five months, covering about 1.5 cycles of its pulsational period of 92 days. H$\alpha$ was seen in emission throughout the observations, with the line-profile behaviour consistent with the model given in Pollard et al. (1997). Line splitting/doubling of the Fe I 6191.558 Å line, an emission component of Fe I 6546.238 Å and the Ti I 6554.223 Å line going into emission serve as testaments to the pulsation-related shock wave phenomenon at specific phases. Molecular bands of TiO and CN were seen which points at the RVA Preston spectroscopic classification of U Mon. Radial velocities were calculated from two methods: cross-correlation function and Gaussian profile fitting to the line profile of specific atomic lines, spectrum by spectrum. The new pulsational radial velocity curve from the Fe I 6200.313 Å line was consistent with the pulsational radial velocity curve in Pollard et al. (1997) and showed well-defined discontinuities at phases $\sim$0.1–0.2, $\sim$0.6–0.7 and $\sim$1.1–1.2.

The results obtained in this thesis can be concluded as consequences of a number of complex processes happening in the stellar environment, stellar atmosphere and interior of the star. All the target stars studied are binaries or at least proposed to be binaries (Manick et al. 2017; Ertel et al. 2019; Maas et al. 2002; Pollard et al. 2006, with substantial amounts of warm dust as shown by their near infrared excesses (Lloyd Evans 1985, Pollard & Lloyd Evans 1999) – a proposition which suggests the existence of circumstellar or circumbinary disks (Maas et al. 2005, Bujarrabal et al. 2017) in the post AGB stage of evolution and with possible interactions between binary components. These binary-related atmospheric dynamics, working in a combination with the intrinsic stellar pulsations and perhaps long-term periodic dust obscuration, dictate the brightness variations depending on the perspective of the observer. We find that this work has strengthened observational evidence supporting this leading RV Tauri model. Further photometric and spectroscopic long-term monitoring of RV Tauri stars would add more depth to the current understanding of the true nature of pulsations and shocks, as observed from their light and spectral modulations, and in turn of the evolutionary phase, overall structure and dynamics of such stellar systems.

# Appendix A

# Photometry Results

**Table A.1:** UCMJO photometric observations of RU Cen in the $V$ filter.

| JD | V mag | V Err | JD | V mag | V Err |
|---|---|---|---|---|---|
| 2458827.104 | 9.063 | 0.002 | 2458886.979 | 8.968 | 0.002 |
| 2458827.104 | 9.042 | 0.002 | 2458886.979 | 8.999 | 0.002 |
| 2458827.104 | 9.054 | 0.002 | 2458887.955 | 8.979 | 0.002 |
| 2458833.062 | 8.536 | 0.002 | 2458887.955 | 8.947 | 0.002 |
| 2458833.062 | 8.542 | 0.002 | 2458887.956 | 8.984 | 0.002 |
| ‘ 2458833.062 | 8.539 | 0.002 | 2458888.948 | 8.858 | 0.002 |
| 2458838.042 | 8.429 | 0.002 | 2458888.949 | 8.873 | 0.003 |
| 2458838.042 | 8.443 | 0.002 | 2458888.949 | 8.948 | 0.003 |
| 2458838.042 | 8.467 | 0.002 | 2458889.943 | 8.882 | 0.003 |
| 2458840.036 | 8.479 | 0.002 | 2458890.945 | 8.788 | 0.002 |
| 2458840.036 | 8.462 | 0.002 | 2458890.945 | 8.804 | 0.002 |
| 2458840.036 | 8.501 | 0.002 | 2458890.946 | 8.823 | 0.002 |
| 2458844.023 | 8.638 | 0.002 | 2458900.961 | 8.61 | 0.002 |
| 2458844.024 | 8.663 | 0.002 | 2458900.961 | 8.68 | 0.002 |
| 2458844.024 | 8.592 | 0.002 | 2458900.961 | 8.624 | 0.002 |
| 2458848.017 | 8.885 | 0.004 | 2458904.929 | 8.589 | 0.002 |
| 2458848.017 | 8.932 | 0.004 | 2458904.93 | 8.591 | 0.002 |
| 2458848.017 | 8.948 | 0.004 | 2458904.93 | 8.595 | 0.002 |
| 2458861.106 | 8.9 | 0.003 | 2458908.929 | 8.7 | 0.002 |
| 2458861.999 | 8.721 | 0.003 | 2458908.929 | 8.725 | 0.002 |
| 2458862 | 8.784 | 0.002 | 2458908.929 | 8.734 | 0.002 |
| 2458862 | 8.776 | 0.002 | 2458910.936 | 8.783 | 0.002 |
| 2458862.975 | 8.665 | 0.002 | 2458910.937 | 8.801 | 0.002 |
| 2458862.975 | 8.643 | 0.002 | 2458910.937 | 8.828 | 0.002 |
| 2458862.976 | 8.674 | 0.002 | 2458912.917 | 8.93 | 0.002 |
| 2458864.006 | 8.616 | 0.002 | 2458912.918 | 8.939 | 0.002 |
| 2458864.006 | 8.586 | 0.002 | 2458912.918 | 8.949 | 0.002 |
| 2458864.006 | 8.595 | 0.002 | 2458913.901 | 8.976 | 0.002 |
| 2458865.986 | 8.444 | 0.002 | 2458913.902 | 8.98 | 0.002 |
| 2458865.986 | 8.492 | 0.002 | 2458919.915 | 9.316 | 0.002 |
| 2458865.986 | 8.497 | 0.002 | 2458919.915 | 9.335 | 0.002 |
| 2458867.021 | 8.532 | 0.003 | 2458919.915 | 9.331 | 0.002 |
| 2458867.021 | 8.53 | 0.003 | 2458921.927 | 9.423 | 0.002 |
| 2458867.021 | 8.518 | 0.003 | 2458921.928 | 9.411 | 0.002 |
| 2458867.985 | 8.437 | 0.001 | 2458921.928 | 9.428 | 0.002 |
| 2458867.985 | 8.401 | 0.001 | 2458922.911 | 9.324 | 0.004 |
| 2458867.986 | 8.427 | 0.002 | 2458922.911 | 9.368 | 0.003 |
| 2458870.983 | 8.41 | 0.002 | 2458922.911 | 9.328 | 0.003 |
| 2458870.983 | 8.399 | 0.002 | 2458925.892 | 9.106 | 0.002 |
| 2458870.984 | 8.413 | 0.002 | 2458925.892 | 9.078 | 0.002 |
| 2458872.06 | 8.468 | 0.002 | 2458925.892 | 9.11 | 0.002 |
| 2458872.061 | 8.45 | 0.002 | 2458926.881 | 8.933 | 0.002 |
| 2458872.061 | 8.452 | 0.001 | 2458926.881 | 8.991 | 0.002 |
| 2458875.944 | 8.62 | 0.002 | 2458926.881 | 9.009 | 0.002 |
| 2458875.945 | 8.565 | 0.002 | 2458933.884 | 8.379 | 0.001 |
| 2458875.945 | 8.604 | 0.002 | 2458933.884 | 8.375 | 0.001 |
| 2458885.013 | 8.982 | 0.002 | 2458933.884 | 8.398 | 0.001 |

**Table A.2:** BSM photometric observations of RU Cen in the $V$ filter.

| JD | V mag | V Err | JD | V mag | V Err |
|---|---|---|---|---|---|
| 2458558.085 | 8.998 | 0.003 | 2458630.019 | 9.09 | 0.003 |
| 2458558.088 | 9.011 | 0.002 | 2458630.021 | 9.165 | 0.001 |
| 2458558.091 | 9 | 0.002 | 2458630.024 | 9.169 | 0.002 |
| 2458576.059 | 8.747 | 0.002 | 2458630.999 | 9.095 | 0.002 |
| 2458576.062 | 8.763 | 0.002 | 2458631.002 | 9.121 | 0.001 |
| 2458576.065 | 8.756 | 0.002 | 2458631.004 | 9.072 | 0.002 |
| 2458585.975 | 8.818 | 0.002 | 2458632 | 9.058 | 0.002 |
| 2458585.978 | 8.829 | 0.002 | 2458632.003 | 9.046 | 0.002 |
| 2458585.981 | 8.825 | 0.002 | 2458632.006 | 9.136 | 0.002 |
| 2458595.143 | 9.632 | 0.002 | 2458633.108 | 9.036 | 0.002 |
| 2458595.146 | 9.58 | 0.002 | 2458633.111 | 9.025 | 0.002 |
| 2458595.149 | 9.643 | 0.004 | 2458633.114 | 9.056 | 0.004 |
| 2458610.046 | 8.676 | 0.002 | 2458637.113 | 8.847 | 0.002 |
| 2458611.04 | 8.667 | 0.002 | 2458637.116 | 8.847 | 0.002 |
| 2458611.042 | 8.729 | 0.002 | 2458637.118 | 8.822 | 0.002 |
| 2458611.045 | 8.682 | 0.004 | 2458637.974 | 8.813 | 0.004 |
| 2458616.026 | 8.76 | 0.004 | 2458637.977 | 8.808 | 0.004 |
| 2458616.028 | 8.769 | 0.004 | 2458637.979 | 8.827 | 0.004 |
| 2458616.031 | 8.76 | 0.003 | 2458639.053 | 8.847 | 0.003 |
| 2458618.018 | 8.883 | 0.003 | 2458639.056 | 8.819 | 0.003 |
| 2458618.021 | 8.889 | 0.002 | 2458639.059 | 8.815 | 0.002 |
| 2458618.023 | 8.887 | 0.002 | 2458652.116 | 8.98 | 0.002 |
| 2458620.052 | 8.962 | 0.002 | 2458652.121 | 8.931 | 0.002 |
| 2458620.055 | 9.021 | 0.002 | 2458652.986 | 8.931 | 0.002 |
| 2458620.058 | 8.938 | 0.002 | 2458652.988 | 9.02 | 0.002 |
| 2458621.029 | 8.977 | 0.002 | 2458652.991 | 9.037 | 0.002 |
| 2458621.032 | 9.016 | 0.002 | 2458653.987 | 8.994 | 0.002 |
| 2458621.035 | 8.994 | 0.002 | 2458653.99 | 9.067 | 0.002 |
| 2458622.978 | 9.118 | 0.002 | 2458657.923 | 9.341 | 0.002 |
| 2458622.982 | 9.16 | 0.002 | 2458657.926 | 9.314 | 0.002 |
| 2458622.985 | 9.121 | 0.002 | 2458657.929 | 9.312 | 0.002 |
| 2458624.003 | 9.123 | 0.003 | 2458659.877 | 9.503 | 0.003 |
| 2458624.007 | 9.094 | 0.003 | 2458659.88 | 9.499 | 0.003 |
| 2458624.01 | 9.143 | 0.003 | 2458659.884 | 9.496 | 0.003 |
| 2458625.982 | 9.143 | 0.001 | 2458660.891 | 9.551 | 0.001 |
| 2458625.986 | 9.161 | 0.001 | 2458660.895 | 9.545 | 0.001 |
| 2458625.989 | 9.16 | 0.002 | 2458660.898 | 9.544 | 0.002 |
| 2458629.005 | 9.134 | 0.002 | 2458661.897 | 9.61 | 0.002 |
| 2458629.008 | 9.233 | 0.002 | 2458661.9 | 9.593 | 0.002 |

**Table A.3:** BSM photometric observations of RU Cen in the $V$ filter.

| JD | V mag | V Err |
|---|---|---|
| 2458661.904 | 9.58 | 0.003 |
| 2458666.039 | 9.465 | 0.001 |
| 2458666.042 | 9.472 | 0.002 |
| 2458666.045 | 9.508 | 0.002 |
| 2458666.981 | 9.265 | 0.001 |
| 2458666.983 | 9.344 | 0.002 |
| 2458666.986 | 9.403 | 0.002 |
| 2458667.915 | 9.195 | 0.002 |
| 2458667.919 | 9.196 | 0.002 |
| 2458667.922 | 9.212 | 0.002 |
| 2458671.989 | 8.658 | 0.002 |
| 2458671.992 | 8.672 | 0.004 |
| 2458671.994 | 8.695 | 0.002 |
| 2458673.909 | 8.611 | 0.002 |
| 2458673.912 | 8.614 | 0.002 |
| 2458673.915 | 8.621 | 0.004 |
| 2458676.008 | 8.587 | 0.004 |
| 2458676.011 | 8.563 | 0.004 |
| 2458676.013 | 8.571 | 0.003 |
| 2458676.985 | 8.565 | 0.003 |
| 2458676.987 | 8.512 | 0.002 |
| 2458676.99 | 8.55 | 0.002 |
| 2458677.965 | 8.558 | 0.002 |
| 2458677.968 | 8.547 | 0.002 |
| 2458677.971 | 8.533 | 0.002 |
| 2458678.96 | 8.527 | 0.002 |
| 2458678.965 | 8.616 | 0.002 |
| 2458679.976 | 8.56 | 0.002 |
| 2458679.979 | 8.658 | 0.002 |
| 2458680.977 | 8.605 | 0.002 |
| 2458680.98 | 8.711 | 0.002 |
| 2458680.982 | 8.623 | 0.002 |
| 2458681.979 | 8.686 | 0.002 |
| 2458681.982 | 8.656 | 0.002 |

| JD | V mag | V Err |
|---|---|---|
| 2458683.877 | 8.807 | 0.001 |
| 2458683.881 | 8.813 | 0.002 |
| 2458683.884 | 8.822 | 0.002 |
| 2458693.023 | 9.393 | 0.002 |
| 2458693.026 | 9.425 | 0.002 |
| 2458693.029 | 9.405 | 0.002 |
| 2458693.973 | 9.447 | 0.002 |
| 2458693.975 | 9.45 | 0.002 |
| 2458693.978 | 9.417 | 0.002 |
| 2458695.968 | 9.458 | 0.002 |
| 2458695.971 | 9.505 | 0.002 |
| 2458695.973 | 9.48 | 0.003 |
| 2458704.959 | 8.756 | 0.003 |
| 2458704.961 | 8.735 | 0.003 |
| 2458704.964 | 8.754 | 0.002 |
| 2458706.966 | 8.714 | 0.002 |
| 2458706.969 | 8.693 | 0.002 |
| 2458706.971 | 8.698 | 0.002 |
| 2458707.969 | 8.686 | 0.002 |
| 2458707.971 | 8.702 | 0.002 |
| 2458707.974 | 8.684 | 0.002 |
| 2458716.961 | 8.979 | 0.002 |
| 2458716.964 | 8.981 | 0.002 |
| 2458716.967 | 8.983 | 0.002 |
| 2458657.929 | 9.312 | 0.002 |
| 2458659.877 | 9.503 | 0.002 |
| 2458659.88 | 9.499 | 0.002 |
| 2458659.884 | 9.496 | 0.002 |
| 2458660.891 | 9.551 | 0.002 |
| 2458660.895 | 9.545 | 0.002 |
| 2458660.898 | 9.544 | 0.002 |
| 2458661.897 | 9.61 | 0.002 |
| 2458661.9 | 9.593 | 0.002 |

**Table A.4:** UCMJO photometric observations of RU Cen in the $B$ filter.

| JD | B mag | B Err |
|---|---|---|
| 2458827.103 | 8.733 | 0.002 |
| 2458827.103 | 8.749 | 0.002 |
| 2458827.103 | 8.728 | 0.002 |
| 2458833.061 | 8.215 | 0.002 |
| 2458833.062 | 8.224 | 0.002 |
| 2458833.062 | 8.252 | 0.001 |
| 2458838.041 | 8.293 | 0.002 |
| 2458838.041 | 8.266 | 0.002 |
| 2458838.042 | 8.294 | 0.002 |
| 2458840.035 | 8.444 | 0.002 |
| 2458840.035 | 8.562 | 0.002 |
| 2458840.036 | 8.379 | 0.002 |
| 2458844.023 | 8.899 | 0.002 |
| 2458844.023 | 8.554 | 0.002 |
| 2458844.023 | 8.539 | 0.002 |
| 2458848.016 | 9.531 | 0.002 |
| 2458848.016 | 9.572 | 0.003 |
| 2458848.016 | 9.51 | 0.003 |
| 2458861.105 | 8.568 | 0.003 |
| 2458861.999 | 8.494 | 0.002 |
| 2458861.999 | 8.527 | 0.002 |
| 2458861.999 | 8.569 | 0.002 |
| 2458862.975 | 8.359 | 0.002 |
| 2458862.975 | 8.583 | 0.002 |
| 2458862.975 | 8.385 | 0.002 |
| 2458864.006 | 8.317 | 0.002 |
| 2458864.006 | 8.304 | 0.002 |
| 2458865.985 | 8.23 | 0.002 |
| 2458865.985 | 8.176 | 0.002 |
| 2458865.986 | 8.217 | 0.002 |
| 2458867.019 | 8.585 | 0.002 |
| 2458867.02 | 8.576 | 0.002 |
| 2458867.02 | 8.588 | 0.002 |
| 2458867.984 | 8.212 | 0.002 |
| 2458867.984 | 8.164 | 0.002 |
| 2458867.985 | 8.218 | 0.002 |
| 2458870.982 | 8.196 | 0.002 |
| 2458870.983 | 8.103 | 0.002 |
| 2458870.983 | 8.211 | 0.001 |
| 2458872.06 | 8.249 | 0.002 |
| 2458872.06 | 8.254 | 0.003 |
| 2458875.943 | 8.979 | 0.002 |
| 2458875.944 | 9.068 | 0.002 |
| 2458875.944 | 8.652 | 0.003 |
| 2458886.977 | 9.19 | 0.002 |
| 2458886.978 | 8.827 | 0.002 |
| 2458886.978 | 8.832 | 0.001 |
| 2458887.954 | 8.987 | 0.002 |
| 2458887.954 | 8.975 | 0.002 |
| 2458887.955 | 8.914 | 0.002 |
| 2458888.947 | 8.687 | 0.002 |
| 2458888.948 | 8.719 | 0.002 |
| 2458888.948 | 8.918 | 0.002 |
| 2458890.944 | 8.533 | 0.001 |
| 2458890.945 | 8.572 | 0.002 |
| 2458890.945 | 8.516 | 0.002 |
| 2458900.96 | 8.488 | 0.002 |
| 2458900.96 | 8.438 | 0.002 |
| 2458900.96 | 8.46 | 0.002 |
| 2458904.928 | 8.513 | 0.002 |
| 2458904.929 | 8.499 | 0.002 |
| 2458904.929 | 8.501 | 0.002 |
| 2458908.928 | 8.621 | 0.002 |
| 2458908.928 | 8.642 | 0.002 |
| 2458908.929 | 8.61 | 0.003 |
| 2458910.935 | 8.939 | 0.003 |
| 2458910.936 | 8.762 | 0.003 |
| 2458910.936 | 9.025 | 0.002 |
| 2458911.94 | 8.848 | 0.002 |
| 2458911.941 | 8.891 | 0.002 |
| 2458911.941 | 8.88 | 0.002 |
| 2458912.916 | 8.93 | 0.002 |
| 2458912.917 | 8.935 | 0.002 |
| 2458912.917 | 8.949 | 0.002 |
| 2458913.9 | 9.054 | 0.002 |
| 2458913.9 | 9.052 | 0.002 |
| 2458913.901 | 9.083 | 0.002 |
| 2458919.914 | 9.428 | 0.002 |
| 2458919.914 | 9.4 | 0.002 |
| 2458919.914 | 9.432 | 0.002 |
| 2458921.926 | 9.366 | 0.002 |
| 2458921.927 | 9.316 | 0.002 |
| 2458921.927 | 9.357 | 0.002 |
| 2458922.91 | 9.302 | 0.002 |
| 2458922.91 | 9.315 | 0.002 |
| 2458922.91 | 9.336 | 0.002 |
| 2458925.891 | 8.932 | 0.001 |
| 2458925.891 | 8.886 | 0.002 |
| 2458925.891 | 8.895 | 0.003 |
| 2458926.88 | 8.617 | 0.002 |
| 2458926.88 | 8.664 | 0.002 |
| 2458926.88 | 8.675 | 0.003 |
| 2458933.882 | 8.138 | 0.002 |
| 2458933.883 | 8.14 | 0.002 |
| 2458933.883 | 8.126 | 0.001 |

**Table A.5:** UCMJO photometric observations of AR Pup in the $V$ filter.

| JD | V mag | V Err |
|---|---|---|
| 2458818.998 | 9.116 | 0.008 |
| 2458818.999 | 9.115 | 0.007 |
| 2458827.059 | 9.105 | 0.008 |
| 2458827.059 | 9.112 | 0.008 |
| 2458832.908 | 9.193 | 0.004 |
| 2458832.908 | 9.157 | 0.003 |
| 2458832.908 | 9.173 | 0.003 |
| 2458835.998 | 9.229 | 0.002 |
| 2458835.998 | 9.229 | 0.002 |
| 2458835.998 | 9.236 | 0.002 |
| 2458838.033 | 9.277 | 0.002 |
| 2458838.033 | 9.265 | 0.002 |
| 2458838.034 | 9.269 | 0.002 |
| 2458847.16 | 9.776 | 0.007 |
| 2458847.16 | 9.72 | 0.006 |
| 2458847.899 | 9.643 | 0.003 |
| 2458847.899 | 9.651 | 0.003 |
| 2458850.058 | 9.647 | 0.004 |
| 2458850.058 | 9.632 | 0.004 |
| 2458850.058 | 9.641 | 0.004 |
| 2458852.045 | 9.59 | 0.004 |
| 2458852.045 | 9.583 | 0.003 |
| 2458852.045 | 9.62 | 0.003 |
| 2458861.067 | 9.107 | 0.002 |
| 2458861.067 | 9.149 | 0.002 |
| 2458861.067 | 9.137 | 0.002 |
| 2458861.899 | 9.076 | 0.003 |
| 2458861.9 | 9.08 | 0.003 |
| 2458862.967 | 9.043 | 0.002 |
| 2458862.967 | 9.034 | 0.002 |
| 2458862.967 | 9.047 | 0.002 |
| 2458865.927 | 9 | 0.002 |
| 2458865.927 | 8.96 | 0.002 |
| 2458866.96 | 9.034 | 0.002 |
| 2458866.961 | 9.023 | 0.002 |
| 2458867.007 | 9.619 | 0.003 |
| 2458867.007 | 9.615 | 0.004 |
| 2458867.926 | 9 | 0.002 |
| 2458867.927 | 9.014 | 0.002 |
| 2458867.927 | 8.98 | 0.002 |
| 2458870.97 | 9.128 | 0.002 |
| 2458872.041 | 9.169 | 0.002 |
| 2458872.041 | 9.212 | 0.002 |
| 2458872.041 | 9.193 | 0.002 |
| 2458875.016 | 9.242 | 0.005 |
| 2458875.016 | 9.285 | 0.005 |
| 2458875.016 | 9.236 | 0.005 |
| 2458875.931 | 9.239 | 0.002 |
| 2458875.931 | 9.237 | 0.002 |
| 2458875.932 | 9.234 | 0.005 |
| 2458884.989 | 9.374 | 0.005 |
| 2458884.989 | 9.342 | 0.005 |
| 2458884.99 | 9.329 | 0.002 |
| 2458886.96 | 9.338 | 0.002 |
| 2458886.96 | 9.26 | 0.002 |
| 2458886.96 | 9.366 | 0.004 |
| 2458887.941 | 9.323 | 0.004 |
| 2458887.941 | 9.318 | 0.004 |
| 2458887.942 | 9.309 | 0.003 |
| 2458888.924 | 9.291 | 0.003 |
| 2458889.918 | 9.24 | 0.003 |
| 2458889.918 | 9.278 | 0.002 |
| 2458889.919 | 9.22 | 0.002 |
| 2458890.931 | 9.116 | 0.002 |
| 2458892.91 | 9.124 | 0.002 |
| 2458892.911 | 9.116 | 0.003 |
| 2458892.911 | 9.125 | 0.003 |
| 2458904.915 | 9.106 | 0.003 |
| 2458904.916 | 9.12 | 0.002 |
| 2458904.916 | 9.122 | 0.002 |
| 2458908.915 | 9.251 | 0.002 |
| 2458908.915 | 9.244 | 0.002 |
| 2458908.915 | 9.23 | 0.002 |
| 2458909.955 | 9.264 | 0.002 |
| 2458909.956 | 9.247 | 0.002 |
| 2458909.956 | 9.276 | 0.002 |
| 2458910.913 | 9.269 | 0.002 |
| 2458910.913 | 9.268 | 0.002 |
| 2458910.913 | 9.306 | 0.005 |
| 2458911.923 | 9.231 | 0.004 |
| 2458911.923 | 9.26 | 0.004 |
| 2458913.882 | 9.301 | 0.003 |
| 2458913.882 | 9.322 | 0.003 |
| 2458913.883 | 9.34 | 0.003 |
| 2458919.895 | 9.593 | 0.004 |
| 2458919.896 | 9.588 | 0.008 |
| 2458919.896 | 9.593 | 0.003 |
| 2458921.908 | 9.605 | 0.002 |
| 2458921.909 | 9.599 | 0.002 |
| 2458921.909 | 9.623 | 0.002 |
| 2458923.871 | 9.605 | 0.002 |
| 2458923.871 | 9.616 | 0.003 |
| 2458925.867 | 9.608 | 0.002 |
| 2458925.868 | 9.568 | 0.002 |
| 2458925.868 | 9.604 | 0.002 |
| 2458926.857 | 9.513 | 0.002 |
| 2458933.864 | 9.151 | 0.01 |
| 2458933.864 | 9.141 | 0.007 |
| 2458933.864 | 9.129 | 0.003 |

**Table A.6:** BSM photometric observations of AR Pup in the $V$ filter.

| JD | V mag | V Err |
|---|---|---|
| 2458818.998 | 9.116 | 0.005 |
| 2458818.999 | 9.115 | 0.005 |
| 2458827.059 | 9.105 | 0.005 |
| 2458827.059 | 9.112 | 0.002 |
| 2458832.908 | 9.193 | 0.002 |
| 2458832.908 | 9.157 | 0.002 |
| 2458832.908 | 9.173 | 0.004 |
| 2458835.998 | 9.229 | 0.004 |
| 2458835.998 | 9.229 | 0.004 |
| 2458835.998 | 9.236 | 0.003 |
| 2458838.033 | 9.277 | 0.003 |
| 2458838.033 | 9.265 | 0.003 |
| 2458838.034 | 9.269 | 0.002 |
| 2458847.899 | 9.643 | 0.002 |
| 2458847.899 | 9.651 | 0.002 |
| 2458850.058 | 9.647 | 0.002 |
| 2458850.058 | 9.632 | 0.003 |
| 2458850.058 | 9.641 | 0.003 |
| 2458852.045 | 9.59 | 0.003 |
| 2458852.045 | 9.583 | 0.002 |
| 2458852.045 | 9.62 | 0.002 |
| 2458861.067 | 9.107 | 0.002 |
| 2458861.067 | 9.149 | 0.002 |
| 2458861.067 | 9.137 | 0.002 |
| 2458861.899 | 9.076 | 0.002 |
| 2458861.9 | 9.08 | 0.002 |
| 2458862.967 | 9.043 | 0.002 |
| 2458862.967 | 9.034 | 0.002 |
| 2458862.967 | 9.047 | 0.002 |
| 2458865.927 | 9 | 0.005 |
| 2458865.927 | 8.96 | 0.004 |

| JD | V mag | V Err |
|---|---|---|
| 2458866.96 | 9.034 | 0.008 |
| 2458866.961 | 9.023 | 0.007 |
| 2458867.926 | 9 | 0.008 |
| 2458867.927 | 9.014 | 0.008 |
| 2458870.97 | 9.128 | 0.004 |
| 2458872.041 | 9.169 | 0.003 |
| 2458872.041 | 9.212 | 0.003 |
| 2458872.041 | 9.193 | 0.002 |
| 2458875.016 | 9.242 | 0.002 |
| 2458875.016 | 9.285 | 0.002 |
| 2458875.016 | 9.236 | 0.002 |
| 2458875.931 | 9.239 | 0.002 |
| 2458875.931 | 9.237 | 0.002 |
| 2458875.932 | 9.234 | 0.007 |
| 2458884.989 | 9.374 | 0.006 |
| 2458884.989 | 9.342 | 0.003 |
| 2458884.99 | 9.329 | 0.003 |
| 2458886.96 | 9.338 | 0.004 |
| 2458886.96 | 9.26 | 0.004 |
| 2458886.96 | 9.366 | 0.004 |
| 2458887.941 | 9.323 | 0.004 |
| 2458887.941 | 9.318 | 0.003 |
| 2458887.942 | 9.309 | 0.003 |
| 2458888.924 | 9.291 | 0.002 |
| 2458889.918 | 9.24 | 0.002 |
| 2458889.919 | 9.22 | 0.002 |
| 2458890.931 | 9.116 | 0.003 |
| 2458892.91 | 9.124 | 0.003 |
| 2458892.911 | 9.116 | 0.002 |
| 2458892.911 | 9.125 | 0.002 |

**Table A.7:** UCMJO photometric observations of AR Pup in the $B$ filter.

| JD | B mag | B Err |
|---|---|---|
| 2458818.998 | 9.613 | 0.01 |
| 2458827.059 | 9.74 | 0.014 |
| 2458832.907 | 9.982 | 0.005 |
| 2458832.907 | 10.018 | 0.005 |
| 2458832.908 | 10.05 | 0.005 |
| 2458835.997 | 10.119 | 0.003 |
| 2458835.997 | 10.123 | 0.002 |
| 2458835.998 | 10.119 | 0.002 |
| 2458838.033 | 10.195 | 0.002 |
| 2458838.033 | 10.213 | 0.002 |
| 2458838.033 | 10.184 | 0.002 |
| 2458839.944 | 10.385 | 0.004 |
| 2458839.945 | 10.344 | 0.004 |
| 2458839.945 | 10.303 | 0.003 |
| 2458847.899 | 10.595 | 0.005 |
| 2458847.899 | 10.629 | 0.005 |
| 2458847.899 | 10.552 | 0.005 |
| 2458850.057 | 10.546 | 0.007 |
| 2458850.057 | 10.519 | 0.006 |
| 2458850.057 | 10.561 | 0.007 |
| 2458852.045 | 10.439 | 0.005 |
| 2458852.045 | 10.424 | 0.004 |
| 2458861.066 | 9.843 | 0.003 |
| 2458861.066 | 9.842 | 0.003 |
| 2458861.066 | 9.812 | 0.003 |
| 2458861.899 | 9.792 | 0.003 |
| 2458861.899 | 9.774 | 0.003 |
| 2458862.966 | 9.727 | 0.002 |
| 2458862.966 | 9.736 | 0.002 |
| 2458862.966 | 9.741 | 0.002 |
| 2458866.959 | 9.743 | 0.003 |
| 2458866.96 | 9.778 | 0.003 |
| 2458867.006 | 8.549 | 0.001 |
| 2458867.006 | 8.532 | 0.001 |
| 2458867.925 | 9.813 | 0.001 |
| 2458867.926 | 9.789 | 0.002 |
| 2458867.926 | 9.759 | 0.002 |
| 2458872.04 | 10.024 | 0.002 |
| 2458872.04 | 10.017 | 0.003 |
| 2458872.04 | 10.008 | 0.003 |
| 2458875.015 | 10.132 | 0.003 |
| 2458875.015 | 10.144 | 0.006 |
| 2458875.016 | 10.122 | 0.006 |
| 2458875.93 | 10.137 | 0.007 |
| 2458884.988 | 10.07 | 0.006 |
| 2458875.016 | 9.236 | 0.005 |
| 2458875.931 | 9.239 | 0.005 |
| 2458875.931 | 9.237 | 0.005 |
| 2458933.864 | 9.129 | 0.004 |

| JD | B mag | B Err |
|---|---|---|
| 2458884.988 | 10.047 | 0.003 |
| 2458884.989 | 10.059 | 0.003 |
| 2458886.959 | 10.05 | 0.003 |
| 2458887.94 | 9.972 | 0.003 |
| 2458887.94 | 9.968 | 0.003 |
| 2458887.941 | 10.017 | 0.003 |
| 2458888.922 | 9.946 | 0.002 |
| 2458888.923 | 9.924 | 0.002 |
| 2458888.923 | 9.907 | 0.002 |
| 2458890.93 | 9.77 | 0.003 |
| 2458890.931 | 9.8 | 0.002 |
| 2458890.931 | 9.763 | 0.003 |
| 2458892.909 | 9.741 | 0.002 |
| 2458892.91 | 9.724 | 0.002 |
| 2458892.91 | 9.703 | 0.002 |
| 2458904.914 | 9.935 | 0.003 |
| 2458904.915 | 9.942 | 0.003 |
| 2458904.915 | 9.939 | 0.003 |
| 2458908.914 | 10.135 | 0.004 |
| 2458908.914 | 10.151 | 0.005 |
| 2458908.915 | 10.153 | 0.005 |
| 2458909.954 | 10.161 | 0.005 |
| 2458909.955 | 10.169 | 0.005 |
| 2458909.955 | 10.167 | 0.005 |
| 2458910.912 | 10.172 | 0.003 |
| 2458910.912 | 10.188 | 0.003 |
| 2458911.922 | 10.16 | 0.003 |
| 2458913.881 | 10.265 | 0.003 |
| 2458913.881 | 10.273 | 0.003 |
| 2458913.882 | 10.263 | 0.003 |
| 2458919.894 | 10.564 | 0.003 |
| 2458919.895 | 10.57 | 0.003 |
| 2458919.895 | 10.582 | 0.003 |
| 2458921.907 | 10.571 | 0.004 |
| 2458921.908 | 10.579 | 0.003 |
| 2458921.908 | 10.573 | 0.003 |
| 2458925.866 | 10.452 | 0.004 |
| 2458925.867 | 10.45 | 0.003 |
| 2458925.867 | 10.45 | 0.003 |
| 2458926.855 | 10.268 | 0.002 |
| 2458926.855 | 10.357 | 0.002 |
| 2458926.856 | 10.346 | 0.002 |
| 2458933.863 | 9.811 | 0.001 |
| 2458933.863 | 9.827 | 0.002 |
| 2458933.864 | 9.816 | 0.003 |
| 2458875.931 | 9.239 | 0.001 |
| 2458875.931 | 9.237 | 0.002 |
| 2458933.864 | 9.129 | 0.003 |

**Table A.8:** UCMJO photometric observations of IW Car in the $V$ filter.

| JD | V mag | V Err | JD | V mag | V Err |
|---|---|---|---|---|---|
| 2458832.905 | 8.591 | 0.003 | 2458888.929 | 8.666 | 0.001 |
| 2458832.905 | 8.565 | 0.003 | 2458890.936 | 8.664 | 0.003 |
| 2458832.905 | 8.566 | 0.003 | 2458890.937 | 8.697 | 0.003 |
| 2458835.995 | 8.536 | 0.003 | 2458890.937 | 8.649 | 0.002 |
| 2458835.995 | 8.509 | 0.003 | 2458892.915 | 8.641 | 0.003 |
| 2458835.995 | 8.52 | 0.003 | 2458892.915 | 8.596 | 0.003 |
| 2458839.938 | 8.495 | 0.002 | 2458892.916 | 8.569 | 0.002 |
| 2458840.913 | 8.495 | 0.002 | 2458900.952 | 8.578 | 0.002 |
| 2458840.914 | 8.299 | 0.002 | 2458900.952 | 8.588 | 0.002 |
| 2458847.896 | 8.305 | 0.003 | 2458900.953 | 8.473 | 0.003 |
| 2458847.896 | 8.308 | 0.002 | 2458904.92 | 8.485 | 0.002 |
| 2458847.896 | 8.192 | 0.003 | 2458904.92 | 8.496 | 0.003 |
| 2458850.061 | 8.266 | 0.002 | 2458904.921 | 8.526 | 0.002 |
| 2458850.061 | 8.281 | 0.002 | 2458908.92 | 8.494 | 0.002 |
| 2458850.061 | 8.278 | 0.002 | 2458908.92 | 8.504 | 0.002 |
| 2458861.897 | 8.349 | 0.003 | 2458908.92 | 8.466 | 0.003 |
| 2458862.97 | 8.356 | 0.003 | 2458909.951 | 8.453 | 0.003 |
| 2458862.97 | 8.346 | 0.003 | 2458909.951 | 8.469 | 0.003 |
| 2458862.97 | 8.323 | 0.004 | 2458909.951 | 8.406 | 0.004 |
| 2458865.921 | 8.301 | 0.005 | 2458910.917 | 8.401 | 0.005 |
| 2458865.922 | 8.307 | 0.005 | 2458910.918 | 8.385 | 0.005 |
| 2458865.922 | 8.401 | 0.005 | 2458910.918 | 8.393 | 0.005 |
| 2458867.012 | 8.397 | 0.005 | 2458911.917 | 8.394 | 0.005 |
| 2458867.012 | 8.39 | 0.005 | 2458911.918 | 8.377 | 0.005 |
| 2458867.012 | 8.459 | 0.003 | 2458912.909 | 8.376 | 0.003 |
| 2458867.921 | 8.464 | 0.003 | 2458912.909 | 8.374 | 0.003 |
| 2458867.921 | 8.453 | 0.003 | 2458912.909 | 8.298 | 0.003 |
| 2458867.921 | 8.498 | 0.003 | 2458913.887 | 8.291 | 0.003 |
| 2458870.974 | 8.492 | 0.003 | 2458913.887 | 8.259 | 0.003 |
| 2458870.975 | 8.496 | 0.003 | 2458913.887 | 8.23 | 0.003 |
| 2458870.975 | 8.584 | 0.003 | 2458917.914 | 8.225 | 0.003 |
| 2458872.036 | 8.579 | 0.003 | 2458917.914 | 8.24 | 0.003 |
| 2458872.036 | 8.58 | 0.003 | 2458917.914 | 8.225 | 0.003 |
| 2458872.036 | 8.685 | 0.004 | 2458919.9 | 8.207 | 0.004 |
| 2458875.936 | 8.664 | 0.003 | 2458919.901 | 8.221 | 0.003 |
| 2458875.936 | 8.711 | 0.003 | 2458919.901 | 8.245 | 0.003 |
| 2458875.936 | 8.702 | 0.004 | 2458921.903 | 8.212 | 0.004 |
| 2458884.999 | 8.688 | 0.003 | 2458921.904 | 8.228 | 0.003 |
| 2458884.999 | 8.7 | 0.003 | 2458921.904 | 8.181 | 0.003 |
| 2458886.965 | 8.703 | 0.002 | 2458922.897 | 8.197 | 0.002 |
| 2458886.965 | 8.697 | 0.002 | 2458922.897 | 8.197 | 0.002 |
| 2458887.946 | 8.646 | 0.002 | 2458922.897 | 8.2 | 0.002 |
| 2458887.946 | 8.634 | 0.001 | 2458925.872 | 8.196 | 0.001 |
| 2458887.946 | 8.684 | 0.002 | 2458925.873 | 8.28 | 0.002 |
| 2458888.929 | 8.699 | 0.003 | 2458925.873 | 8.29 | 0.003 |
| 2458888.929 | 8.689 | 0.001 | 2458926.861 | 8.276 | 0.001 |
| 2458875.931 | 9.237 | 0.002 | 2458875.931 | 9.237 | 0.002 |
| 2458933.864 | 9.129 | 0.003 | 2458933.864 | 9.129 | 0.003 |

**Table A.9:** BSM photometric observations of IW Car in the $V$ filter.

| JD | V mag | V Err | JD | V mag | V Err |
|---|---|---|---|---|---|
| 2458735.386 | 8.166 | 0.001 | 2458856.348 | 7.89 | 0.002 |
| 2458735.391 | 8.171 | 0.003 | 2458858.188 | 7.921 | 0.003 |
| 2458748.384 | 8.31 | 0.003 | 2458858.191 | 7.868 | 0.004 |
| 2458748.387 | 8.3 | 0.002 | 2458858.193 | 7.896 | 0.002 |
| 2458748.39 | 8.316 | 0.003 | 2458859.152 | 7.896 | 0.003 |
| 2458755.378 | 8.213 | 0.003 | 2458859.155 | 7.874 | 0.003 |
| 2458755.381 | 8.244 | 0.002 | 2458859.158 | 7.902 | 0.002 |
| 2458755.384 | 8.252 | 0.002 | 2458860.145 | 7.893 | 0.002 |
| 2458775.348 | 7.931 | 0.002 | 2458860.151 | 7.913 | 0.002 |
| 2458775.35 | 7.943 | 0.003 | 2458861.177 | 7.933 | 0.003 |
| 2458775.353 | 7.946 | 0.002 | 2458861.18 | 7.947 | 0.002 |
| 2458778.348 | 7.926 | 0.003 | 2458861.182 | 7.926 | 0.003 |
| 2458778.35 | 7.914 | 0.002 | 2458864.302 | 8.026 | 0.002 |
| 2458778.353 | 7.951 | 0.002 | 2458864.305 | 7.992 | 0.002 |
| 2458782.335 | 7.898 | 0.002 | 2458864.307 | 7.985 | 0.002 |
| 2458782.337 | 7.938 | 0.003 | 2458867.203 | 8.025 | 0.003 |
| 2458782.34 | 7.938 | 0.003 | 2458867.206 | 8.037 | 0.003 |
| 2458826.333 | 8.29 | 0.003 | 2458867.208 | 8.04 | 0.003 |
| 2458826.336 | 8.291 | 0.004 | 2458868.125 | 8.067 | 0.004 |
| 2458826.338 | 8.329 | 0.005 | 2458868.128 | 8.094 | 0.005 |
| 2458827.312 | 8.326 | 0.005 | 2458868.131 | 8.075 | 0.005 |
| 2458827.315 | 8.305 | 0.005 | 2458870.332 | 8.18 | 0.005 |
| 2458856.342 | 7.902 | 0.005 | 2458870.334 | 8.206 | 0.005 |
| 2458856.345 | 7.903 | 0.005 | 2458870.337 | 8.179 | 0.005 |

**Table A.10:** UCMJO photometric observations of IW Car in the $B$ filter.

| JD | B mag | B Err | JD | B mag | B Err |
|---|---|---|---|---|---|
| 2458832.904 | 8.573 | 0.003 | 2458892.914 | 8.704 | 0.001 |
| 2458832.904 | 8.61 | 0.001 | 2458892.915 | 8.748 | 0.003 |
| 2458832.905 | 8.635 | 0.002 | 2458892.915 | 8.709 | 0.002 |
| 2458835.994 | 8.493 | 0.003 | 2458900.951 | 8.705 | 0.003 |
| 2458835.994 | 8.485 | 0.003 | 2458900.951 | 8.656 | 0.001 |
| 2458835.994 | 8.5 | 0.002 | 2458900.952 | 8.647 | 0.002 |
| 2458840.913 | 8.665 | 0.002 | 2458904.919 | 8.596 | 0.002 |
| 2458840.913 | 8.432 | 0.002 | 2458904.919 | 8.585 | 0.002 |
| 2458847.895 | 8.212 | 0.003 | 2458904.92 | 8.581 | 0.003 |
| 2458847.896 | 8.178 | 0.002 | 2458908.919 | 8.474 | 0.002 |
| 2458847.896 | 8.183 | 0.003 | 2458908.919 | 8.465 | 0.003 |
| 2458861.896 | 8.07 | 0.002 | 2458908.919 | 8.482 | 0.002 |
| 2458862.969 | 8.166 | 0.002 | 2458909.949 | 8.495 | 0.002 |
| 2458862.969 | 8.163 | 0.002 | 2458909.95 | 8.495 | 0.002 |
| 2458862.97 | 8.171 | 0.003 | 2458909.95 | 8.463 | 0.003 |
| 2458865.92 | 8.26 | 0.003 | 2458910.917 | 8.415 | 0.003 |
| 2458865.921 | 8.263 | 0.003 | 2458910.917 | 8.377 | 0.003 |
| 2458865.921 | 8.25 | 0.004 | 2458910.917 | 8.384 | 0.004 |
| 2458867.011 | 8.247 | 0.005 | 2458911.916 | 8.341 | 0.005 |
| 2458867.011 | 8.232 | 0.005 | 2458911.917 | 8.386 | 0.005 |
| 2458867.011 | 8.224 | 0.005 | 2458912.907 | 8.406 | 0.005 |
| 2458867.92 | 8.297 | 0.005 | 2458912.908 | 8.396 | 0.005 |
| 2458867.92 | 8.319 | 0.005 | 2458912.908 | 8.409 | 0.005 |
| 2458867.921 | 8.249 | 0.003 | 2458913.886 | 8.31 | 0.003 |
| 2458870.973 | 8.313 | 0.003 | 2458913.886 | 8.31 | 0.003 |
| 2458870.974 | 8.408 | 0.003 | 2458913.886 | 8.299 | 0.003 |
| 2458870.974 | 8.392 | 0.003 | 2458917.913 | 8.184 | 0.003 |
| 2458872.035 | 8.449 | 0.003 | 2458917.913 | 8.187 | 0.003 |
| 2458872.035 | 8.438 | 0.003 | 2458917.913 | 8.175 | 0.002 |
| 2458872.035 | 8.449 | 0.003 | 2458919.899 | 8.093 | 0.003 |
| 2458875.935 | 8.588 | 0.003 | 2458919.9 | 8.112 | 0.003 |
| 2458875.935 | 8.571 | 0.003 | 2458919.9 | 8.122 | 0.003 |
| 2458875.936 | 8.599 | 0.004 | 2458921.902 | 8.069 | 0.004 |
| 2458884.998 | 8.575 | 0.003 | 2458921.903 | 8.071 | 0.003 |
| 2458884.999 | 8.703 | 0.003 | 2458921.903 | 8.066 | 0.003 |
| 2458886.964 | 8.695 | 0.004 | 2458922.896 | 8.042 | 0.004 |
| 2458886.964 | 8.758 | 0.003 | 2458922.896 | 8.031 | 0.003 |
| 2458887.945 | 8.774 | 0.003 | 2458922.896 | 8.05 | 0.003 |
| 2458887.945 | 8.758 | 0.002 | 2458925.871 | 7.923 | 0.002 |
| 2458887.945 | 8.762 | 0.002 | 2458925.872 | 7.919 | 0.002 |
| 2458888.928 | 8.75 | 0.002 | 2458926.86 | 8.072 | 0.002 |
| 2458888.928 | 8.688 | 0.001 | 2458926.861 | 8.031 | 0.001 |
| 2458888.928 | 8.765 | 0.002 | 2458926.861 | 8.023 | 0.002 |
| 2458890.935 | 8.778 | 0.003 | 2458933.858 | 8.153 | 0.003 |
| 2458890.936 | 8.787 | 0.001 | 2458933.858 | 8.171 | 0.001 |
| 2458890.936 | 8.808 | 0.002 | 2458933.859 | 8.154 | 0.001 |

# Appendix B

# Spectroscopy Results

The radial velocities from the Fe I line at 6200.313 Å were measured by fitting Gaussian profiles to the line profile in each of the 92 spectra. The Gaussian fitting code outputted uncertainties in the fitted centroid position, width and depth. Fitted line positions with 95% confidence limit uncertainties were converted to velocity to give an upper limit uncertainty of $\pm 2\,\mathrm{km\,s^{-1}}$ in radial velocities. The uncertainty in cross-correlated radial velocities is $\pm 0.14\,\mathrm{km\,s^{-1}}$.

**Table B.1:** Radial velocities measured from 92 spectra of U Mon taken between 2019 November and 2020 March.

| JD | Phase ($\phi$) | Fe I 6200.313 Å ($\mathrm{km\,s^{-1}}$) | Cross-correlation ($\mathrm{km\,s^{-1}}$) |
|---|---|---|---|
| 2458790.056 | 0.0000 | 47.63 | 48.21 |
| 2458790.068 | 0.0001 | 47.59 | 48.47 |
| 2458791.113 | 0.0115 | 49.09 | 49.26 |
| 2458791.124 | 0.0116 | 49.18 | 49.52 |
| 2458826.099 | 0.3924 | 32.15 | 41.50 |
| 2458826.110 | 0.3925 | 32.11 | 41.65 |
| 2458827.020 | 0.4024 | 33.53 | 42.08 |
| 2458827.032 | 0.4025 | 33.53 | 42.09 |
| 2458827.110 | 0.4034 | 33.66 | 42.17 |
| 2458832.005 | 0.4567 | 41.5 | 44.92 |
| 2458832.016 | 0.4568 | 41.12 | 44.94 |
| 2458833.002 | 0.4675 | 42.93 | 45.99 |
| 2458833.014 | 0.4676 | 42.92 | 45.79 |
| 2458855.082 | 0.7079 | 20.23 | 43.93 |
| 2458855.094 | 0.7080 | 20.33 | 43.88 |
| 2458857.075 | 0.7296 | 18.03 | 39.61 |
| 2458857.087 | 0.7297 | 18.36 | 39.60 |
| 2458857.098 | 0.7299 | 18.08 | 39.77 |
| 2458858.076 | 0.7405 | 17.45 | 38.01 |
| 2458858.087 | 0.7406 | 17.57 | 38.03 |
| 2458858.099 | 0.7408 | 17.71 | 38.02 |
| 2458859.052 | 0.7511 | 17.4 | 36.95 |
| 2458859.109 | 0.7518 | 17.39 | 36.56 |
| 2458860.984 | 0.7722 | 18.42 | 35.40 |
| 2458861.091 | 0.7733 | 18.29 | 35.15 |

**Table B.2:** Radial velocities measured from 92 spectra of U Mon taken between 2019 November and 2020 March.

| JD | Phase ($\phi$) | Fe I 6200.313 Å ($\mathrm{km\,s^{-1}}$) | Cross-correlation ($\mathrm{km\,s^{-1}}$) | JD | Phase ($\phi$) | Fe I 6200.313 Å ($\mathrm{km\,s^{-1}}$) | Cross-correlation ($\mathrm{km\,s^{-1}}$) |
|---|---|---|---|---|---|---|---|
| 2458861.102 | 0.7735 | 18.48 | 35.04 | 2458892.922 | 1.1199 | 54.40 | 53.08 |
| 2458862.054 | 0.7838 | 19.06 | 35.02 | 2458892.932 | 1.1200 | 54.60 | 52.87 |
| 2458862.065 | 0.7839 | 18.98 | 34.99 | 2458894.905 | 1.1415 | 59.80 | 51.75 |
| 2458862.077 | 0.7841 | 18.97 | 35.00 | 2458894.919 | 1.1416 | 60.10 | 51.66 |
| 2458862.993 | 0.7942 | 19.72 | 34.81 | 2458895.989 | 1.1533 | 65.90 | 49.98 |
| 2458863.004 | 0.7942 | 19.63 | 34.79 | 2458896.006 | 1.1535 | 67.20 | 49.28 |
| 2458864.016 | 0.8052 | 20.60 | 34.84 | 2458913.916 | 1.3485 | 26.70 | 39.78 |
| 2458864.028 | 0.8053 | 20.48 | 34.82 | 2458913.928 | 1.3486 | 26.90 | 39.81 |
| 2458864.044 | 0.8055 | 20.57 | 34.87 | 2458914.915 | 1.3593 | 28.10 | 40.35 |
| 2458864.056 | 0.8056 | 20.50 | 34.82 | 2458914.926 | 1.3595 | 28.10 | 39.95 |
| 2458865.032 | 0.8162 | 21.41 | 34.99 | 2458916.866 | 1.3806 | 30.90 | 42.02 |
| 2458865.044 | 0.8164 | 21.46 | 35.01 | 2458916.878 | 1.3807 | 31.21 | 41.76 |
| 2458885.865 | 1.0431 | 52.72 | 49.24 | 2458916.891 | 1.3808 | 31.10 | 42.09 |
| 2458886.982 | 1.0552 | 53.50 | 50.96 | 2458916.903 | 1.3810 | 31.20 | 42.11 |
| 2458886.998 | 1.0554 | 53.60 | 50.82 | 2458919.825 | 1.4128 | 36.90 | 43.59 |
| 2458887.039 | 1.0558 | 53.50 | 50.82 | 2458919.837 | 1.4129 | 36.91 | 44.57 |
| 2458887.858 | 1.0648 | 54.40 | 45.69 | 2458919.850 | 1.4131 | 36.92 | 44.65 |
| 2458887.868 | 1.0649 | 54.50 | 50.51 | 2458919.861 | 1.4132 | 37.10 | 44.47 |
| 2458888.043 | 1.0668 | 54.60 | 51.30 | 2458920.827 | 1.4237 | 39.10 | 45.19 |
| 2458888.054 | 1.0669 | 54.60 | 51.16 | 2458920.838 | 1.4238 | 39.10 | 45.33 |
| 2458888.856 | 1.0756 | 55.08 | 48.62 | 2458920.851 | 1.4240 | 39.20 | 45.39 |
| 2458888.865 | 1.0757 | 55.00 | 51.38 | 2458920.863 | 1.4241 | 39.30 | 45.38 |
| 2458888.875 | 1.0758 | 54.97 | 51.57 | 2458921.825 | 1.4346 | 41.30 | 46.07 |
| 2458889.040 | 1.0776 | 55.10 | 51.63 | 2458921.837 | 1.4347 | 41.30 | 46.22 |
| 2458889.855 | 1.0865 | 55.40 | 48.47 | 2458921.853 | 1.4349 | 41.35 | 46.22 |
| 2458889.864 | 1.0866 | 55.10 | 51.88 | 2458921.865 | 1.4350 | 41.37 | 46.22 |
| 2458889.876 | 1.0867 | 55.40 | 52.15 | 2458922.823 | 1.4454 | 43.30 | 46.71 |
| 2458889.893 | 1.0869 | 55.30 | 52.20 | 2458922.834 | 1.4455 | 43.50 | 46.97 |
| 2458890.853 | 1.0974 | 54.80 | 47.55 | 2458922.848 | 1.4457 | 43.45 | 46.94 |
| 2458890.864 | 1.0975 | 55.00 | 52.49 | 2458922.859 | 1.4458 | 43.41 | 46.96 |
| 2458890.877 | 1.0976 | 54.30 | 52.60 | 2458923.853 | 1.4566 | 45.80 | 47.52 |
| 2458890.918 | 1.0981 | 54.50 | 52.73 | 2458923.895 | 1.4571 | 45.50 | 47.63 |
| 2458890.928 | 1.0982 | 54.60 | 52.57 | 2458923.907 | 1.4572 | 45.90 | 46.96 |

# Bibliography


Aerts C., Christensen-Dalsgaard J., Kurtz D. W., 2010, *Asteroseismology*

Aikawa, T. 2010, *The instability strip and pulsation features of post-AGB star models*, A&A, 514, A45

Anderson R. I., 2020, *Cepheids under the magnifying glass – not so simple, after all!*, arXiv e-prints, p. arXiv:2001.03028

Baird S. R., 1984, *Causes of anomalous line-splitting in RV Tauri stars.*, , 96, 72

Benn D., 2012, *Algorithms + Observations = VStar*, Journal of the American Association of Variable Star Observers (JAAVSO), 40, 852

Bevington P. R., 1969, *Data reduction and error analysis for the physical sciences*

Breger M., et al., 1993, *Nonradial pulsation of the delta Scuti star BU CANCRI in the Praesepe cluster.*, , 271, 482

Brown T. M., Gilliland R. L., 1994, *Asteroseismology*, , 32, 37

Brunsden E., 2013, PhD thesis, University of Canterbury, doi:10.5281/zenodo.50874, `https://doi.org/10.5281/zenodo.50874`

Buchlar J. R., Goupil M.-J., Kovács G., 1987, *Tangent bifurcations to Chaos in stellar pulsations*, Physics Letters A, 126, 177

Bujarrabal V., Castro-Carrizo A., Alcolea J., Van Winckel H., Sánchez Contreras C., Santand er-García M., 2017, *A second post-AGB nebula that contains gas in rotation and in expansion: ALMA maps of IW Carinae*, , 597, L5

Bódi A., Kiss L. L., 2019, *Physical Properties of Galactic RV Tauri Stars from Gaia DR2 Data*, The Astrophysical Journal, 872, 60

Carroll B. W., Ostlie D. A., 2006, *An introduction to modern astrophysics and cosmology*

Carroll B. W., Ostlie D. A., 2017, *Stellar Pulsation*, 2 edn. Cambridge University Press, p. 483–517, doi:10.1017/9781108380980.015

Catelan M., Smith H. A., 2015, *Pulsating Stars*

Ceraski W., 1905, *Trois nouvelles variables*, Astronomische Nachrichten, 168, 29

Collins K., Kielkopf J., 2013, *AstroImageJ: ImageJ for Astronomy* (ascl:1309.001)

De Ruyter S., Van Winckel H., Dominik C., Waters L. B. F. M., Dejonghe H., 2005, *Strong dust processing in circumstellar discs around 6 RVTauri stars*, Astronomy & Astrophysics, 435, 161–166

Deb S., Tiwari S. K., Singh H. P., Seshadri T. R., Chaubey U. S., 2009, *Photometry of the delta Scuti star HD 40372*, Bulletin of the Astronomical Society of India, 37, 109

Dvorak S., 2008, *Frequency Analysis of Long-term AAVSO Visual Observations of TU Cas*, Journal of the American Association of Variable Star Observers (JAAVSO)

Eid M. F. E., 2016, *Introduction to Asymptotic Giant Branch Stars*, Journal of Physics: Conference Series, 703, 012005

Ertel S., et al., 2019, *Resolved Imaging of the AR Puppis Circumbinary Disk*, , 157, 110

Fadeyev Y. A., Gillet D., 2004, *The structure of radiative shock waves. V. Hydrogen emission lines*, , 420, 423

Fokin A. B., 1994, *Nonlinear pulsations of the RV Tauri stars.*, , 292, 133

Foster G., 1996, *Wavelets for period analysis of unevenly sampled time series*, , 112, 1709

Freytag B., Liljegren S., Höfner S., 2017, *Global 3D radiation-hydrodynamics models of AGB stars. Effects of convection and radial pulsations on atmospheric structures*, , 600, A137

Gaige Y., 1993, *Stellar rotational velocities from the V sin i observations : inversion procedures and applications to open clusters.*, , 269, 267

Gary D. E., 2001, *PHYS 321, Astronomy and Astrophysics*

Gautschy A., Saio H., 1995, *Stellar Pulsations Across The HR Diagram: Part 1*, , 33, 75

Gavin H. P., 2013.

Gezer I., Van Winckel H., Bozkurt Z., De Smedt K., Kamath D., Hillen M., Manick R., 2015, *The WISE view of RV Tauri stars*, , 453, 133

Gielen C., van Winckel H., Waters L. B. F. M., Min M., Dominik C., 2007, *Dust-grain processing in circumbinary discs around evolved binaries. The RV Tauri spectral twins RU Centauri and AC Herculis*, , 475, 629

Gillet D., Burki G., Duquennoy A., 1990, *The pulsation of the photosphere of the RV Tauri stars : AC Herculis and R Scuti.*, , 237, 159

Giridhar S., Rao N. K., Lambert D. L., 1994, *The Chemical Composition of the RV Tauri Variable IW Carinae*, , 437, 476

Giridhar S., Lambert D. L., Gonzalez G., 2000, *Abundance Analyses of Field RV Tauri Stars. V. DS Aquarii, UY Arae, TW Camelopardalis, BT Librae, U Monocerotis, TT Ophiuchi, R Scuti, and RV Tauri*, The Astrophysical Journal, 531, 521

Gray D. F., 2005, *The Observation and Analysis of Stellar Photospheres*

Gray R. O., Corbally Christopher J., 2009, *Stellar Spectral Classification*

Greenwood A., 2014, Master's thesis, University of Canterbury

Hearnshaw J. B., Barnes S. I., Kershaw G. M., Frost N., Graham G., Ritchie R., Nankivell G. R., 2002, *The Hercules Échelle Spectrograph at Mt. John*, Experimental Astronomy, 13, 59

Hearnshaw J. B., Barnes S. I., Frost N., Kershaw G. M., Graham G., Nankivell G. R., 2003, *HERCULES: A High-resolution Spectrograph for Small to Medium-sized Telescopes*. pp 11–16

Herwig F., 2005, *Evolution of Asymptotic Giant Branch Stars*, , 43, 435

Höfner S., Olofsson H., 2018, *Mass loss of stars on the asymptotic giant branch. Mechanisms, models and measurements*, , 26, 1

Jeffery C. S., Saio H., 2016, *Radial pulsation as a function of hydrogen abundance*, , 458, 1352

Jura M., 1986, *RV Tauri Stars as Post–Asymptotic Giant Granch Objects*, , 309, 732

Kafka S., Templeton M., 2015, in IAU General Assembly. p. 2255477

Kallinger, T. et al., 2014, *The connection between stellar granulation and oscillation as seen by the Kepler mission*, A&A, 570, A41

Keenan P. C., McNeil R. C., 1989, *The Perkins Catalog of Revised MK Types for the Cooler Stars*, , 71, 245

Kippenhahn R., Weigert A., Weiss A., 2012, *Stellar Structure and Evolution*, doi:10.1007/978-3-642-30304-3.

Kiss L. L., Bódi A., 2017, *Amplitude variations of modulated RV Tauri stars support the dust obscuration model of the RVb phenomenon*, , 608, A99

Kiss L. L., Szabó G. M., Bedding T. R., 2006, *Variability in red supergiant stars: pulsations, long secondary periods and convection noise*, , 372, 1721

Kiss L. L., Derekas A., Szabó G. M., Bedding T. R., Szabados L., 2007, *Defining the instability strip of pulsating post-AGB binary stars from ASAS and NSVS photometry*, , 375, 1338

Koen C., 2020, *Significance levels of common frequencies extracted from multiple data sets*, , 493, 48

Kupka F., Piskunov N., Ryabchikova T. A., Stempels H. C., Weiss W. W., 1999, *VALD-2: Progress of the Vienna Atomic Line Data Base*, , 138, 119

Kurtz D. W., 2006, *Stellar pulsation: an overview*, Communications in Asteroseismology, 147, 6

Kuschnig R., Weiss W. W., Zwintz K., 1997, in Casertano S., Jedrzejewski R., Keyes T., Stevens M., eds, The 1997 HST Calibration Workshop with a New Generation of Instruments. p. 481

Lagadec E., 2017, in Liu X., Stanghellini L., Karakas A., eds, IAU Symposium Vol. 323, Planetary Nebulae: Multi-Wavelength Probes of Stellar and Galactic Evolution. pp 20–27 (arXiv:1701.04324), doi:10.1017/S1743921317000928

Leavitt H. S., Pickering E. C., 1912, *Periods of 25 Variable Stars in the Small Magellanic Cloud.*, Harvard College Observatory Circular, 173, 1

Lenz P., 2005, *Period04 User Guide*, 146, 53

Lenz P., Breger M., 2004, in Zverko J., Ziznovsky J., Adelman S. J., Weiss W. W., eds, IAU Symposium Vol. 224, The A-Star Puzzle. pp 786–790, doi:10.1017/S1743921305009750

Lenz P., Breger M., 2014, *Period04: Statistical analysis of large astronomical time series* (ascl:1407.009)

Lloyd Evans T., 1985, *Circumstellar material and the light variations of RV Tauri stars.*, , 217, 493

Lobel A., 2006, in IAU Joint Discussion. p. 22

Lobel A., 2008, in Journal of Physics Conference Series. p. 012015 (arXiv:0712.1185), doi:10.1088/1742-6596/130/1/012015

Maas T., Van Winckel H., Waelkens C., 2002, *RU Cen and SX Cen: Two strongly depleted RV Tauri stars in binary systems. The RV Tauri photometric b phenomenon and binarity*, , 386, 504

Maas T., Van Winckel H., Lloyd Evans T., 2005, *Depletion in post-AGB stars with a dusty disc. II.*, , 429, 297

Manick R., 2018, PhD thesis, Arenberg Doctoral School, KU Leuven, https://fys.kuleuven.be/ster/pub/phd-rajeev-manick/thesis_RM_final.pdf

Manick R., Van Winckel H., Kamath D., Hillen M., Escorza A., 2017, *Establishing binarity amongst Galactic RV Tauri stars with a disc⋆*, , 597, A129

Manick R., Van Winckel H., Kamath D., Sekaran S., Kolenberg K., 2018, *The evolutionary nature of RV Tauri stars in the SMC and LMC*, , 618, A21

Matsuura M., et al., 2014, *Spitzer Space Telescope spectra of post-AGB stars in the Large Magellanic Cloud - polycyclic aromatic hydrocarbons at low metallicities*, , 439, 1472

McSaveney J., 2003, PhD thesis, University of Canterbury

McSaveney J., Cottrell P., Pollard K., Mattei J., 2002, *Wavelet Analysis of the RV Tauri Star U Mon*, International Astronomical Union Colloquium, 185, 576–577

Montgomery M. H., Odonoghue D., 1999, *A derivation of the errors for least squares fitting to time series data*, Delta Scuti Star Newsletter, 13, 28

Nave G., Johansson S., Learner R. C. M., Thorne A. P., Brault J. W., 1994, *A New Multiplet Table for Fe i*, , 94, 221

Percy J. R., 1993, *Longterm Changes in Rv-Tauri Stars*. p. 295

Percy J. R., 2007, *Understanding Variable Stars*

Percy J. R., 2015, *Studies of RV Tauri and SRD Variables*, Journal of the American Association of Variable Star Observers (JAAVSO), 43, 176

Percy J. R., Abachi R., 2013, *Amplitude Variations in Pulsating Red Giants*, Journal of the American Association of Variable Star Observers (JAAVSO), 41, 193

Percy J. R., Khatu V. C., 2013, *Amplitude Variations in Pulsating Red Supergiants* (arXiv:1310.6306)

Percy J. R., Kim R. Y. H., 2014, *Amplitude Variations in Pulsating Yellow Supergiants*, Journal of the American Association of Variable Star Observers (JAAVSO), 42, 267

Percy J. R., Sasselov D. D., Alfred A., Scott G., 1991, *Period Changes and Evolution in RV Tauri Stars*, , 375, 691

Percy J. R., Bezuhly M., Milanowski M., Zsoldos E., 1997, *The Nature of the Period Changes in RV Tauri Stars*, , 109, 264

Plachy E., Molnár L., Kolláth Z., Benkő J. M., Kolenberg K., 2013, *On the interchange of alternating-amplitude pulsation cycles*, Proceedings of the International Astronomical Union, 9, 473–474

Plachy E., Bódi A., Kolláth Z., 2018, *Chaotic dynamics in the pulsation of DF Cygni, as observed by Kepler*, , 481, 2986

Pojmanski G., Pilecki B., Szczygiel D., 2005, *The All Sky Automated Survey. Catalog of Variable Stars. V. Declinations 0 arcd - +28 arcd of the Northern Hemisphere*, , 55, 275

Pollard K. H., Cottrell P. L., 1995, in Stobie R. S., Whitelock P. A., eds, Astronomical Society of the Pacific Conference Series Vol. 83, IAU Colloq. 155: Astrophysical Applications of Stellar Pulsation. p. 409

Pollard K. R., Lloyd Evans T., 1999, in Le Bertre T., Lebre A., Waelkens C., eds, IAU Symposium Vol. 191, Asymptotic Giant Branch Stars. p. 459

Pollard K. R., Cottrell P. L., Kilmartin P. M., Gilmore A. C., 1996, *RV Tauri stars. I. A long-term photometric survey.*, , 279, 949

Pollard K. R., Cottrell P. L., Lawson W. A., Albrow M. D., Tobin W., 1997, *RV Tauri stars - II. A spectroscopic study*, , 286, 1

Pollard K. R., et al., 2000, *RV Tauri Stars and Type II Cepheids in the Magellanic Clouds – Results from the MACHO Database*. pp 89–95

Pollard K. R., McSaveney J. A., Cottrelll P. L., 2006, *The long-term phenomenon in U Mon.*, , 77, 527

Preston G. W., Krzeminski W., Smak J., Williams J. A., 1963, *A Spectroscopic and Photoelectric Survey of the RV Tauri Stars.*, , 137, 401

Scargle J. D., 1982, *Studies in astronomical time series analysis. II. Statistical aspects of spectral analysis of unevenly spaced data.*, , 263, 835

Shenton M., et al., 1992, *Multiwavelength observations of RV Tauri stars. I. AC Herculis.*, , 262, 138

Shenton M., Evans A., Cardelli J. A., Marang F., van Wyk F., Weight A., 1994, *Multiwavelength observations of RV Tauri stars II. U Monocerotis*, , 287, 852

Skuljan J., 2004, in Kurtz D. W., Pollard K. R., eds, Astronomical Society of the Pacific Conference Series Vol. 310, IAU Colloq. 193: Variable Stars in the Local Group. p. 575

Sloan G. C., et al., 2014, *Carbon-rich Dust Past the Asymptotic Giant Branch: Aliphatics, Aromatics, and Fullerenes in the Magellanic Clouds*, , 791, 28

Soszynski I., et al., 2008a, *The Optical Gravitational Lensing Experiment. The OGLE-III Catalog of Variable Stars. I. Classical Cepheids in the Large Magellanic Cloud*, , 58, 163

Soszyński I., et al., 2008b, *The Optical Gravitational Lensing Experiment. The OGLE-III Catalog of Variable Stars. II. Type II Cepheids and Anomalous Cepheids in the Large Magellanic Cloud*, , 58, 293

Stanton R. H., 1999, *Visual Magnitudes and the "Average Observer": The SS Cygni Field Experiment*, Journal of the American Association of Variable Star Observers (JAAVSO), 27, 97

Sterken C., 2005, *The O-C Diagram: Basic Procedures*. p. 3

Takeuti M., Petersen J. O., 1983, *The resonance hypothesis applied to RV Tauri stars*, , 117, 352

Templeton M., 2004, *Time-Series Analysis of Variable Star Data*, Journal of the American Association of Variable Star Observers (JAAVSO), 32, 41

Tuchman Y., Lebre A., Mennessier M. O., Yarri A., 1993, *Linear analysis of RV Tauri stars : the resonance hypothesis.*, , 271, 501

Valenti J. A., Piskunov N., Johns-Krull C. M., 1998, *Spectral Synthesis of TiO Lines*, , 498, 851

Vega L. D., Montez R. J., Stassun K. G., Kaminski T., Sabin L., Principe D., Boyd P. T., Schlegel E. M., 2020, in American Astronomical Society Meeting Abstracts. American Astronomical Society Meeting Abstracts. p. 106.07

Waelkens C., Waters L. B. F. M., 1993, *Binarity of High-Latitude Supergiants - Observational Evidence*. p. 219

Wallerstein G., 2002, *The Cepheids of Population II and Related Stars*, , 114, 689

Willson L. A., Templeton M., 2009, in Guzik J. A., Bradley P. A., eds, American Institute of Physics Conference Series Vol. 1170, American Institute of Physics Conference Series. pp 113–121, doi:10.1063/1.3246421

Wilson R. E., 1953, *General catalogue of stellar radial velocities.*, Carnegie Institute Washington D.C. Publication, p. 0

Wright D. J., Pollard K. R., Cottrell P. L., 2007, *Analysis tools for non-radially pulsating objects*, Communications in Asteroseismology, 150, 135

Zissell R., 2002, *Transformation of AAVSO Archive Visual Data to the Johnson V System*, Journal of the American Association of Variable Star Observers (JAAVSO)

Zsoldos E., 1996, *RV Tauri and the RVB phenomenon. I. Photometry of RV Tauri.*, , 119, 431

Zsoldos E., 1998, *No RV Tauri Stars in Globular Clusters?*, , 48, 775

de Boer K., Seggewiss W., 2008, *Stars and Stellar Evolution*

de Ruyter S., van Winckel H., Dominik C., Waters L. B. F. M., Dejonghe H., 2005, *Strong dust processing in circumstellar discs around 6 RV Tauri stars. Are dusty RV Tauri stars all binaries?*, , 435, 161